



## Durham E-Theses

---

### *Nano-scale structure of polymers and small molecules in organic electronic applications*

ALANAZI, FAISAL

#### How to cite:

---

ALANAZI, FAISAL (2023) *Nano-scale structure of polymers and small molecules in organic electronic applications*, Durham theses, Durham University. Available at Durham E-Theses Online:  
<http://etheses.dur.ac.uk/14921/>

#### Use policy

---

The full-text may be used and/or reproduced, and given to third parties in any format or medium, without prior permission or charge, for personal research or study, educational, or not-for-profit purposes provided that:

- a full bibliographic reference is made to the original source
- a [link](#) is made to the metadata record in Durham E-Theses
- the full-text is not changed in any way

The full-text must not be sold in any format or medium without the formal permission of the copyright holders.

Please consult the [full Durham E-Theses policy](#) for further details.

**Nano-scale structure of  
polymers and small molecules  
in organic electronic  
applications**

**Faisal Alanazi**

A thesis presented for the degree of  
Doctor of Philosophy



Centre for Materials Physics

The University of Durham

United Kingdom

January 2023

# Nano-scale structure of polymers and small molecules in organic electronic applications

Faisal K Alanazi

## Abstract

The thesis explores novel electron microscopy techniques for probing the molecular ordering in organic thin-films at high spatial resolution. The research is relevant to the wider field of optoelectronics as organic electronic devices, such as organic photovoltaics (OPV) and organic light emitting diodes (OLED), have become desirable as a potentially low-cost, flexible, and lightweight alternative to conventional inorganic technologies. The crystallinity in organic materials determines important properties, such as charge carrier mobility, but is extremely complex and difficult to characterise. Unlike standard inorganic crystals that have long-range order (LRO), organic materials tend to be disordered, with some regions of the material amorphous, and other regions semi-crystalline or crystalline. The study uses several electron microscopy methods to examine the nanoscale ordering in organic thin-films, including a variation of the fluctuation electron microscopy (FEM) technique performed in a scanning transmission electron microscope (STEM) to probe the medium-range order (MRO), as well as electron energy loss spectroscopy (EELS) to determine the orientation of  $\pi$ -stacking from the carbon K-edge fine structure. Multislice simulation (Chapter 3) is also used to examine the role of a range of parameters such as particle crystalline size, depth in the sample, atomic number, and para-crystallinity on the expected contrast in dark-field STEM imaging. The effect of these parameters is difficult to isolate by experiment, and therefore simulations are required to make estimates. The sensitivity to parameters such as the particle size was found to be similar to that estimated from experiment.

Chapter 4 presents the FEM results. STEM annular dark field (DF) imaging is used to measure the diffracted intensity of crystalline domains. By varying the

inner angle of the annular detector used for DF imaging, it is possible to control the ‘coherence volume’, i.e. the volume over which diffraction takes place. This provides information on the degree of crystallinity as well as domain size. The measurements were first performed on a polycrystalline NiO thin-film test sample. It was found that the STEM technique overall showed the expected behaviour for NiO. After testing NiO, we examined samples of drop cast and spin coated TIPS pentacene by a conventional TEM at 200 kV, and found limitations in the information that could be extracted due to specimen damage under the electron beam. However, we found that useful information could be obtained on a 200 kV Talos TEM with direct electron detector and 4D STEM measurements. The drop cast TIPS pentacene diffraction pattern resembles previous reports in the literature. In particular, diffuse streaking due to pentacene molecular movement is seen. The molecular disorder was not uniformly distributed across the sample, as seen by virtual dark-field images taken from several points along the streak. A virtual dark-field image of the spin coated TIPS pentacene sample showed grains with an average size of 58.7 nm, and the diffraction pattern also showed Bragg reflections. The spin coated sample appears to have more paracrystallinity inside the grains than the drop cast sample, according to variance plots obtained from the same 4D STEM datasets.

EELS spectroscopy (Chapter 5) of the carbon K-edge fine structure is used to map the local orientation of organic thin-films like TIPS pentacene. A natural graphite sample was used to calibrate the  $\pi^*/\sigma^*$  ratio as a function of specimen orientation for both TEM and STEM modes. Application of EELS spectrum imaging to a TIPS pentacene thin-film however showed that the minimum dose required for an accurate  $\pi^*/\sigma^*$  ratio was several orders of magnitude above the critical electron beam dose for damage under the electron beam. Therefore, successful application of EELS to study molecular disorder requires strategies to overcome the beam damage in organic thin-films. These include increasing the energy of the incident electron beam (higher kV), using a cryo-microscope to cool the specimen, and direct electron detectors with higher detector quantum efficiency, as well as dose fractionation.

Department of Physics

Reviewers: Prof Andy Brown and Prof Elizabeth Bromley

Supervisors: Dr. Mendis Buddhika and Dr. Fernando Dias

**Durham University**

Centre for Materials Physics

Department of Physics

31 Ayden Grove, Newton Hall

Durham

DH1 5FS

---

# Acknowledgements

I would like to acknowledge the support of my supervisors Dr. Budhika Mendis and Dr. Fernando Dias for their continued guidance and enthusiasm. I also give thanks to Dr. Kleitos Stavrou and Dr. Andrew Danos from Physics Department for preparing organic thin film samples, such as TIPS pentacene.

---

# Contents

<b>Declaration</b>	<b>viii</b>
<b>List of Figures</b>	<b>ix</b>
<b>List of Tables</b>	<b>xxi</b>
<b>1 Organic thin films</b>	<b>1</b>
1.1 Introduction to organic materials . . . . .	1
1.2 Conjugated polymers and small molecules . . . . .	3
1.2.1 Band structure in organic materials . . . . .	3
1.2.2 Examples of conjugated polymers . . . . .	5
1.2.3 Examples of small molecules . . . . .	6
1.2.4 Optical excitation in conjugated systems . . . . .	7
1.3 Microstructure of organic materials . . . . .	9
1.3.1 Semi-crystalline . . . . .	9
1.3.2 Poly-crystalline . . . . .	10
1.3.3 Polymer fullerene blends . . . . .	12
1.3.4 Charge transport and Mobility . . . . .	14
1.4 Pair Correlation Functions . . . . .	16
1.5 Motivation of project . . . . .	18

<b>2</b>	<b>Electron Microscope</b>	<b>20</b>
2.1	Introduction . . . . .	20
2.1.1	Transmission Electron Microscopy (TEM) . . . . .	22
2.1.2	Scanning Transmission Electron Microscopy (STEM) . . . . .	24
2.2	Bright and Dark field imaging . . . . .	28
2.3	Phase contrast and high resolution electron microscopy (HREM) . . . . .	31
2.4	Electron diffraction and pair correlation function . . . . .	33
2.5	Electron microscopy techniques for probing order . . . . .	36
2.5.1	Fluctuation Electron Microscopy in the TEM . . . . .	36
2.5.2	Fluctuation Electron Microscopy in the STEM . . . . .	41
2.5.3	Energy electron loss spectroscopy (EELS) analysis . . . . .	44
2.6	Multislice Simulation . . . . .	51
<b>3</b>	<b>Multislice Simulations</b>	<b>54</b>
3.1	Motivation for simulations . . . . .	54
3.1.1	Simulation procedure . . . . .	55
3.2	Results and discussion . . . . .	63
3.2.1	Radius and atomic number . . . . .	63
3.2.2	Particle depth in the specimen. . . . .	68
3.2.3	Para-crystallinity in the specimen. . . . .	71
3.3	Summary and conclusions . . . . .	73
<b>4</b>	<b>STEM and 4D STEM</b>	<b>75</b>
4.1	Motivation . . . . .	75
4.2	Experimental Method . . . . .	77
4.2.1	Sample preparation . . . . .	77
4.2.2	Electron Microscopy . . . . .	78
4.3	NiO experimental results . . . . .	81
4.3.1	NiO thin-film characterisation . . . . .	81
4.3.2	Grain Size Analysis . . . . .	82

4.3.3	STEM Fluctuation Electron Microscopy . . . . .	84
4.3.4	4D STEM . . . . .	86
4.4	TIPS pentacene experimental results . . . . .	90
4.4.1	TIPS pentacene characterisation . . . . .	90
4.4.2	4D STEM . . . . .	92
4.4.3	Variance plots . . . . .	96
4.5	Conclusions . . . . .	98
<b>5</b>	<b>EELS spectroscopy</b>	<b>100</b>
5.1	Motivation . . . . .	100
5.2	Anisotropy in carbon K-edge . . . . .	102
5.3	Beam Damage . . . . .	109
5.4	STEM EELS Mapping . . . . .	111
5.5	Conclusions . . . . .	116
<b>6</b>	<b>Future work</b>	<b>117</b>
	<b>Bibliography</b>	<b>121</b>

---

# Declaration

The work in this thesis is based on research carried out at the Centre for Advanced Instrumentation, Department of Physics, University of Durham, England. No part of this thesis has been submitted elsewhere for any other degree or qualification, and it is the sole work of the author unless referenced to the contrary in the text.

Some of the work presented in this thesis has been published in journals and conference proceedings - the relevant publications are listed below.

## Publications

Palacios-Gómez, D. A., Huerta Flores, A. M., MacKenzie, R. C. I., Pearson, C., Alanazi, F., Mendis, B. G., Groves, C. (2021). Differing Impacts of Blended Fullerene Acceptors on the Performance of Ternary Organic Solar Cells. *ACS Applied Energy Materials*, 4(10), 10867-10876.

**Copyright © 2023 by Faisal Alanazi.**

*“The copyright of this thesis rests with the author. No quotation from it should be published without the author’s prior written consent and information derived from it should be acknowledged”.*

---

## List of Figures

1.1	Some examples of conductive polymers. The square bracket indicates the monomer and the subscript 'n' refers to the number of repeating units (Rasmussen, 2014). . . . .	2
1.2	Two alternative structures of benzene with single and double covalent bonds are shown in a) and b). c) Shows the equivalent structure with the delocalised electrons moving around the molecule with no impediment (Geoghegan and Hadziioannou, 2013). . . . .	3
1.3	The structure of polyacetylene, containing alternating single and double bonds (Le et al., 2017) . . . . .	4
1.4	Ethane molecule consisting of six hydrogen atoms and two $sp^3$ hybridised carbon atoms and ethene consisting of four hydrogen atoms and two $sp^2$ hybridised carbon atoms (Koehler and Baessler, 2015). . . . .	5
1.5	Energy level diagram illustrating the formation of $\sigma$ and $\pi$ -bonds from atomic orbitals for ethene. . . . .	6
1.6	Chemical structures of some undoped conjugated polymers (Krieger, 1999). . . . .	6
1.7	Chemical structure of PCBM (Huang et al., 2015). . . . .	7
1.8	Chemical structures of some common planar organic molecules. . . . .	8
1.9	Schematic showing exciton formation and dissociation in OPV donor-acceptor blend (Haruk and Mativetsky, 2015). . . . .	9

1.10	Schematic of the microstructure of a semi-crystalline polymer film, where the lamellae ordered areas are crystalline regions and the area surrounding it is amorphous (Callister et al., 2007).	10
1.11	a) Monomers of P3HT and b) lamellar structure of co-facially stacked conjugated sheets, with $\pi$ -stacking direction indicated (Chowdhury et al., 2017)	10
1.12	Grain boundaries in a polycrystalline material, a) macroscopic and b) atomic scale (Nagra, 2019).	11
1.13	a) Atomic force microscopy (AFM) image of thermally evaporated pentacene films (Stadlober et al., 2003). The pentacene has a dendritic structure and preferential orientation. The grain boundaries are the regions between the pentacene crystals. b) Pentacene and its crystal packing showing predominant edge-to-face interactions (Anthony, 2006).	12
1.14	Schematic morphology of P3HT:PCBM films post-treated with different solvent vapors, a) chlorobenzene, b) toluene, c) xylene and d) dichlorobenzene. The grey spheres indicate PCBM, red tangled lines represent amorphous P3HT and red parallel lines are P3HT crystallites (Wang et al., 2016).	13
1.15	Charge transport via hopping to localised trap states within the forbidden gap (Oelerich et al., 2014).	14
1.16	The radial distribution function $g_2(r)$ for a disordered solid. The peaks and troughs represent atom correlations that deviate from an ideal gas, which has a constant $g_2(r)$ value of unity	16
1.17	Two concentric spherical shells where the grey colour indicates the effective search volume for the correlation function. (a) $g_2(r)$ searches the volume between $r$ and $r + dr$ within the shell. (b) $g_3(r_1, r, \theta)$ searches a small portion of volume that is between $r$ and $r + dr$ about $\theta$ and $\theta + d\theta$ where $\theta$ is measured with respect to $r_1$ that is between to atoms (Voyles and Abelson, 2003).	17

1.18	The dihedral angle is defined as the angle between two planes, each containing at least three atoms with two atoms in common. In the above figure $\theta$ is the bond angle and $\phi$ is the dihedral angle (Abdullah et al., 2015). . . . .	18
2.1	(a) Intensity profile of the Airy pattern. (b) Intensity plot along the radial direction, showing the Airy Disk radius (Graney, 2009). . . . .	21
2.2	(a) Schematic of a field-emission source formed by two anodes and (b) the energy level diagram showing the process of field emission through tunneling ( $E_{vac}$ is the vacuum energy level, while $E_F$ and $\phi$ are the Fermi level and work function for the tungsten tip). The gradient of $E_{vac}$ is proportional to the electric field at the tip (Williams and Carter, 2009). . . . .	22
2.3	Parallel-beam operation in the TEM. . . . .	23
2.4	Ray diagram for a finite object as imaged by an objective lens. It shows the formation of a diffraction pattern in the back focal plane and real space image of the sample in the image plane (Williams and Carter, 2009). . . . .	24
2.5	Convergent beam STEM mode operation in a TEM/STEM microscope (Williams and Carter, 2009). . . . .	25
2.6	Ray diagrams show the reciprocity between a) TEM and b) STEM (Zhou and Wang, 2007). . . . .	26
2.7	Ray diagram showing the effects of spherical aberration. Higher angle rays are focussed more strongly by the lens causing blurring of a point object 'P'. . . . .	26
2.8	Schematic of a diffraction aberrated probe. . . . .	27
2.9	Curve of the diffraction and spherical aberration limited probe sizes . . . . .	28

2.10	Ray diagrams showing how an objective aperture is used to produce (a) a bright field (BF) image formed from the on-axis, transmitted electron beam, (b) a dark field (DF) image formed with a specific off-axis scattered beam, and (c) a centered dark field (CDF) image where the incident beam is tilted to let the scattered beam pass along the optic axis(Williams and Carter, 1978). . . . .	29
2.11	Schematic of image formation in a STEM, showing the on-axis small bright-field detector and an annular dark-field detector (pink) (MacArthur, 2016). . . . .	30
2.12	Electron wave profile a) within an atom and b) in vacuum. The vertical dashed lines represents the phase shift between the two electron wavefronts. . . . .	31
2.13	HREM image of a pentacene nanocrystal showing bright and dark fringes of a crystal surrounded by amorphous regions (Martin et al. (2005)). . . . .	32
2.14	Two electron diffraction patterns showing sharp rings in polycrystalline pure gold and broad ‘halos’ in amorphous PC61BM. . . . .	33
2.15	Experimental RDFs (from top to bottom) of a P3HT:PC61BM blend (blue solid line), neat P3HT (red solid line) with simulated RDF (red dashed line) and neat PC61BM (green solid line) with simulated PDF (green dashed line)(Mu et al., 2019). . . . .	35
2.16	(a) Variance as function of scattering vector magnitude ( $k$ ) for an amorphous silicon sample. (b) The origin of the speckle pattern in a dark field image. Bragg scattering from small crystalline domains in an otherwise amorphous solid give rise to local variations in the dark field image intensity (Voyles and Abelson, 2003). . . . .	38

2.17	Coherence volume for 100 kV hollow cone illumination superimposed on the atomic positions (open circles) within a silicon specimen viewed in the [100] direction. In these images grey represents regions where no interference with the central atom can take place during scattering. Bright and dark regions represent regions of constructive and destructive interference respectively. The outer angle of the hollow cone illumination is fixed at 200 mrad, while the inner angle in (a), (b) and (c) are 10, 50 and 100 mrad respectively (Treacy and Gibson, 1993). . . . .	39
2.18	The role of coherence volume (smaller shaded cylinder) and Airy disc (larger open cylinder) on scattering from two atom pairs. (a) shows the two atom pairs within the same coherence volume and Airy disc, while in (b) the two atom pairs are within the same Airy disc but different coherence volumes (the curve on the top represents the Airy disc profile). (c) is the same as (b) but with a larger coherence volume. See text for further details. . . . .	41
2.19	Schematic illustrating STEM fluctuation electron microscopy measurements. The specimen is probed by scanning the electron beam over the sample and collecting a diffraction pattern at each point (Treacy et al., 2005). . . . .	42
2.20	Plot of variance dependence on inner angle for an "amorphous" material as at large inner angle the curve drop to zero and show no crystallinity. See text for further details. . . . .	44
2.21	Schematic diagram that shows on the left hand side the electron energy-loss spectrometer mounted below the viewing screen of a TEM and at the right hand side shows the focussing lens action in the dispersion plane outside the spectrometer(Williams and Carter, 1978). . . . .	45

2.22	EELS spectrum plotted on a logarithmic intensity scale. The overall signal intensity drops rapidly with increasing energy loss above the plasmon peak. In most cases the zero-loss peak is several orders of magnitude more intense than the low energy-loss portion. At the high energy loss, the small ionisation edge peaks are shown (Williams and Carter, 1978). . . . .	46
2.23	The diagram shows the relationship between the empty and filled electronic state DOS and the fine structure in EELS. A smooth curve is drawn for the DOS below the Fermi energy ( $E_F$ ) for filled states while an oscillating shape is present for the empty states. The corresponding EELS edge shape is shown at the bottom of the figure (Williams and Carter, 1978). . . . .	48
2.24	EELS spectrum of carbon K-edge for (a) graphite and (b) diamond (Hamon et al., 2004). . . . .	49
2.25	EELS spectra for graphite as a function of the scattering angle ( $\theta$ ). The electron beam is incident normal to the graphite planes [001]. . . . .	50
2.26	Schematic of the multislice method showing the electron beam transferred through the specimen that is divided into many thin slices. $\Psi_o(\mathbf{r})$ and $\Psi_{exit}(\mathbf{r})$ are the electron incident and exit wave functions. . . . .	52
3.1	Schematic of a supercell 8 nm dimension and 20 nm thickness . . . . .	56
3.2	Multislice simulated convergent beam electron diffraction patterns . . .	57
3.3	An image of size $a \times b$ is sampled in a plane perpendicular to the microscope's optic axis. In real space, there are $(N_x) \times (N_y)$ pixels of size $(a/N_x) \times (b/N_y)$ , whereas in reciprocal space, the pixel size is $(1/a) \times (1/b)$ . The figure is for a non-square supercell (Kirkland, 2010). .	57

3.4	Simulated diffraction patterns obtained from an amorphous carbon supercell of dimension 8 x 8 x 20 nm, with a crystalline particle of radius 2nm at 10 nm depth (diamond cubic crystal structure). The electron beam parameters are 200 keV energy, Cs = 1.1mm and 643 Å underfocus (Scherzer condition). (a) and (b) show diffraction patterns with the probe incident along the crystalline and amorphous regions respectively. The central beam has been blocked to display the weaker scattering better.	60
3.5	Schematic showing the scattering inner angle $\alpha_{inner}$ and maximum simulated scattering angle $\alpha_{max}$ used for calculating the virtual dark-field intensity.	61
3.6	Virtual dark-field intensity as a function of scattering inner angle (mrad) for the crystalline and amorphous diffraction patterns in Figure 3.4.	62
3.7	Contrast as a function of scattering inner angle for the results shown in Figure 3.6.	62
3.8	Simulated diffraction patterns obtained from a 20 nm thick amorphous carbon specimen with a crystalline particle at 10 nm depth. A) 1 nm and b) 3 nm particle radius	63
3.9	Contrast as a function of scattering inner angle for carbon with particle radii 3 nm, 2 nm, 1 nm and 0.5 nm. The crystalline particles are at 10 nm depth in an otherwise 20 nm thick amorphous carbon specimen. B) Diffraction pattern for 3 nm radius particle showing the inner angle at maximum contrast.	64
3.10	Simulated diffraction patterns obtained from a 20 nm thick amorphous germanium specimen with a crystalline particle of radius a) 1 nm and b) 3 nm positioned at 10 nm depth.	65
3.11	Contrast as a function of scattering inner angle for germanium with particle radii 3 nm, 2 nm, 1 nm and 0.5 nm. The particles are at 10 nm depth in an otherwise amorphous specimen 20 nm thick.	66

3.12	Simulated diffraction patterns (log intensity scale) obtained from a 20 nm thick amorphous germanium specimen with a) 3 nm and b) 2 nm radius crystalline particle at 10 nm depth. . . . .	66
3.13	Simulated diffraction patterns (log scale) obtained from a 20 nm thick amorphous germanium specimen with a crystalline particle of radius a) 0.5 nm and b) 1 nm positioned at 10 nm depth. . . . .	67
3.14	Hollow-cone TEM dark-field image of amorphous Ge with 14.4 nm specimen thickness. The scale bar is 10nm (Treacy and Gibson, 1996). The circled particles were randomly chosen for particle size analysis. . . . .	68
3.15	Contrast as a function of scattering inner angle for carbon at depths 3 nm, 10 nm and 17 nm in a 20 nm thick amorphous specimen. The particles size is a) 2 nm and b) 3 nm. . . . .	69
3.16	Schematic illustrating the effect of geometric spreading of a STEM probe with 5.3 mrad semi-convergence angle for particles located at different specimen depths. The diagram is not drawn to scale. . . . .	70
3.17	Contrast as a function of scattering inner angle for Ge at depths 3 nm, 10 nm and 17 nm in a 20 nm amorphous specimen. The particles radius is a) 2 nm and b) 3nm. . . . .	71
3.18	Contrast as a function of scattering inner angle for carbon at paracrystallinity displacements of 0 Å, 0.10 Å and 0.20 Å in a 20 nm thick amorphous specimen. The particles size is a) 2 nm and b) 3 nm. . . . .	72
3.19	Contrast as a function of scattering inner angle for Ge at paracrystallinity displacements of 0 Å, 0.10 Å and 0.20 Å in a 20 nm amorphous specimen. The particles radius is a) 2 nm and b) 3nm. . . . .	73
4.1	JEOL JEM-2100F TEM used for investigating NiO and TIPS pentacene thin-films. . . . .	78

4.2	Electron diffraction pattern for a [110] NiO grain. The STEM probe semi-convergence angle $\theta_{probe}$ is proportional to the unscattered beam radius, which can be calibrated using a known Bragg angle, such as $\theta_{111}$ . Also shown in the figure is the inner angle $\theta_{inner}$ for the ADF detector.	79
4.3	Example as-recorded diffraction pattern for NiO in 4D STEM. The figure is displayed on a square root intensity scale to highlight any weak scattering.	80
4.4	An example diffraction pattern of TIPS pentacene recorded by 4D-STEM, which shows faint streaks at high scattering angles. The figure is displayed on a square root intensity scale to highlight any weak scattering.	81
4.5	(a) Bright field and (b) dark field TEM images of NiO. The scale bar in each figure is 50 nm.	82
4.6	(a) Electron diffraction pattern of NiO. Miller indices for each of the rings is as indicated. (b) Plot of $(1/d_{hkl})$ vs $\sqrt{h^2 + k^2 + l^2}$ , where $d_{hkl}$ is the inter-planar spacing of the $(hkl)$ crystallographic plane.	83
4.7	Histogram plot showing grain size data (diameter) for 100 grains.	83
4.8	STEM DF images for NiO at a) the smallest inner angle of 6 mrad and b) the largest inner angle of 45 mrad. The scale bar is 100 nm.	84
4.9	Intensity variance as function of inner angle for the NiO thin-film sample. For all data points other than 18 mrad the error bar is smaller than the data point marker.	85
4.10	Variation of ADF detector outer angle as a function of inner angle for a JEOL JEM-2100F TEM.	86
4.11	4D STEM electron diffraction pattern for NiO acquired at spot size 9 and aperture C2-1. The red and yellow circles represent virtual apertures for generating bright-field and dark-field images. The figure is displayed on a square root intensity scale to highlight any weak scattering.	87

4.12 NiO 4D STEM virtual a) bright-field and b) dark-field images for C2-1 aperture. The scale bar is 100 nm and the sampling is 200 x 200 pixels.	88
4.13 NiO 4D STEM virtual a) bright-field and b) dark-field images for C2-3 aperture. The scale bar is 100 nm and the sampling is 200 x 200 pixels.	88
4.14 4D STEM dark-field intensity variance as function of virtual detector inner angle for the NiO thin-film sample. . . . .	89
4.15 (a) Schematic structure of the TIPS-pentacene molecule showing the conjugated $\pi$ -electron density on the TIPS pentacene. (b) Assembly of TIPS pentacene molecules in a triclinic crystal structure; (Eggeman et al., 2013). . . . .	90
4.16 TEM image of a) drop cast and b) spin coating TIPS pentacene. The scale bar is 2 $\mu\text{m}$ for drop casting and 0.2 $\mu\text{m}$ for the spin coating image.	91
4.17 a) Example 4D STEM electron diffraction pattern for drop cast TIPS pentacene. The yellow circles represent virtual apertures for generating Bragg reflection dark-field images. The green circles represent virtual apertures for the diffuse intensity streaks. b) The diffraction pattern for drop cast TIPS pentacene in the [001] orientation reported in (Eggeman et al., 2013). Origin of streaking in TIPS pentacene shows c) displacements along the long axis of the pentacene molecule creates a range of interplanar angles ( $\delta$ , $\epsilon$ , $\theta$ ) and interplanar distances (l, m, n) and d) in reciprocal space this gives rise to a diffuse scattered streak. c) The diffraction pattern for drop cast TIPS pentacene in the [001] orientation reported in (Eggeman et al., 2013). . . . .	93
4.18 TIPS pentacene dark field images generated via 4D STEM virtual apertures positioned on a) $g_1$ and b) $g_2$ reflections in Figure 4.17a. . . . .	94
4.19 TIPS pentacene dark field images of the diffuse streak, generated using the virtual $g_3$ , $g_4$ and $g_5$ in Figure 4.15. . . . .	95

4.20	a) Diffraction pattern of spin coated TIPS pentacene, where the sample is crystalline and shows sharp Bragg reflections. The circled reflection is used to generate the virtual dark field image in b). The circled grains in b) are used to calculate the grain size . . . . .	95
4.21	4D STEM dark-field intensity variance as function of virtual detector inner angle for drop cast TIPS pentacene thin-film sample. . . . .	97
4.22	4D STEM dark-field intensity variance as function of virtual detector inner angle for spin coated TIPS pentacene thin-film sample. Spot size number 9. . . . .	98
5.1	Three structures of the benzene/benzene intermolecular stacking; a) face-to-face, b) parallel-displaced and c) edge-to-face (Wheeler, 2011). .	101
5.2	The four categories of $\pi$ -stacking in conjugated small molecules: herringbone, slipped, brick layer and cofacial stacking (Yao et al., 2018). . .	101
5.3	TEM image of graphite at a) $0^\circ$ and b) $60^\circ$ specimen holder tilt. EELS data was acquired from the circled area in each figure. At $0^\circ$ tilt the c-axis of the graphite flake is parallel to the electron optic axis. . . . .	104
5.4	TEM EELS carbon K spectra for graphite recorded at specimen tilts of a) $0^\circ$ and b) $60^\circ$ . The $\pi^*$ and $\sigma^*$ features are indicated in each figure. At $0^\circ$ tilt the c-axis of the graphite flake is parallel to the electron optic axis.	105
5.5	The $\pi^*/\sigma^*$ intensity ratio in TEM EELS spectra of graphite as a function of specimen tilt angle. The line connecting the data points is a guide to the eye. . . . .	106
5.6	Diagram showing the relation between scattering angle ( $\theta$ ), scattering vector ( $\vec{q}$ ) and the incident and inelastically scattered electron wavevectors, $\vec{k}$ and ( $\vec{k}'$ ) respectively Leapman et al. (1983). . . . .	107
5.7	Energy loss spectrum of graphite carbon K-edge recorded using STEM EELS for a) $0^\circ$ and b) $60^\circ$ specimen tilt. Both graphs show $\pi^*$ and $\sigma^*$ features. . . . .	108

5.8	The $\pi^*/\sigma^*$ ratio in STEM EELS as a function of specimen tilt angle. The line connecting the data points is a guide to the eye. The error bar is very small. . . . .	109
5.9	Diffraction pattern and TEM image showing bend contours in TIPS pentacene at a) 0 seconds and b) after few seconds respectively. . . . .	110
5.10	Dark field STEM images showing TIPS pentacene a) before and b) after acquiring an EELS spectrum image over the boxed region with STEM probe spot size number 5 as well as c) and d) for spot size number 4. The scale bar is 50 nm. . . . .	112
5.11	Energy loss spectrum of TIPS pentacene carbon K-edge recorded using STEM probe spot size numbers a) 5 and b) 4. The EELS spectra were extracted from a single ‘point’ in a spectrum image data set. . . . .	113
5.12	TIPS pentacene $\pi^*/\sigma^*$ ratio maps calculated from EELS spectrum images acquired with STEM probe spot size number a) 5 and b) 4. . . . .	114
6.1	A diagram showing the basic features of a) scintillator based and b) direct electron detectors. Each schematic shows electrons passing through the detector. . . . .	119

---

# List of Tables

1.1	Comparison between band and hopping transport . . . . .	15
-----	---	----

---

# Organic thin films

## 1.1 Introduction to organic materials

Organic electronics is a branch of modern electronics that deals with carbon-based materials. In the late 1970s, the field of organic electronics received widespread attention due to the discovery of  $\pi$  conjugated polymers such as polyacetylene (a flat polymer with  $120^\circ$  bond angle) and polythiophene (Figure 1.1) shows some common conductive polymers) (Brédas et al., 2018). A polymer is a material that contains a chain of repeating molecular structure called a "monomer". In 1976 (Heeger, 2001) three scientists, Heeger, MacDiarmid, and Shirakawa found that doping (trans) polyacetylene resulted in a high conductivity (Shirakawa et al., 1977) and were awarded the Nobel Prize in Chemistry in 2000. They discovered that oxidation with chlorine, bromine or iodine vapour made polyacetylene films  $10^9$  times more conductive than the original polymer. Since the discovery of polyacetylene, various important conductive polymers have been investigated continuously such as polythiophene (PT), poly(3,4-ethylenedioxythiophene) (PEDOT) and poly(p-phenylene vinylene) (PPV). Polyacetylene as a semiconductor has a conductivity between  $7 \times 10^{-11}$  to  $7 \times 10^{-3} \text{ S m}^{-1}$  (Saldivar-Guerra and Vivaldo-Lima, 2013) and (poly(3,4-ethylene dioxythiophene) (PEDOT), has conductivities in excess of  $300 \text{ S m}^{-1}$  (Geoghegan and Hadziioannou, 2013; Ravichandran et al., 2010), compared to conductivity of silicon  $4.3 \times 10^{-4} \text{ S m}^{-1}$  (Nair and Deepa, 2008). A lot of re-

search teams in both academia and industry have been investigating  $\pi$  conjugated polymers and small molecules to gain the benefit of their unique optical and semi-conducting properties in the fields of plastic electronics and photonics (Facchetti, 2011). The hope of plastic semiconductors resulted in the study of these polymer materials as a viable alternative to more traditional inorganic silicon-based material.

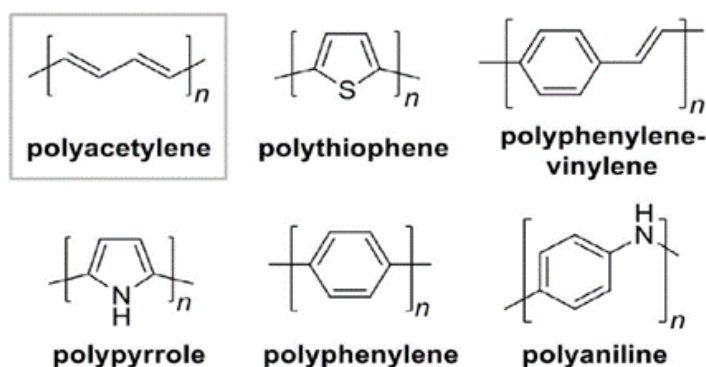


Figure 1.1: Some examples of conductive polymers. The square bracket indicates the monomer and the subscript 'n' refers to the number of repeating units (Rasmussen, 2014).

Since silicon-based electronics is highly successful and rapidly developing it is worth asking what are the potential benefits of organic electronics? The answer is that organic materials are low cost, easy to process and can be fabricated on flexible or curved substrates (Geoghegan and Hadziioannou, 2013; Kulovits et al., 2012). With silicon it is very difficult to change or upgrade the manufacturing processes from one chip design to another, while on the other hand polymers are easy to process (Geoghegan and Hadziioannou, 2013). Furthermore, significant energy is required to extract electronic grade purity silicon from its raw material (i.e. sand) and very expensive clean room facilities and vacuum chambers are required for device fabrication (Geoghegan and Hadziioannou, 2013). Organic electronics devices include organic photovoltaics (OPVs), organic light-emitting diodes (OLEDs), and organic field-effect transistors (OFETs). Organic materials, in the form of polymers and small molecules, are used as the absorber layer in OPVs, the emissive

layer in OLEDs and channel region in OFETs (Anthony, 2006). Usually optimal performance of the polymer is obtained by processing from solution (Geoghegan and Hadziioannou, 2013) and small molecules are thermally evaporated in vacuum (Chiang, 2007; Koch, 2007).

## 1.2 Conjugated polymers and small molecules

### 1.2.1 Band structure in organic materials

Benzene can be drawn with alternating single and double covalent bonds and this can be done in two equivalent ways as shown in Figures 1.2(a) and 1.2(b). The electrons in benzene are therefore delocalised and are represented schematically in Figure 1.2(c). By adding more of benzene molecules we can create a macromolecule. The delocalised electrons (called  $\pi$  electrons) should therefore be able to travel along the macromolecule, from one end to the other, giving rise to conductivity. Conductivity of an organic semiconductor can be increased by heating, illumination, doping, or other processes that increase the charge carrier density. The electrical conductivity can be carried by two types of charge carriers, electrons, and holes. Moreover, their densities can be increased selectively by n-doping or p-doping, respectively.

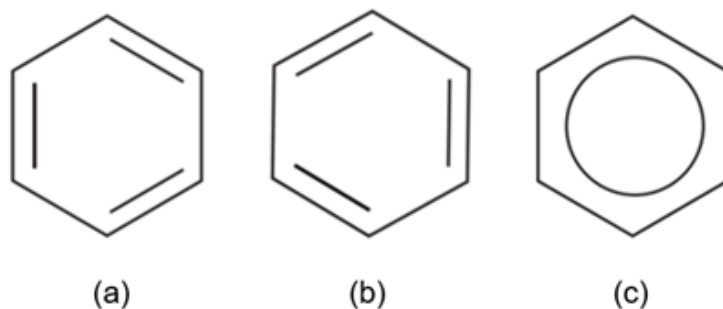


Figure 1.2: Two alternative structures of benzene with single and double covalent bonds are shown in a) and b). c) Shows the equivalent structure with the delocalised electrons moving around the molecule with no impediment (Geoghegan and Hadziioannou, 2013).

Conjugated polymers are organic macromolecules that are characterised by a back-

---

bone chain of alternating single and double carbon bonds, similar to benzene discussed above (see Figure 1.3). Both single and double bonds contain a localised  $\sigma$ -bond, which forms a strong chemical bond. Moreover, each double bond also includes a delocalised  $\pi$ -bond (Ravichandran et al., 2010). The  $\pi$ -bond is what gives the conjugated polymer its conductivity.

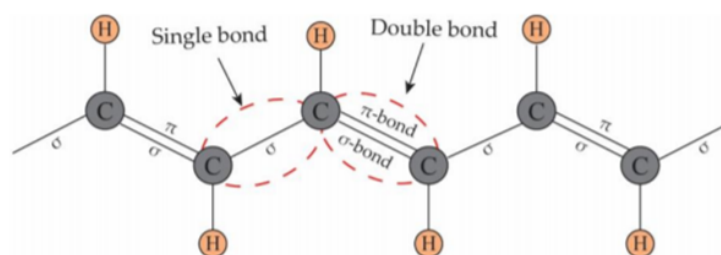


Figure 1.3: The structure of polyacetylene, containing alternating single and double bonds (Le et al., 2017)

The fundamental optoelectronic properties for conductive polymers and small molecules are governed by  $\pi$ . Carbon is tetravalent because of 2s and 2p valence electrons. Moreover, the chemistry of bonding in polymer or small molecules is formed from linear combination of atomic 2s and 2p orbitals (Koehler and Baessler, 2015). This process is called ‘hybridisation’. There are two types of hybridisation that are possible from the electron configuration, which are  $sp^2$  and  $sp^3$ . In  $sp^3$  the 2s electron is hybridised with three 2p electrons to give four covalent  $\sigma$ -bonds. Because the  $\sigma$ -bonds are localised electrical conductivity is poor. This explains why carbon in the form of  $sp^3$  diamond is an insulator. The second type of hybridisation is  $sp^2$  which is formed by overlap of a 2s electron with two 2p electrons to give three  $\sigma$ -bonds and one  $\pi$ -bond from the unmixed  $2p_z$  orbital. The  $p_z$  orbitals along the carbon backbone overlap leading to electron delocalisation and a small band gap (Heeger, 2001). The electron delocalisation is what gives the higher electrical conductivity in organic materials. Thus, conjugated double bonds allow a flow of electric charge. A typical example of molecule with  $\sigma$ -bonds is ethane ( $C_2H_6$ ), while ethene ( $C_2H_4$ ) has a double bond between the carbon atoms and therefore

contains a mixture of  $\sigma$ - and  $\pi$ -bonds as shown in Figure 1.4.

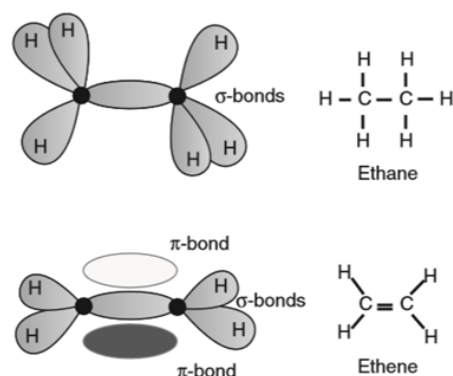


Figure 1.4: Ethane molecule consisting of six hydrogen atoms and two  $sp^3$  hybridised carbon atoms and ethene consisting of four hydrogen atoms and two  $sp^2$  hybridised carbon atoms (Koehler and Baessler, 2015).

In an inorganic semiconductor there are conduction and valence bands because of the crystalline state. The band structure in a conjugated organic material is similar to inorganic but instead of having conduction and valance bands,  $sp^2$  carbon induces a small band gap between the highest occupied molecular orbital ( $\pi$  bonds) and lowest unoccupied molecular orbital ( $\pi^*$  anti-bonds) as can be seen in Figure 1.5. The highest occupied molecular orbitals and lowest unoccupied molecular orbitals are abbreviated as HOMO and LUMO respectively.

## 1.2.2 Examples of conjugated polymers

Polymerisation of ethene results in polyacetylene, which is an example of conjugated polymer (see Figure 1.6). A conjugated polymer results in overlapping  $p_z$  orbitals that create a system of delocalised electrons. However, conjugation by itself is not enough to make a highly conducting polymer without doping (i.e. oxidation or reduction) (Geoghegan and Hadziioannou, 2013). Under an electric field delocalised  $p_z$  electrons in the anti-bonding LUMO level are able to travel along the chain of the conjugated polymer giving rise to electrical conductivity.

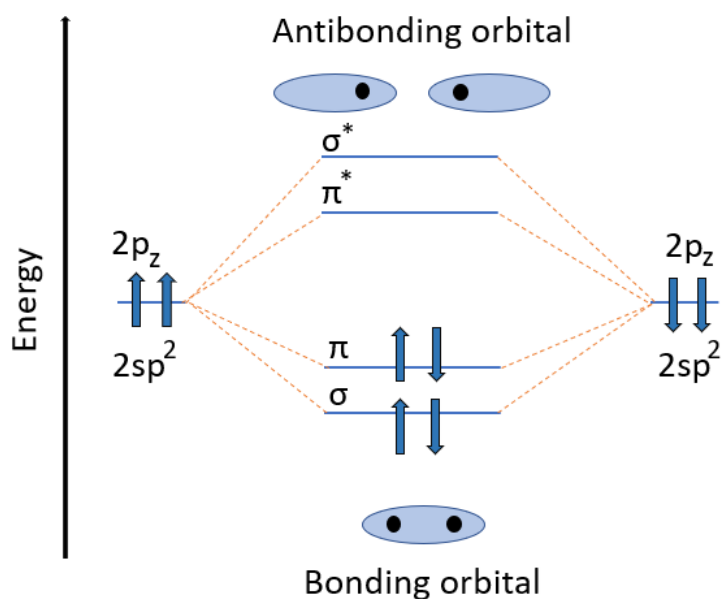


Figure 1.5: Energy level diagram illustrating the formation of  $\sigma$  and  $\pi$ -bonds from atomic orbitals for ethene.

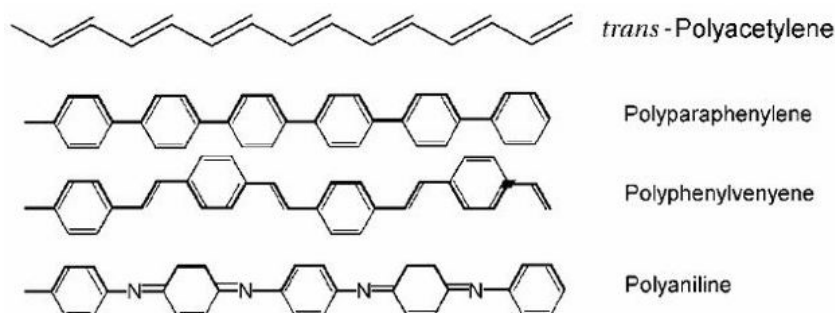


Figure 1.6: Chemical structures of some undoped conjugated polymers (Krieger, 1999).

### 1.2.3 Examples of small molecules

Small molecule semiconductors have been receiving growing attention due to their unique electrical and optical properties. Small molecules offer advantages over polymeric materials in terms of the simplicity of synthesis and purification, which greatly improves fabrication reproducibility, as well as possessing a greater tendency to self-assemble into ordered domains, which leads to high charge carrier mobility. A fullerene ( $C_{60}$ ), or informally called ‘buckyball’, is a small molecule consisting of fused rings of five to seven carbon atoms connected by single and

double bonds. A common derivative of  $C_{60}$ , used widely in organic electronics (e.g. OPV), is [6,6]-phenyl  $C_{61}$ -butyric acid methyl ester (PCBM), shown in Figure 1.7. PCMB gets its conductivity from delocalised  $p_z$  electrons.

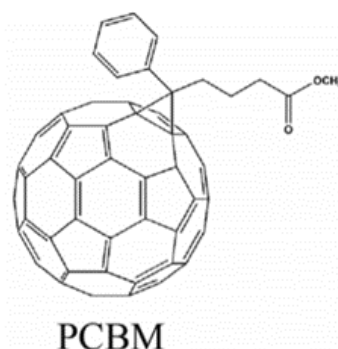


Figure 1.7: Chemical structure of PCBM (Huang et al., 2015).

Other examples of planar small molecules widely used in organic electronics include the acene group and rubrene (see Figure 1.8). Acenes are a group of organic compounds, classified within the category of polycyclic aromatic hydrocarbons (PAH), that consist of a continuous and linear fusion of benzene rings (Bettinger, 2010; Zade and Bendikov, 2010). For example, anthracene with formula  $C_{14}H_{10}$ , consists of three fused benzene rings, while tetracene and pentacene contain four and five rings respectively. The acenes are used extensively in OFET and OLED devices (Anthony, 2006). Rubrene (5, 6,11,12-tetraphenyltetracene) is a polycyclic aromatic hydrocarbon derived from tetracene and has applications in OLEDs (Anthony, 2008; Musa et al.; Paraskar et al., 2008).

#### 1.2.4 Optical excitation in conjugated systems

Organic semiconductors have the capacity to emit or absorb light of certain wavelengths, with many important applications. For example, the ability to emit light at a specified wavelength is the basis of organic LEDs. The size of the band gap plays an important role in determining the absorption and emission of light. The relev-

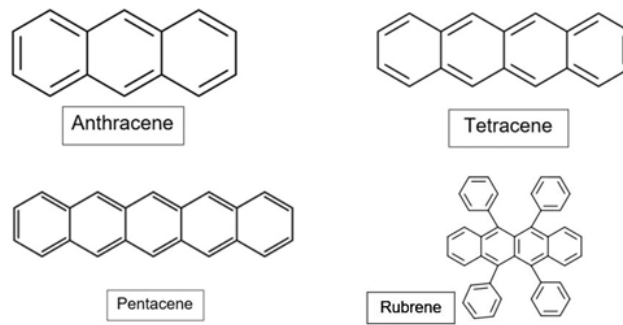


Figure 1.8: Chemical structures of some common planar organic molecules.

ant energy levels in an organic semiconductor are the HOMO and LUMO, which are separated by the band gap (Figure 1.5). When an electron is excited from the HOMO to LUMO, such as during absorption of a light photon, there will be a strong Coulombic attraction between the promoted electron and the hole that is left behind. This attraction means that the electron and hole form a bound quasi-particle known as an exciton. Excitons have important implications for OPV devices. Since they are charge neutral they must be dissociated into free carriers (i.e. electrons and holes) in order to extract an electric current. In OPVs this is achieved by creating a finely mixed ‘blend’ of two organic materials, called ‘donor’ and ‘acceptor’, which have an offset in HOMO and LUMO levels (see Figure 1.9). Excitons that diffuse to the donor-acceptor interface can dissociate to lower their energy, such that the electron is injected into the acceptor phase with lower LUMO level, leaving behind the hole in the donor phase with higher HOMO level. P3HT-PCBM is a typical OPV blend, where the P3HT polymer is the donor phase and PCBM small molecule the acceptor.

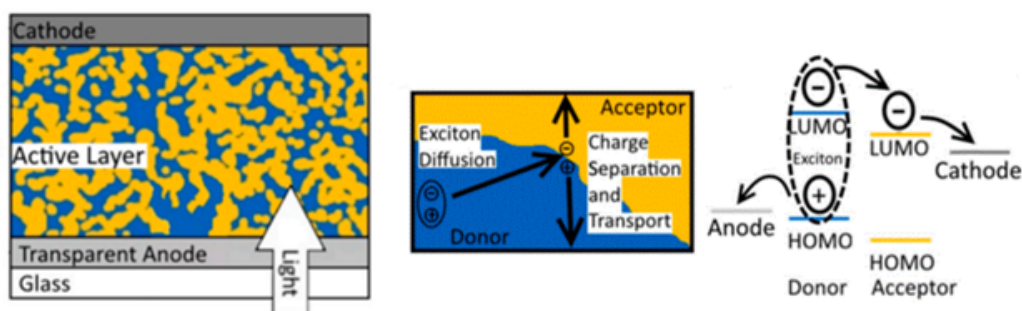


Figure 1.9: Schematic showing exciton formation and dissociation in OPV donor-acceptor blend (Haruk and Mativetsky, 2015).

## 1.3 Microstructure of organic materials

### 1.3.1 Semi-crystalline

Organic materials such as polymers are typically semi-crystalline material. They have the morphology of both crystal and amorphous regions. In the crystal, the electronic structure represents an ordered phase that is similar to an inorganic semiconductor such as silicon. However, in the amorphous (disordered) phase there is no periodicity in the structure, as shown in Figure 1.10. The reason for having both regions in polymers is because the conjugation has much more conformational freedom (Noriega et al., 2013), which means that the polymer backbone is not rigid. Poly (3-hexylthiophene-2,5-diyl) or P3HT is a semi-crystalline polymer, widely used in bulk heterojunction OPV, exhibiting both crystalline and amorphous phases. The monomer in P3HT consists of an aromatic ring of one sulphur atom and four carbon atoms, with a  $C_6H_{13}$  alkyl side group for doping (see Figure 1.11a). P3HT in the crystalline phase can organise into a lamellar structure of co-facially stacked conjugated sheets (Figure 1.11b). There are overlapping  $\pi$ -orbitals in between the lamellae. Crystalline P3HT exhibits anisotropic carrier mobility, such that the highest mobility is along the chain backbone [001] direction, then the  $\pi$ -stacking [010] direction and the lowest charge carrier mobility is along the alkyl-stacking [100] direction.

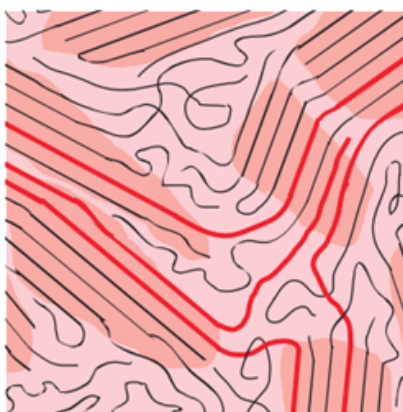


Figure 1.10: Schematic of the microstructure of a semi-crystalline polymer film, where the lamellae ordered areas are crystalline regions and the area surrounding it is amorphous (Callister et al., 2007).

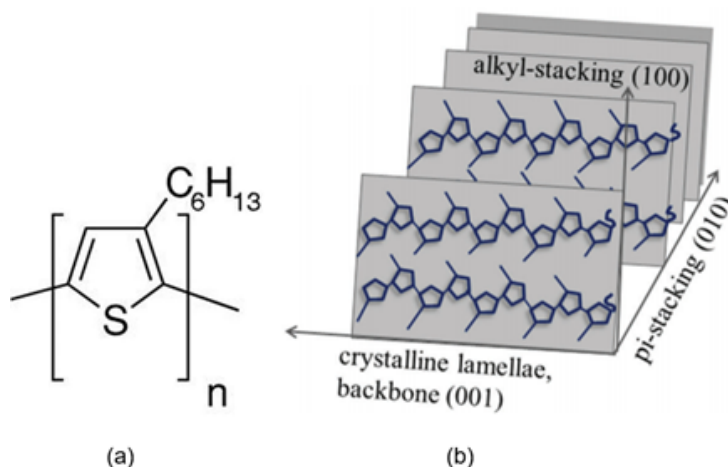


Figure 1.11: a) Monomers of P3HT and b) lamellar structure of co-facially stacked conjugated sheets, with  $\pi$ -stacking direction indicated (Chowdhury et al., 2017)

### 1.3.2 Poly-crystalline

Poly-crystalline are fully crystalline materials with different orientation between neighbouring 'grains'(Figure 1.12). Both the grains and grain boundaries determine the properties of these materials. The grain size can vary from a few hundred nanometers to several micrometers. Small molecules (e.g. pentacene) are examples of organic poly-crystalline materials.

In Figure 1.12(a) grains are the region of space occupied by a continuous crystal lattice, while the boundaries between neighbouring grains are grain boundaries.

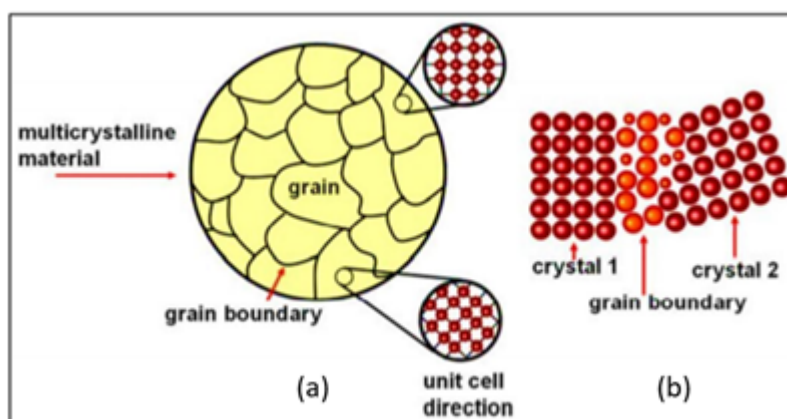


Figure 1.12: Grain boundaries in a polycrystalline material, a) macroscopic and b) atomic scale (Nagra, 2019).

Each grain has a particular crystal orientation. Figure 1.12(b) represents two grains of different orientation and the grain boundaries that arise at the interfaces between the grains.

Poly-crystalline small molecular thin-films are mainly grown by thermal evaporation or vapour phase deposition. The morphology of these materials largely affects their performance with charge carrier mobility being highly sensitive to crystallite grain size (Knipp et al., 2003). The grain size and morphology can also be controlled by the deposition technique (e.g. temperature and duration of thermal annealing) and substrate surface (Knipp et al., 2003; Dimitrakopoulos and Malenfant, 2002). Pentacene for example forms highly ordered poly-crystalline thin-films (Chen et al., 2010), where the pentacene molecules form a triclinic crystal structure that grows in the form of dendritic grains (Knipp et al., 2003) (Figure 1.13). Moreover, the molecules within each layer adopt a face-on-edge herringbone arrangement.

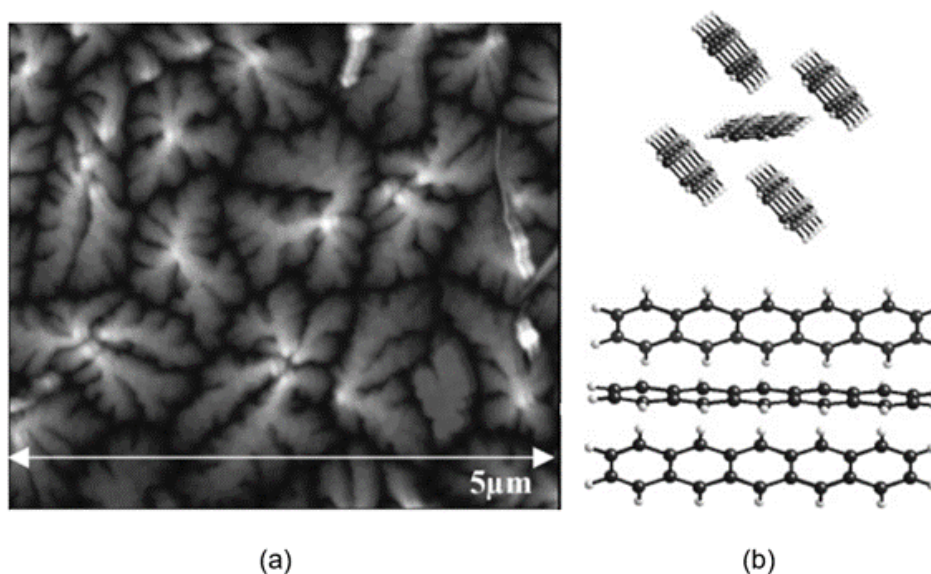


Figure 1.13: a) Atomic force microscopy (AFM) image of thermally evaporated pentacene films (Stadlober et al., 2003). The pentacene has a dendritic structure and preferential orientation. The grain boundaries are the regions between the pentacene crystals. b) Pentacene and its crystal packing showing predominant edge-to-face interactions (Anthony, 2006).

### 1.3.3 Polymer fullerene blends

Blends consisting of several different materials are also widely used in organic electronics. Examples include the P3HT:PCBM polymer/small molecule blend for OPV applications. There are several strategies that can be used to manipulate and control the morphology of organic blends, including variations in the thin-film deposition conditions and post processing techniques, such as thermal and solvent vapour annealing (Verploegen et al., 2012; Thompson and Fréchet, 2008). For example, during thermal annealing, PCBM is found to aggregate and form crystals with increasing annealing time. Likewise solvent annealing, where the as-cast film is exposed to solvent vapour, can also influence the morphology and crystalline order of the P3HT: PCBM film and therefore increase the conductivity (Wang et al., 2016). Solvent introduced into the film during this procedure can help re-arrangement and/or diffusion of organic molecules into aggregates or crystals. Morphology changes during solvent annealing are illustrated schematically

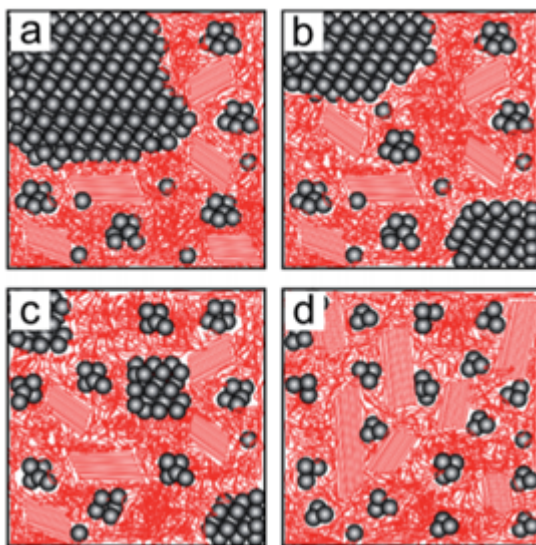


Figure 1.14: Schematic morphology of P3HT:PCBM films post-treated with different solvent vapors, a) chlorobenzene, b) toluene, c) xylene and d) dichlorobenzene. The grey spheres indicate PCBM, red tangled lines represent amorphous P3HT and red parallel lines are P3HT crystallites (Wang et al., 2016).

in Figure 1.14. The grey dots represent PCBM aggregates, while the red tangled lines represent the amorphous P3HT and the parallel lines the crystalline P3HT phase. The phase separation of P3HT and PCBM causes a domain structure in the range for efficient exciton dissociation (subsection 1.2.2), although the different solvent vapour treatments in Figure 1.14 show slightly different lateral structure sizes. Controlling the molecular packing within each domain and the orientation of the crystallites within the domains are all critical for optimising the performance of organic devices.

Understanding the morphology of the organic material (semi-crystalline or polycrystalline) is imperative to comprehend the charge transport mechanisms and other materials properties. There are many ways to study and probe the morphology of organic materials such as X-ray diffraction (XRD) (Salleo et al., 2010), grazing incidence X-ray scattering (GIXS) (Verploegen et al., 2012), atomic force microscopy (AFM) and electron microscopy (Wang et al., 2016; Zheng et al., 2011).

### 1.3.4 Charge transport and Mobility

Charge transport mechanisms describe the electric current flow through a given medium. Amorphous materials have strong localisation effects, which reduce the mobility of charges. Charge is typically transported via hopping, where charge carriers jump from one trap energy level to another within the broadened density of states, under the influence of a driving force such as an applied voltage (Figure 1.15).

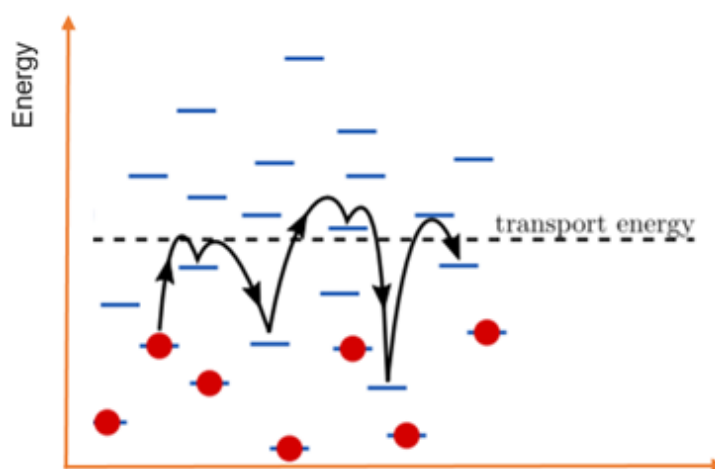


Figure 1.15: Charge transport via hopping to localised trap states within the forbidden gap (Oelerich et al., 2014).

Hopping between molecules is related to the intermolecular overlap of neighbouring molecular orbitals and is mainly dependent on how molecules pack with respect to each other. Furthermore, conjugated polymers are typically longer than their persistence length, which means the charge is not expected to be able to travel the full length of a polymer chain before having to hop to a neighbouring polymer macromolecule. Therefore the chain packing is critical to charge transport (Kline and McGehee, 2006). In poly-crystalline material, the charge is transported within individual grains via band transport and is similar to inorganic semiconductors when an electric field applied. Table 1 below shows the difference between the two types of transport.

Another important parameter is the carrier mobility ( $\mu$ ), which governs the drift

velocity of the carriers under an applied electric field. Because of large energetic disorder, the mobility of organic polymers is generally low and only on the order of  $1 \text{ cm}^2 \text{ V}^{-1} \text{ s}^{-1}$ ; for example, pentacene has values of approximately  $1.5 \text{ cm}^2 \text{ V}^{-1} \text{ s}^{-1}$  by organic vapour phase deposition (Forrest, 2004) and  $5 \text{ cm}^2 \text{ V}^{-1} \text{ s}^{-1}$  in OFET devices (Salzmann et al., 2008). Tetracene single crystals have a mobility of  $0.4 \text{ cm}^2 \text{ V}^{-1} \text{ s}^{-1}$  (Poelking et al., 2014). The magnitude of the mobility in organic materials is very low compared to conventional inorganic materials such as silicon ( $10^3 \text{ cm}^2 \text{ V}^{-1} \text{ s}^{-1}$ ) (Kulovits et al., 2012; Dimitrakopoulos and Malenfant, 2002). (Kim et al., 2007) investigated the effect of different solvents on the properties of organic thin-film transistors (OTFTs) made with TIPS-pentacene as an active layer. They looked at how the use of different solvents (i.e. chlorobenzene, 1,2-dichlorobenzene and o-xylene) affects the morphology and crystallinity of the TIPS-Pentacene film, as well as the electrical performance of the resulting OTFTs. They find that the choice of solvent has a significant impact on the morphology and crystallinity of the TIPS-Pentacene film, as well as on the performance of the resulting OTFTs. Chlorobenzene results in larger dendritic grain sizes ( $\sim 10 \text{ }\mu\text{m}$  or larger; see Figure 2 in (Kim et al., 2007)) and higher crystallinity, which give a better electrical performance (e.g.  $0.04 \text{ cm}^2 \text{ V}^{-1} \text{ s}^{-1}$ ) in OTFT applications.

<b>Parameter</b>	<b>Band transport</b>	<b>Hopping transport</b>
<b>Examples</b>	Crystalline semiconductors	Semi-crystalline and amorphous semiconductors
<b>Underlying mechanism</b>	Delocalised wave functions over the entire molecule	Transition between localised trap sites via tunneling or overcoming potential barriers (hopping)
<b>Mobility</b>	Usually larger than $1 \text{ cm}^2/\text{Vs}$ ; independent of electric field; decreases with increasing temperature	Usually smaller than $0.01 \text{ cm}^2/\text{Vs}$ ; depends on electric field; increases with increasing temperature

Table 1.1: Comparison between band and hopping transport

## 1.4 Pair Correlation Functions

Pair correlation functions describe the spatial distribution of atoms in a solid. A simple example is the radial distribution function (RDF or  $g_2(r)$ ), which is the probability of finding two atoms separated by radial distance 'r'. In an ideal gas the RDF is equal to unity. This represents the fact that it is equally probable to find an atom at any given value of r. For a crystalline material with long range order the nearest neighbour positions are well defined. Therefore the RDF consists of a series of sharp peaks at discrete values of r corresponding to the nearest neighbour distances. In amorphous materials however there is no long-range correlation between atom positions and no translational symmetry (Meyers and Myers, 1997). This means that the peaks in the RDF will be broadened, as shown in Figure 1.16. The first RDF peak is relatively sharp and occurs when r is of the order of the molecular diameter. The area under the peak is proportional to the number of nearest neighbours for the particular molecule. Moreover, if we integrate the RDF between the limits 0 and r, we obtain (to within a constant) the number of atoms contained within a sphere of radius (r) (Lu and Hu, 2008).

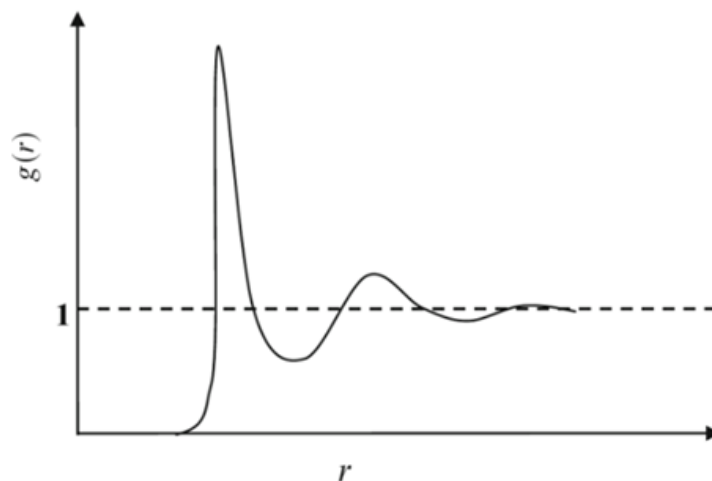


Figure 1.16: The radial distribution function  $g_2(r)$  for a disordered solid. The peaks and troughs represent atom correlations that deviate from an ideal gas, which has a constant  $g_2(r)$  value of unity

Diffraction patterns measure the RDF (see section 2.4), which for a random amorphous material gives information only on first and second nearest neighbours. This is because beyond the first few nearest neighbour atom shells, random changes in the bond length and angle in the amorphous material renders the RDF featureless (Figure 1.16). Therefore  $g_2(r)$  can only give us information on the short range order in a disordered solid. Higher order correlations, such as  $g_3(r_1, r, \theta)$  and  $g_4(r_1, r_2, r, \theta)$  give us the medium range structural order (Lee et al., 2010; Voyles and Abelson, 2003). Here we have a pair of atoms at the origin that are separated by distance  $r_1$  as shown in Figure 1.17(b):

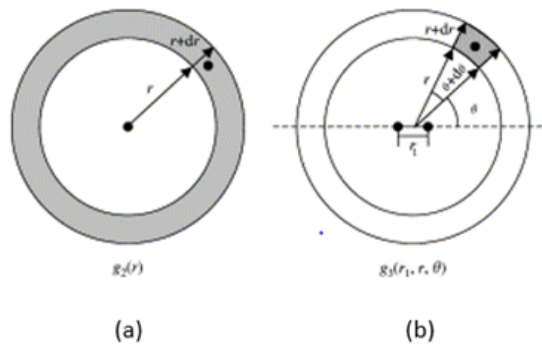


Figure 1.17: Two concentric spherical shells where the grey colour indicates the effective search volume for the correlation function. (a)  $g_2(r)$  searches the volume between  $r$  and  $r + dr$  within the shell. (b)  $g_3(r_1, r, \theta)$  searches a small portion of volume that is between  $r$  and  $r + dr$  about  $\theta$  and  $\theta + d\theta$  where  $\theta$  is measured with respect to  $r_1$  that is between to atoms (Voyles and Abelson, 2003).

$g_3(r_1, r, \theta)$  measures the probability of finding an atom at distance  $r$  and angle  $\theta$  from the atomic pair at the origin. Compare Figures 1.17(a) and 1.17(b); in the first case we only have one atom, and the only variable is the distance  $r$  in the inner sphere (the search area in Fig 1.17a is indicated in grey). In the second case, we are restricted by two atoms at the origin and instead of integrating over the whole sphere, we have only selected the angular range  $d\theta$  about  $\theta$ . In the latter case there are many more conditions imposed and our search volume has gone from the surface of the inner sphere to a smaller part of it. This means there is less chance of information being ‘washed away’, so that peaks beyond second nearest neighbours

are visible in  $g_3(r_1, r, \theta)$  and  $g_4(r_1, r_2, r, \theta)$  (Adachi et al., 2010). These extra peaks probe the medium range order (MRO) in the sample. According to Voyles and Abelson (Adachi et al., 2010) the MRO is due to a non-uniform of distribution of dihedral angles. If the material was similar to a continuous random network, we will have a uniform distribution of dihedral angles (Figure 1.18). However, if we do not have a uniform distribution, we get medium range order. At large distance changes in the dihedral angle causes peaks in  $g_2(r)$  to be washed out, but not for  $g_3(r_1, r, \theta)$  and  $g_4(r_1, r_2, r, \theta)$  due to the more restrictive conditions.

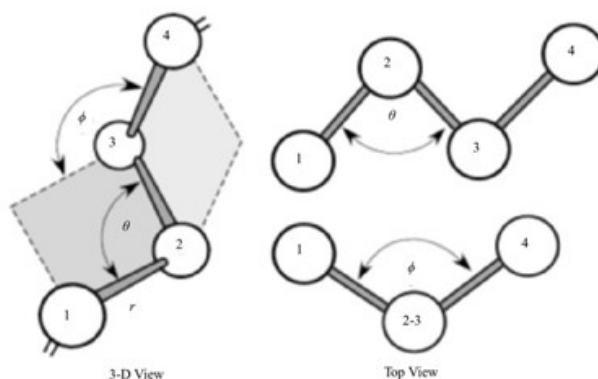


Figure 1.18: The dihedral angle is defined as the angle between two planes, each containing at least three atoms with two atoms in common. In the above figure  $\theta$  is the bond angle and  $\phi$  is the dihedral angle (Abdullah et al., 2015).

## 1.5 Motivation of project

Despite the availability of several techniques, such as atomic force microscopy (AFM) and grazing incidence X-ray diffraction (GI-XRD), to study the morphology of thin films, they do not meet certain requirements. For example, AFM only studies the surface morphology of the material (Salleo et al., 2010) and grazing incidence XRD requires use of expensive synchrotron sources which are not readily accessible. In addition, the unit cell of the polymer is large in real space, so the XRD peaks will be closely spaced in reciprocal space. Other techniques are fluctuation optical microscopy (FOM) and fluctuation X-ray microscopy (FXM) (Fan et al., 2004), but they analyse the structural order larger than a few nanometers and require bulk

samples. Furthermore, because of having a large wavelength, there will be a large probe size as well as a large penetration depth (Sawyer et al., 2008; Williams and Carter, 2009), meaning that it is difficult to extract truly local information about the sample. Therefore in this project we develop a fluctuation based technique for studying the morphology of these materials using scanning transmission electron microscopy (STEM). This has the advantage of providing direct real space images of the ordering at high spatial resolution, and only requires a transmission electron microscope which is available in most labs. The fluctuation STEM method developed here is described in section 2.5.2 and can be used to probe the MRO of organic electronic thin films.

---

# Electron Microscope

## 2.1 Introduction

Electron microscopy (EM) is a technique for obtaining high resolution images by using a beam of accelerated electrons as a source of illumination. Electrons were known as particles, but in 1925 Louis de Broglie postulated that electrons can behave as both a particle and a wave (Bäcke et al., 2017; Bush, 2015). He pointed out that an electron can behave similar to light and proposed the de Broglie wavelength ( $\lambda$ ) equation  $\lambda = h/p$ , where  $h$  is Planck's constant and  $p$  is the momentum of the electron. The wavelength of an electron with kinetic energy 200 keV is 0.025 Å and is therefore much shorter than light photons, so electron microscopes can achieve a higher resolution than light microscopes. The resolution is the minimum distance between distinguishable objects in an image. The imaging system's resolution is limited by diffraction in the absence of other lens aberrations (e.g. spherical aberration). Diffraction is determined by the finite aperture of the optical elements and can be explained by geometrical optics. When electrons are focused by an ideal lens with circular aperture, individual rays interfere with one another creating a radially symmetric beam profile, known as the Airy pattern or Airy disk (Figure 2.1). The radius of the Airy disk is defined as the distance from the central peak to the first intensity minimum. The equation for the Airy disk diameter ( $d$ ) is:

$$d = 1.22\lambda / \sin \alpha \quad (2.1)$$

where  $\lambda$  is the wavelength and  $\alpha$  is the semi-convergence angle imposed by the aperture.

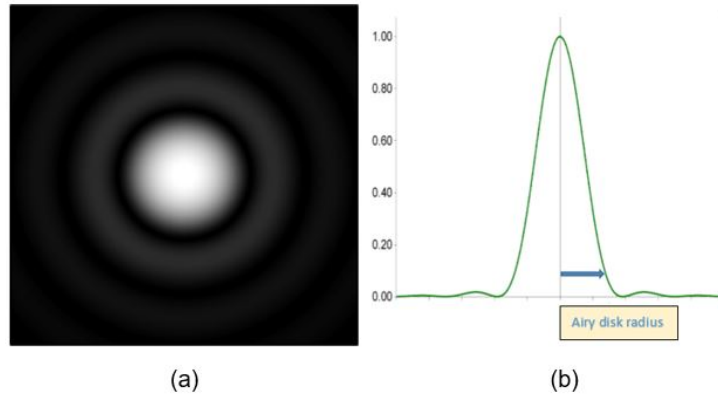


Figure 2.1: (a) Intensity profile of the Airy pattern. (b) Intensity plot along the radial direction, showing the Airy Disk radius (Graney, 2009).

One of the most important components in an electron microscope is the electron emitter or gun, which generates the electrons for specimen characterisation. There are important requirements for any electron emitter, such as a high brightness, high coherence, small energy spread and lifetime. Electron emitters are primarily divided into two types of sources; a thermionic (lanthanum hexaboride ( $\text{LaB}_6$ ) or tungsten filaments) and field emission source. The field emission source is also called a field emission gun (FEG). In thermionic emission the source is heated to very high temperature, so that the electrons gain enough thermal energy to overcome the work function and escape into vacuum. The electron source acts as the cathode and the escaped electrons are accelerated to the desired voltage by use of a positively biased anode. A FEG source consists of a tungsten single crystal with a highly sharpened tip (Figure 2.2). The principle behind field emission is that the strength of an electric field  $E$  applied by the first anode is increased at the sharp tip. This is described by the equation  $E=V/r$ , where  $V$  is the voltage of the first anode and  $r$  is the tip radius. The vacuum energy level decreases rapidly due to the strong electric field, such that the electrons can undergo quantum tunneling,

rather than overcome the work function barrier (Figure 2.2b). The second anode in the FEG source is responsible for accelerating the electrons to their final energy (Figure 2.2a).

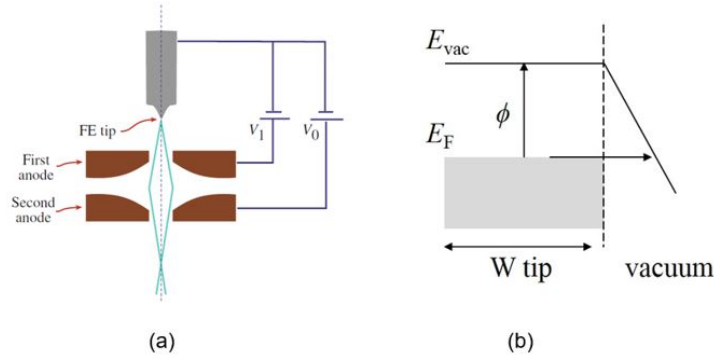


Figure 2.2: (a) Schematic of a field-emission source formed by two anodes and (b) the energy level diagram showing the process of field emission through tunneling ( $E_{vac}$  is the vacuum energy level, while  $E_F$  and  $\phi$  are the Fermi level and work function for the tungsten tip). The gradient of  $E_{vac}$  is proportional to the electric field at the tip (Williams and Carter, 2009).

The electrons emitted from the source can be made to illuminate a fixed area of the sample either as a parallel or focused beam. If the specimen is thin enough such that the incident electrons are transmitted through the sample, the technique is known as transmission electron microscopy (TEM). Scanning transmission electron microscopy (STEM) also uses an electron transparent specimen, but the illumination is a focussed beam that can be rastered across the specimen surface, such that the signal of interest is collected at each point.

### 2.1.1 Transmission Electron Microscopy (TEM)

The illumination system in an electron microscope comprises of the electron gun and the condenser lenses. In the TEM the illumination at the specimen will typically be a parallel beam with dimension of several micrometers. Two (electromagnetic) condenser lenses, C1 and C2 (see Figure 2.3), are used for controlling the illumination at the specimen. The C1 lens first forms an image of the gun crossover and the C2 lens is out of focus to produce an almost parallel beam. When

operating the C2 lens out of focus, the lens will be either strongly excited and the crossover occurs before the sample or weakly excited and the crossover occurs after the sample. This is known as over-focused and under-focused respectively. However, over-focus gives a less parallel beam at the specimen than under-focus, so that the latter is typically used during operation. In TEM the incoming electrons

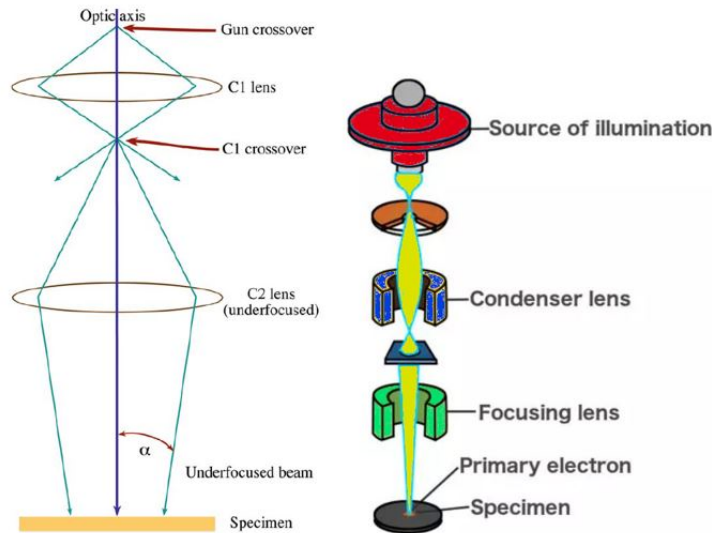


Figure 2.3: Parallel-beam operation in the TEM.

are scattered by both the electrons and the nuclei in the thin specimen. Therefore, there is an objective lens which serves much the same function as in a light microscope. The objective lens uses all the rays emanating from a point in an object and focuses it to a conjugate point in the image plane to form a real space image of the specimen. It also focuses parallel rays to a single point in the back focal plane to give a diffraction pattern (Figure 2.4). We therefore have both real and reciprocal space information from the same area of the specimen. There is also an objective aperture that can be inserted in the back focal plane in order to enhance specimen contrast (section 2.2). Note that both the image and diffraction pattern can be magnified using a series of projector lenses positioned below the sample.

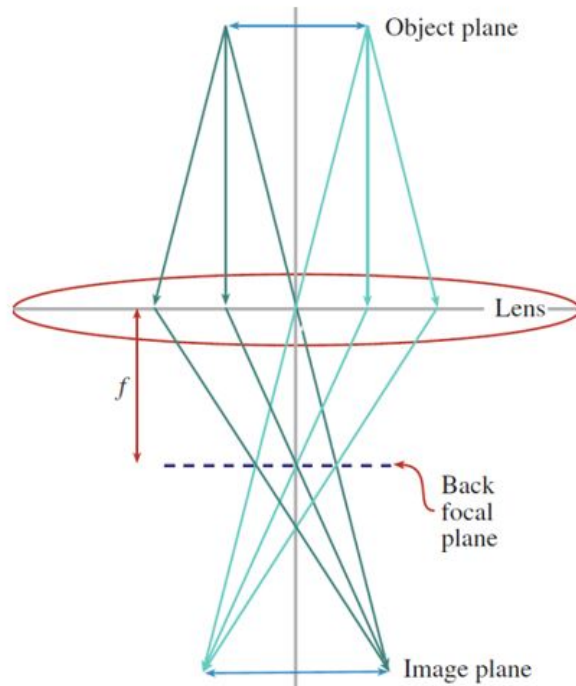


Figure 2.4: Ray diagram for a finite object as imaged by an objective lens. It shows the formation of a diffraction pattern in the back focal plane and real space image of the sample in the image plane (Williams and Carter, 2009).

## 2.1.2 Scanning Transmission Electron Microscopy (STEM)

A scanning transmission electron microscope (STEM) has additional scanning coils, detectors, and necessary circuitry to enable rastering of a focused probe across a specimen while collecting the signal of interest at each point. Most TEM microscopes enable switching between conventional transmission electron microscopy (CTEM) and STEM mode. These are known as TEM/STEM microscopes to distinguish it from dedicated STEMs (DSTEM) that operate only in STEM mode. Figure 2.5 shows that STEM mode in a TEM/STEM is achieved by the pre-field of the objective lens, so that the beam is focused to a small spot on the sample. For simplicity, the objective lens pre-field is denoted as a third condenser lens C3. The C3 lens in a TEM/STEM therefore performs a similar operation to the objective lens in a DSTEM.

TEM and STEM are related by what is called the principle of reciprocity, which

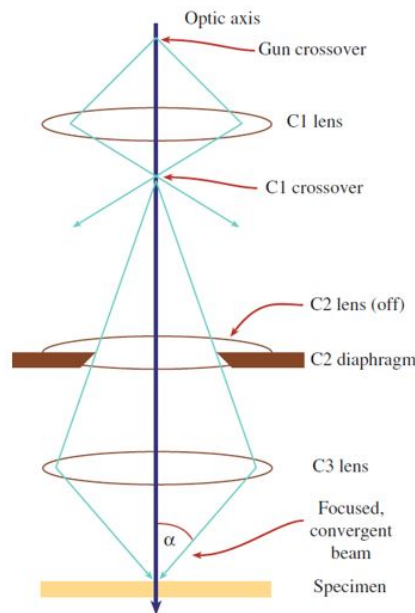


Figure 2.5: Convergent beam STEM mode operation in a TEM/STEM microscope (Williams and Carter, 2009).

states that the direction of the electron ‘rays’ from source to detector can be reversed. This is illustrated in Figure 2.6, which shows ray diagrams for TEM and STEM modes (the electron source for STEM is inverted to emphasise the symmetry). For simplicity imaging of only one point in the specimen is shown. The two optical arrangements are seen to be equivalent. The TEM post-specimen scattering angle  $2\alpha$  imposed by the objective aperture is equivalent to the pre-specimen STEM probe convergence angle. Similarly, the TEM pre-specimen illumination convergence angle  $2\beta$  from the C2 lens aperture is equivalent to the STEM post-specimen on-axis detector collection angle.

The electron optics in STEM is designed to produce an atomic or nanometer - size beam of electrons that illuminates a small area on the surface of the specimen. Images are formed by rastering the probe over the surface and collecting electrons that were transmitted through the sample (Bogner et al., 2007). The STEM probe size is governed by the effects of diffraction and spherical aberration. Spherical aberration is caused by the lens field acting inhomogeneously on the off-axis rays (Tanaka, 2008; Rose, 1990). Rays that are at an angle to the optic axis are more

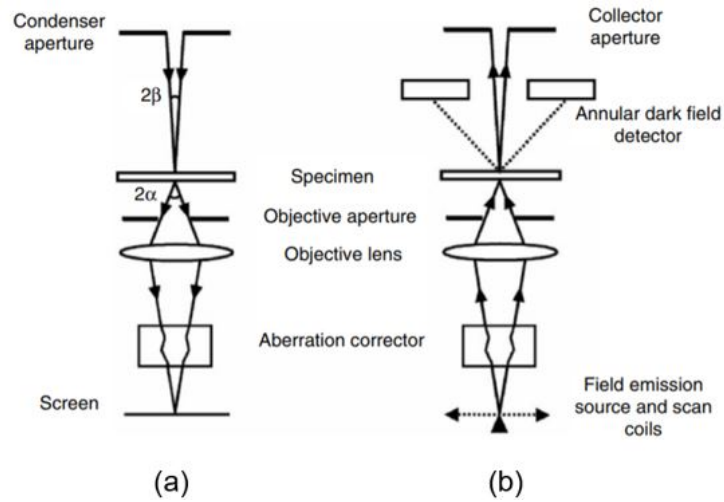


Figure 2.6: Ray diagrams show the reciprocity between a) TEM and b) STEM (Zhou and Wang, 2007).

strongly bent back toward the axis, resulting in a broader probe (Figure 2.7).

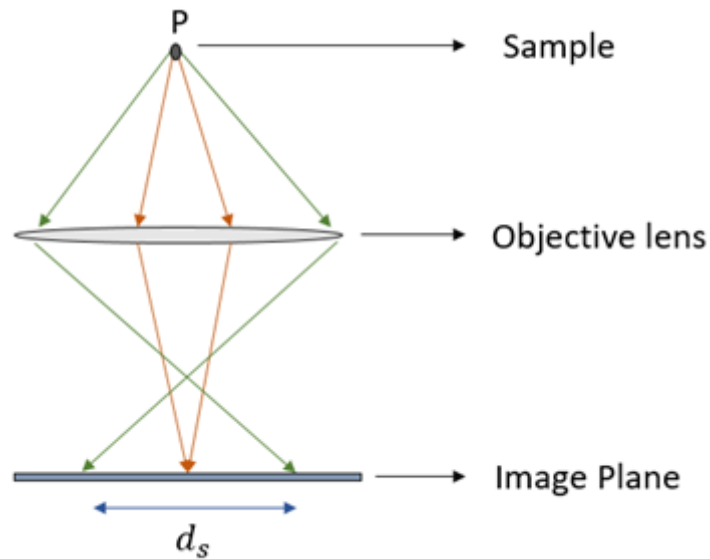


Figure 2.7: Ray diagram showing the effects of spherical aberration. Higher angle rays are focussed more strongly by the lens causing blurring of a point object ‘P’.

Spherical aberration is important because we need a large convergence angle to increase the current within the probe. The diameter of a spherical aberrated probe is given by:

$$d_s = \frac{1}{2} C_s \alpha^3 \quad (2.2)$$

where  $C_s$  is the spherical aberration coefficient and  $\alpha$  is the beam convergence semi-angle.

Diffraction aberration is simply the aberration we get due to spreading of the wave field from a narrow aperture (Figure 2.8). The diameter of the diffraction aberrated probe is given by:

$$d_d = \frac{1.22\lambda}{\sin \alpha} \approx \frac{1.22\lambda}{\alpha} \quad (2.3)$$

where  $\lambda$  is the wavelength of the electron beam. Equation 2.3 makes use of the small angle approximation  $\sin \alpha \approx \alpha$  for small  $\alpha$ .

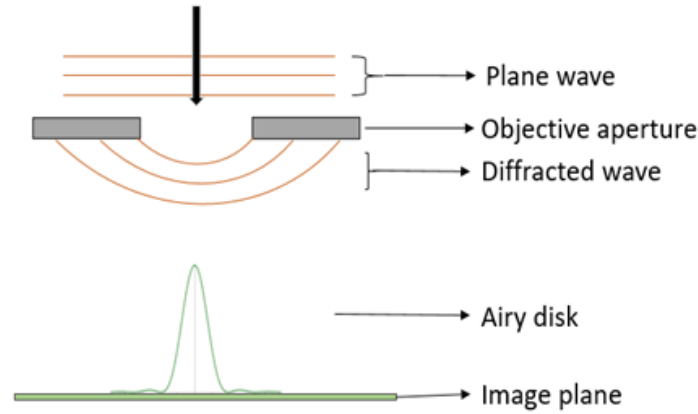


Figure 2.8: Schematic of a diffraction aberrated probe.

There are two competing effects determining the STEM probe size. Spherical aberration increases with convergence semi-angle  $\alpha$ , while diffraction aberration decreases with  $\alpha$ . This means that there is an optimum probe convergence semi-angle  $\alpha_{opt}$ . In the limit of infinite source demagnification the overall probe size ( $d_{net}$ ) (Voyles and Muller, 2002) due to diffraction and spherical aberration effects is given by the equation below:

$$d_{net}^2 = d_s^2 + d_d^2 \quad (2.4)$$

Figure 2.9 shows the variation of spherical and diffraction limited probe sizes as a function of  $\alpha$ . When  $\alpha$  is below the optimum angle, the dominant aberration

is diffraction. For  $\alpha$  larger than the optimum angle the dominant aberration is spherical aberration. The overall resolution in equation 2.4 shows a minimum at the optimum angle  $\alpha_{opt}$ .

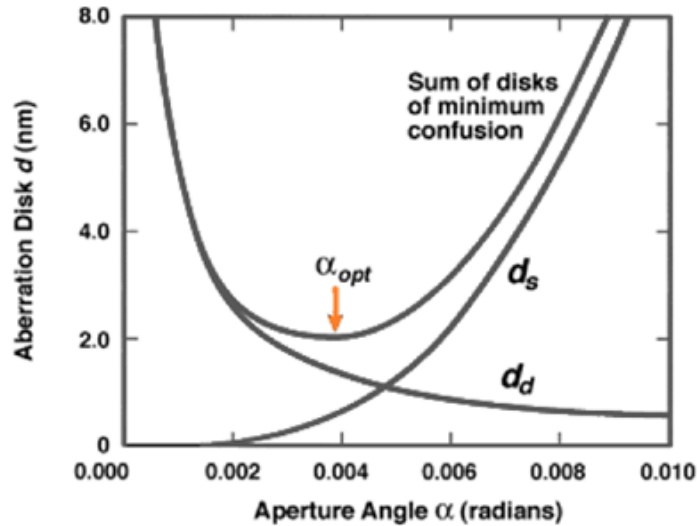


Figure 2.9: Curve of the diffraction and spherical aberration limited probe sizes

## 2.2 Bright and Dark field imaging

The contrast in a TEM image is due to the interaction of the electrons with the sample, while the beam penetrates through the specimen. Bright field (BF) and dark field (DF) imaging are two of the most basic types of images that can be acquired in a TEM. This is done by selecting a sub-region in the diffraction plane using an objective aperture. In BF the unscattered (transmitted) electron beam is selected with the objective aperture, and the scattered electrons are blocked; Figure 2.10(a). Since the unscattered beam is selected, areas with higher mass-thickness or which are crystalline and diffracting will appear dark in the image. In DF the unscattered electron beam is blocked by the aperture and the scattered electrons are selected; Figure 2.10(b). Regions with higher mass-thickness therefore appear brighter due to the larger scattering. Similarly, regions of crystalline material which strongly diffract along the direction selected by the aperture will also appear

brighter in the DF image.

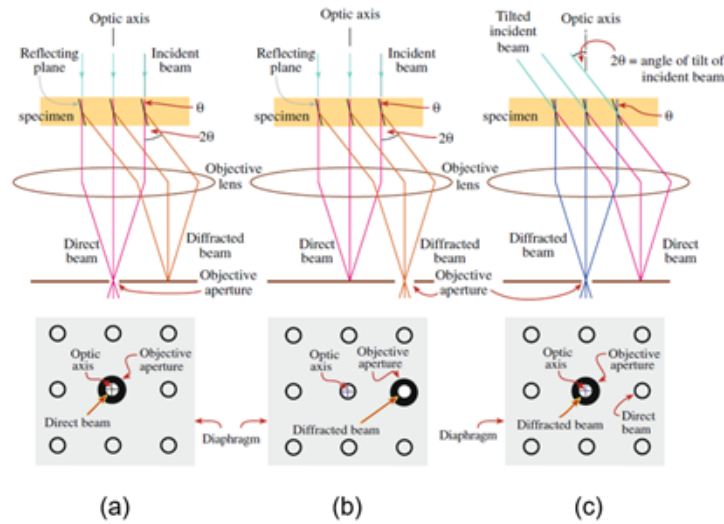


Figure 2.10: Ray diagrams showing how an objective aperture is used to produce (a) a bright field (BF) image formed from the on-axis, transmitted electron beam, (b) a dark field (DF) image formed with a specific off-axis scattered beam, and (c) a centered dark field (CDF) image where the incident beam is tilted to let the scattered beam pass along the optic axis (Williams and Carter, 1978).

In Figure 2.10(b), the electrons that are selected by the aperture for DF imaging travel off the optic axis. Therefore, when the aperture is displaced to select the scattered electrons, the off-axis electrons will undergo more distortion due to the higher spherical aberration, leading to a poor quality image (the blurring due to spherical aberration is proportional to the cube of the ray angle with respect to the optic axis). For solving this problem, there is an alternative method, called centered dark-field (CDF) imaging, Figure 2.10(c), where the scattered electrons are brought back on to the optic axis by tilting the incident beam and forming a DF image. The incident beam can be tilted using the beam shift-tilt coils in the microscope located above the specimen. Since the scattered beam is now parallel to the optic axis the distortion caused by spherical aberration is avoided. The resolution of CDF images is therefore similar to BF.

In STEM there are two detectors called bright field (BF) and annular dark field (ADF) detectors (Oxley et al., 2016), shown in Figure 2.8. In Figure 2.11, BF detector is located in the path of the transmitted electron beam to form a BF image,

while the ADF detector is located outside the path of the directly transmitted beam to detect only the scattered electrons and create an ADF image. The annular detector can collect all the electrons that are scattered at an angle from the optic axis. Furthermore, with the aid of post-specimen electron optics the collection angle of the ADF detector can be varied. This is done by changing the ‘camera length’ (effectively the magnification of the specimen diffraction pattern). ADF does not need an aperture to differentiate the scattered electrons from the main beam, unlike DF in CTEM. If we compare STEM with TEM, the image formation mechanism for BF in STEM is similar to TEM with a small point source and a large objective aperture collecting the transmitted and any other scattered beams (Figure 2.6). Therefore the main difference is between DF TEM and ADF STEM images. From Figure 2.6 it is clear that STEM ADF imaging is equivalent to hollow cone illumination in the TEM, i.e. instead of a parallel beam the illumination source consists of rays travelling at an angle to the optic axis with non-zero inner and outer angles  $2\beta$  (Figure 2.6).

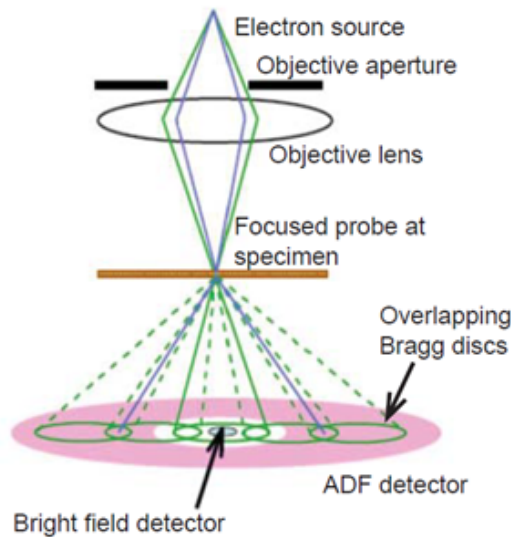


Figure 2.11: Schematic of image formation in a STEM, showing the on-axis small bright-field detector and an annular dark-field detector (pink) (MacArthur, 2016).

## 2.3 Phase contrast and high resolution electron microscopy (HREM)

In a crystal, atoms are ordered in a periodic pattern, while for amorphous specimens the atoms are randomly distributed. Figure 2.12 shows the wave profile for an electron moving through vacuum and through an individual atom. The atom has a low potential energy, so that the electron kinetic energy will be higher, and hence the wavelength shorter, because the total energy is conserved (Figure 2.12a). In comparison in Figure 2.12b, the wavelength in vacuum is unchanged.

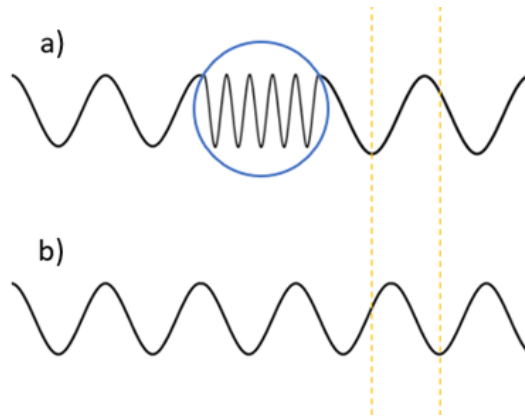


Figure 2.12: Electron wave profile a) within an atom and b) in vacuum. The vertical dashed lines represents the phase shift between the two electron wavefronts.

Therefore, comparing Figures 2.12a and 2.12b, there will be a phase shift between electrons travelling through vacuum and through the atomic potential. The atom therefore imprints a phase shift on the electron, which gives rise to phase contrast in an image due to interference. However, for a solid consisting of many atoms, net interference is only produced when the atoms are periodically arranged as in a diffraction grating, i.e. the solid must be a crystal that is aligned along a crystallographic direction with respect to the electron beam. The interference can be understood in terms of Bragg diffraction. Thus an incident electron beam in a crystal is diffracted into multiple beams that interfere constructively and destructively with each other, producing a pattern of bright and dark fringes. Phase contrast is

a technique that uses changes in the phase of electrons passing through a sample to create an image. The phase shift is caused by the interaction of the electron wave with the electrostatic potential of the atoms within the sample. The weak phase object approximation (WPOA) is a commonly used approximation in phase contrast imaging, where the phase shift introduced by the specimen is small compared to the unscattered wave passing through it (meaning that the scattering is very weak). The resulting image appears as a dark object against a bright background. Phase contrast imaging is often thought to be synonymous with high-resolution electron microscopy (HREM). HREM can be used in organic thin-films to visualise crystals in an otherwise disordered material, as shown in Figure 2.13 for pentacene. The crystal gives periodic bright and dark interference lines, although there is no contrast in the amorphous region, due to the atoms being disordered. The HREM signal is dominated by the amorphous background, and therefore the contrast of the crystalline region is low. For this reason, HREM is not often used to study ordering in ‘amorphous’ organic thin-films. Instead dark-field (DF) methods are employed (section 2.5, since here the background signal is low, which results in high contrast for any crystalline regions).

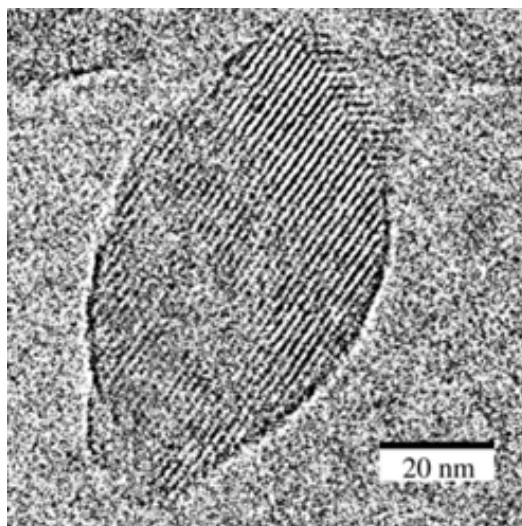


Figure 2.13: HREM image of a pentacene nanocrystal showing bright and dark fringes of a crystal surrounded by amorphous regions (Martin et al. (2005)).

## 2.4 Electron diffraction and pair correlation function

Electron diffraction is due to the wave nature of electrons (section 2.1). The diffraction of electron beams is in principle the same as for the diffraction of X-rays. Moreover, electrons are scattered by the strong electrostatic potential produced by the positive nucleus and the outer electrons of the atom (Lu and Hu, 2008). In TEM the electron diffraction pattern is formed in the back focal plane of the objective lens (Figure 2.4). The diffraction pattern in amorphous materials are different compared to crystalline materials. The latter consists of sharp diffraction spots (Bragg reflections) due to the periodic nature of the specimen. In amorphous materials there is no long range structure and therefore the sharp spots are broadened out into diffuse ‘halos’ (Figure 2.14 30). The diffraction pattern intensity for an amorphous specimen is governed by the pair correlation function  $g_2$ , or equivalently radial distribution function (section 1.4), as demonstrated below.

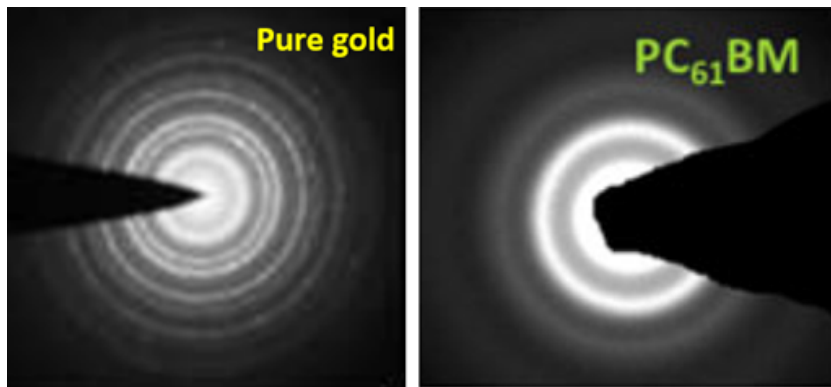


Figure 2.14: Two electron diffraction patterns showing sharp rings in polycrystalline pure gold and broad ‘halos’ in amorphous PC61BM.

The scattered amplitude from an amorphous material is described by,

$$S(\Delta k) = \sum_m f_m \exp(-i\Delta k \cdot r_m) \quad (2.5)$$

where  $f_m$  is the atom scattering factor for the atom at position vector  $r_m$  and  $\Delta k$  is the scattering vector. The summation is over all atoms in the solid. Multiplying by the complex conjugate ( $S^*$ ) we obtain the scattered intensity:

$$I(K, \alpha) = S^* S = \sum_m \sum_n f_m f_n \exp[i\Delta k \cdot (r_m - r_n)] \quad (2.6)$$

If  $\alpha$  denotes the angle between  $\Delta k$  and  $(r_m - r_n)$ , where  $r_n$  is the position of the  $n^{\text{th}}$  atom, equation 2.6 will be:

$$I(K, \alpha) = \sum_m \sum_n f_m f_n \exp(ikr_{mn} \cos \alpha) \quad (2.7)$$

where  $K$  and  $r_{mn}$  are the magnitudes of  $\Delta k$  and  $(r_m - r_n)$  respectively. When the specimen is amorphous, the vector  $(r_m - r_n)$  only depends on the magnitude  $r_{mn}$  and not on the angle  $\alpha$ , since there is no directionality. Exploiting the isotropic nature of the solid we can calculate the average phase factor over a sphere as (McEuen and Kittel, 2005):

$$\langle \exp(ikr_{mn} \cos \alpha) \rangle = \frac{\sin Kr_{mn}}{Kr_{mn}} \quad (2.8)$$

The scattered intensity will then be:

$$I(K) = \sum_m \sum_n f_m f_n \frac{\sin Kr_{mn}}{Kr_{mn}} \quad (2.9)$$

Where there is only one atom type (i.e. monoatomic) in the amorphous material the scattering factors will be identical ( $f_m = f_n = f$ ) and so the intensity for  $N$  atoms in the specimen will give,

$$I(K) = Nf^2 \left[ 1 + \sum_{m \neq n} \frac{\sin Kr_{mn}}{Kr_{mn}} \right] \quad (2.10)$$

where the 1 comes from the fact that when we have  $n=m$  the value of  $r_{mn}$  is zero so that  $[\sin(Kr_{mn})/(Kr_{mn})] = 1$

The discrete summation in Equation (2.10) can be converted to an integral, and written as,

$$I(K) = Nf^2 \left[ 1 + \int_0^R dr 4\pi r^2 \rho(r) \frac{\sin Kr_{mn}}{Kr_{mn}} \right] \quad (2.11)$$

where  $\rho(r)$  represents the concentration of atoms at distance  $r$  and  $4\pi r^2$  represents the area of the sphere. The upper limit  $R$  represents the boundary of the solid.

Making use of the relation  $\rho(r) = g_2(r)\rho_o$ , where  $\rho_o$  is the average atomic concentration, it can be shown that (McEuen and Kittel, 2005):

$$g_2(r) = 1 + \frac{1}{2\pi r^2 \rho_o} \int \left[ \frac{I(K) - Nf^2}{Nf^2} \right] K(\sin Kr) dK \quad (2.12)$$

This result shows that by measuring the diffraction intensity it is possible to extract the radial distribution function  $g_2(r)$  by performing the Fourier transform in Equation (2.12). This method has been used to extract  $g_2(r)$  in organic materials such as P3HT and PCBM (McEuen and Kittel, 2005). Mu et al (Mu et al., 2019) have shown that electron diffraction based RDF analysis can be used to characterise polymers films such as P3HT and small molecules like PC<sub>61</sub>BM as well as bulk heterojunction materials consisting of P3HT:PC<sub>61</sub>BM blends (Figure 2.15). The experimental RDF of the P3HT, PC<sub>61</sub>BM neat films agree closely with simulation, and the RDF of the P3HT:PC<sub>61</sub>BM blend is found to follow a rule of mixtures depending on the relative concentration of P3HT and PC<sub>61</sub>BM.

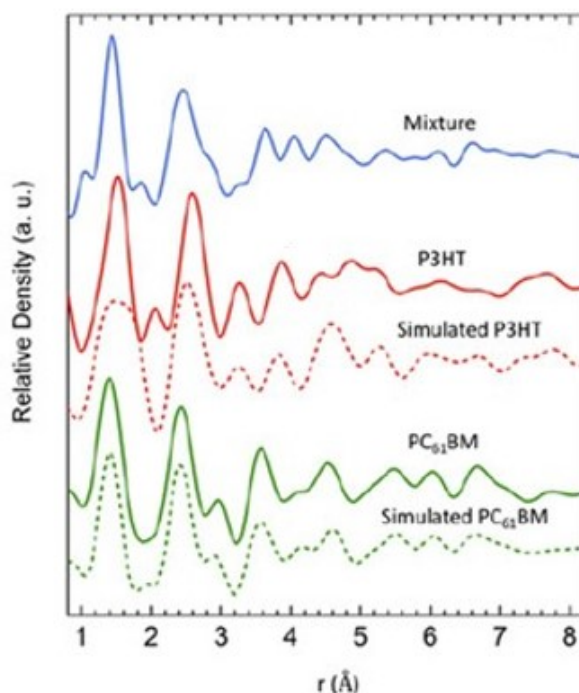


Figure 2.15: Experimental RDFs (from top to bottom) of a P3HT:PC<sub>61</sub>BM blend (blue solid line), neat P3HT (red solid line) with simulated RDF (red dashed line) and neat PC<sub>61</sub>BM (green solid line) with simulated PDF (green dashed line) (Mu et al., 2019).

## 2.5 Electron microscopy techniques for probing order

For amorphous polymer and small molecules the diffraction pattern contains diffuse rings, from which the radial distribution function ( $g_2$ ) can be directly determined. As described in section 1.4 the radial distribution function only contains information on the short range ordering in amorphous solids. However, for probing medium range order  $g_2(r)$  will be not be of much use and therefore high order correlation functions, such as  $g_3$  and  $g_4$ , are required. Information on these higher order correlation functions can be obtained using the technique of fluctuation electron microscopy (FEM) which is described in the following sections.

### 2.5.1 Fluctuation Electron Microscopy in the TEM

Fluctuation electron microscopy (FEM) is a technique that probes nanometer scale medium range order (MRO) in amorphous materials (Lee et al., 2010). Treacy and Gibson were the first to use FEM to examine MRO in vacuum-deposited amorphous germanium in 1996 (Gibson and Treacy, 1997) and later they examined amorphous silicon (Voyles et al., 2001a). This involves acquiring a series of centred dark field (CDF) images and calculating the intensity variance in the images. There are two types of FEM techniques depending on how the dark field images are acquired (Voyles and Abelson, 2003; Treacy et al., 1998). The first type is called variable coherence FEM, which involves acquiring a series of CDF images at different beam tilts (or equivalently different scattering vector magnitude  $k$ ) while keeping the image resolution constant (i.e. fixed objective aperture size) (Gibson and Treacy, 1997). The second type is called variable resolution FEM (Hilke et al., 2019). It involves acquiring a series of CDF images at constant  $k$  by changing the objective aperture size, so that the Airy disk size and hence resolution  $Q$  is different between the images. However, this method is more difficult to implement since there are only a limited number of objective aperture sizes in most microscopes (four for a standard JEOL 2100F FEG TEM used in this work). The CDF image intensity

variance in FEM is a function of the scattering vector magnitude  $k$  as well as the image resolution  $Q$ . The intensity variance ( $V$ ) is defined as:

$$V(k, Q) = \frac{\langle I(k, Q)^2 \rangle}{\langle I(k, Q) \rangle^2} - 1 \quad (2.13)$$

where  $\langle I(k, Q) \rangle^2$  is the mean square intensity and  $\langle I(k, Q)^2 \rangle$  is the square mean intensity calculated over the entire CDF image. The variance can be shown to be dependent on the MRO pair correlation functions  $g_3$  and  $g_4$  (Zhang et al., 2018; Voyles et al., 2000). This dependence is due to the  $\langle I(k, Q)^2 \rangle$  term in the numerator of Equation (2.13); taking the square of Equation (2.6) we obtain:

$$I(K)^2 = \sum_{(m,n)} \sum_{(p,q)} f_m f_n f_p f_q \exp[(i\Delta k \cdot (r_{mn} + r_{pq}))] \quad (2.14)$$

where  $r_{mn} = (r_m - r_n)$  is the separation between the atom pair  $(n, m)$  and similarly for  $r_{pq}$ . It is clear that the square intensity  $I(K)^2$  depends on interference between scattering from different atom pairs, unlike the intensity  $I(K)$  which only depends on interference between atoms in a single pair (Equation 2.6). Therefore  $\langle I(k, Q)^2 \rangle$  is dependent on  $g_3$  and  $g_4$  (as well as  $g_2$ ), while from the previous section the  $\langle I(k, Q) \rangle$  term in the denominator of Equation 2.13 is dependent only on  $g_2$ . Complete expressions for the variance  $V(k, Q)$  can be found in (Voyles and Abelson, 2003; Voyles et al., 2000; Treacy et al., 2005). In a FEM experiment  $V(k, Q)$  is plotted as a function of  $k$  keeping  $Q$  constant (variable coherence FEM) or as a function of  $Q$  keeping  $k$  constant (variable resolution FEM). As mentioned previously the former is easier to implement due to practical reasons.

As an example of a variable coherence FEM measurement Figure 2.16(a) shows a variance plot (i.e. intensity variance of CDF image as a function of scattering vector magnitude  $k$ ) for amorphous silicon (Voyles and Abelson, 2003). The figure inset shows example CDF images at different  $k$ , where the so-called ‘speckle’ pattern, consisting of bright regions against a dark background is apparent. Speckle is the interference pattern from random sources. There are two type of speckle; shot noise which is associated with the illumination and not with the specimen, while the

other type is interference related to Bragg diffraction in the specimen. The latter contains important information about the sample. At  $k$ -values where the intensity variance is maximum the speckle contrast is large, while for  $k$ -values at minimum intensity variance the speckle pattern is less distinct. The intensity variance peaks at  $k$ -values corresponding to Bragg diffraction from individual lattice planes in the crystalline form of the sample. For example, the largest peak in Figure 2.16a is centred about the  $k$  scattering vector magnitude for the (111) plane in crystalline silicon. Since the sample is amorphous however the variance peak is not sharp but considerably broadened. The high intensity regions in the speckle pattern consists of small crystalline domains that are close to Bragg orientation in the otherwise amorphous specimen (Figure 2.16b). The scattering from atoms within the crystalline domain interfere constructively leading to a higher local intensity in the dark field image. On the other hand the regions around the crystalline domains are amorphous and therefore have lower dark field intensity.

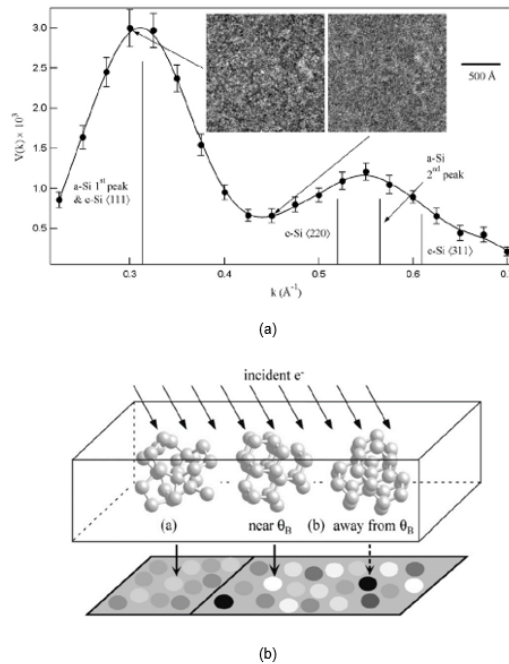


Figure 2.16: (a) Variance as function of scattering vector magnitude ( $k$ ) for an amorphous silicon sample. (b) The origin of the speckle pattern in a dark field image. Bragg scattering from small crystalline domains in an otherwise amorphous solid give rise to local variations in the dark field image intensity (Voyles and Abelson, 2003).

We can further explain the rationale behind fluctuation electron microscopy as a probe for  $g_3$  and  $g_4$  medium range order by introducing the concept of a coherence volume. Coherence volume is defined as the volume around each atomic scatterer where constructive interference with scattering from other atoms within the volume can take place, i.e. scattering from the atoms are ‘in-phase’. The coherence volume ( $F$ ) for an incident plane wave has the form  $F = \exp(2\pi i k \cdot r)$ , where  $k$  is the wave vector of the illumination and  $r$  is a position vector within the sample (Voyle and Muller, 2002). In FEM-TEM, a technique called hollow-cone illumination is also used to control the coherence volume (Treacy and Gibson, 1993). The idea of this technique is to tilt the illumination by a fixed angle before precessing electronically about the optic axis. The illumination therefore maintains the same tilt angle while the azimuthal angle is varied. The coherence volume for hollow cone illumination is smaller than that for a plane wave; it has an elongated ‘cigar’ shape, as shown in Figure 2.17 (Treacy and Gibson, 1993). The size of the coherence volume is a function of the inner and outer angles of the hollow cone illumination. For a fixed outer angle the coherence volume size decreases with increasing inner angle (Figure 2.17).

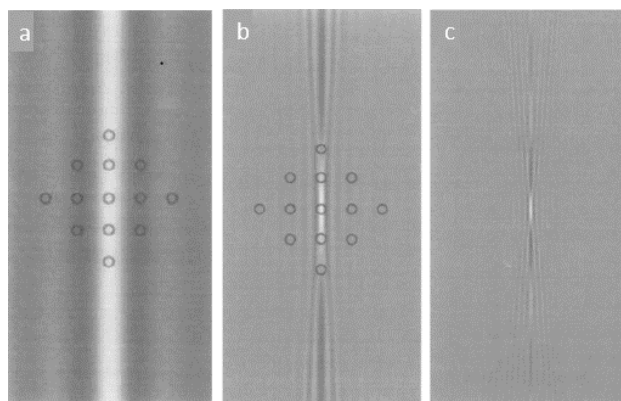


Figure 2.17: Coherence volume for 100 kV hollow cone illumination superimposed on the atomic positions (open circles) within a silicon specimen viewed in the [100] direction. In these images grey represents regions where no interference with the central atom can take place during scattering. Bright and dark regions represent regions of constructive and destructive interference respectively. The outer angle of the hollow cone illumination is fixed at 200 mrad, while the inner angle in (a), (b) and (c) are 10, 50 and 100 mrad respectively (Treacy and Gibson, 1993).

Consider now scattering from atoms within the specimen; for simplicity we only consider two atom pairs. Figure 2.18a shows a situation where both atom pairs are within the same coherence volume. Here scattering from the two atom pairs can interfere constructively with one another. In Figure 2.18b the two atom pairs are shown displaced from one another, such that they do not lie within the same coherence volume but lie within the same Airy disc. The Airy disc represents the blurring in image intensity caused by lens aberrations. If there are no aberrations each point in the specimen is imaged faithfully. However, in the presence of lens aberrations the intensity from a given specimen point will be ‘smeared’ over a distance determined by the Airy disc size. Therefore, although the scattering from the two atom pairs in Figure 2.18b cannot directly interfere with one another (since they are not in the same coherence volume), their intensities will overlap in the final image. The image intensity variance therefore depends on the distribution of atom pairs within the specimen as well as the Airy disc size. If the Airy disc size is varied (e.g. by changing the objective aperture size) intensities from different atom pairs can contribute to the final image; this is the principle behind variable resolution FEM and its use as a probe for medium range order. Alternatively, the coherence volume could also be varied by changing the illumination conditions (e.g. inner angle of hollow cone illumination) such that scattering from the two atom pairs can now interfere with one another (Figure 2.18c). This is the principle behind variable coherence FEM.

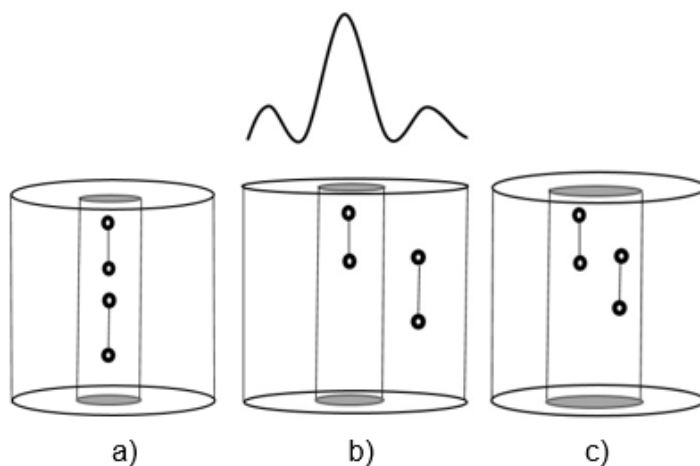


Figure 2.18: The role of coherence volume (smaller shaded cylinder) and Airy disc (larger open cylinder) on scattering from two atom pairs. (a) shows the two atom pairs within the same coherence volume and Airy disc, while in (b) the two atom pairs are within the same Airy disc but different coherence volumes (the curve on the top represents the Airy disc profile). (c) is the same as (b) but with a larger coherence volume. See text for further details.

## 2.5.2 Fluctuation Electron Microscopy in the STEM

In TEM the technique to change the coherence volume is by varying the illumination (i.e. scattering vector magnitude  $k$  of tilted beam). In STEM it is by varying the inner angle of the annular dark-field detector (Cowley, 2001). For variable resolution in TEM, we are using the objective aperture size in the diffraction plane to change the image resolution, while in STEM the same effect is achieved with the probe convergence angle. STEM is an alternative, but essentially equivalent method of carrying out FEM because of the reciprocity principle (Liu, 2005) (see Figure 2.6). In STEM the beam is rastered over the specimen area and at each raster point a diffraction pattern is acquired (Figure 2.19). The speckle statistics in the diffraction patterns are analysed to give a variance plot similar to Figure 2.16a. STEM offers a denser scattering vector sampling at a reduced sample dose (due to all scattering vectors being recorded simultaneously) and captures more of the diffracted intensity. STEM FEM is therefore better suited to organic materials which are prone to damage under the electron beam.

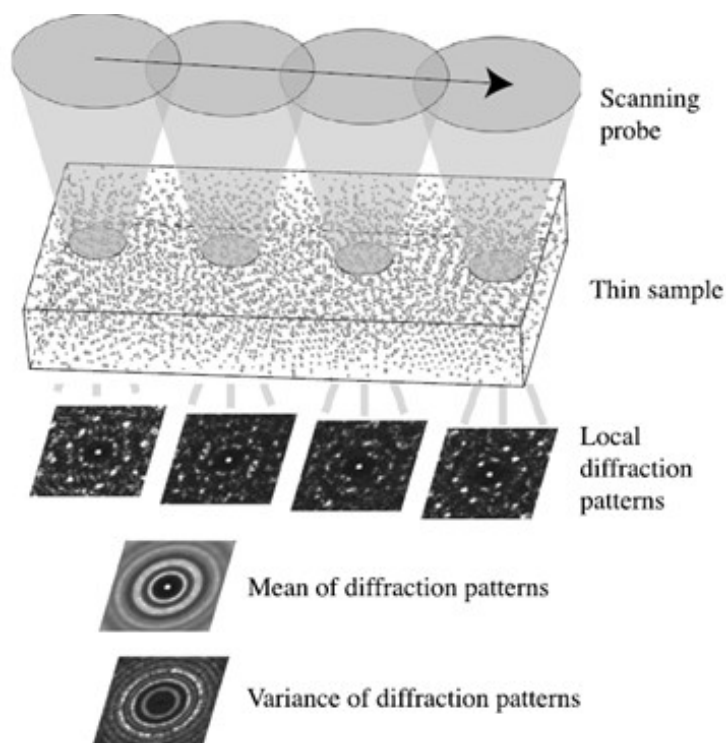


Figure 2.19: Schematic illustrating STEM fluctuation electron microscopy measurements. The specimen is probed by scanning the electron beam over the sample and collecting a diffraction pattern at each point (Treacy et al., 2005).

In TEM it is difficult to extract variance curves similar to Figure 2.16a for organic materials because of the large unit cell size. This means that many of the  $k$ -values for Bragg diffraction from crystal planes are small, meaning that a small objective aperture size must be used to improve the resolution in  $k$ . As an example for P3HT the error bar in  $k$  for the smallest objective aperture (5.3 mrad) on our microscope is still too large. There are two solutions to overcoming this problem. The first is to carry out FEM measurement in STEM. Since the entire diffraction pattern is collected at each point, a ‘virtual’ annular detector (by reciprocity equivalent to a TEM objective aperture) of appropriate size can be created in the computer. This however requires the ability to perform 4D-STEM measurements, i.e. at each point in the 2D specimen plane a 2D diffraction pattern must be acquired to give a 4D data set.

An alternative method is to acquire FEM dark-field images over not one but a range

of scattering  $k$ -vectors. This is most easily achieved using the annular dark-field (ADF) detector in STEM geometry (Figure 2.11) (Cowley, 2002). By changing the inner angle of the ADF detector (through control of the STEM camera length) the coherence volume can be varied (see Figure 2.17). A small inner angle gives low and high angle scattering and large coherence volume, while a large inner angle gives only higher angle scattering and small coherence volume. In this method STEM ADF images at different inner angles (i.e. camera lengths) are acquired. From this data set the intensity variance can be plotted as a function of the detector inner angle. Due to the range of  $k$ -vectors measured by the ADF detector the variance plot will be different to Figure 2.16a. Figure 2.20 is a schematic of the expected variance plot. Large inner angles will not produce much interference (i.e. coherence volume is the size of a single atom) and therefore give an incoherent dark-field image with atomic number contrast. The variance is therefore almost zero for organic materials of constant atomic number. Small inner angles give larger coherence volumes and therefore higher ADF image intensity variance. The variance is therefore expected to increase as the inner angle is made smaller and coherence volume size increases. However, the intensity variance plateaus when the coherence volume is as large as the crystalline domain or STEM probe Airy disc (whichever is the smaller). Therefore, for a sufficiently broad probe, the plateau's onset is a measure of crystalline domain size, i.e. larger domains will have a smaller inner angle onset. Furthermore, the plateau intensity is a measure of the paracrystallinity within the domain, i.e. a crystalline domain with less strain will produce a higher plateau intensity. Here we define paracrystallinity as small amounts of disorder in an otherwise perfect crystalline material with long range order. This does not include the effect of finite size domains, as would be the case for a polycrystalline material. Therefore, the variance plot can provide us additional qualitative information on the paracrystallinity and size of ordered domains within the material.

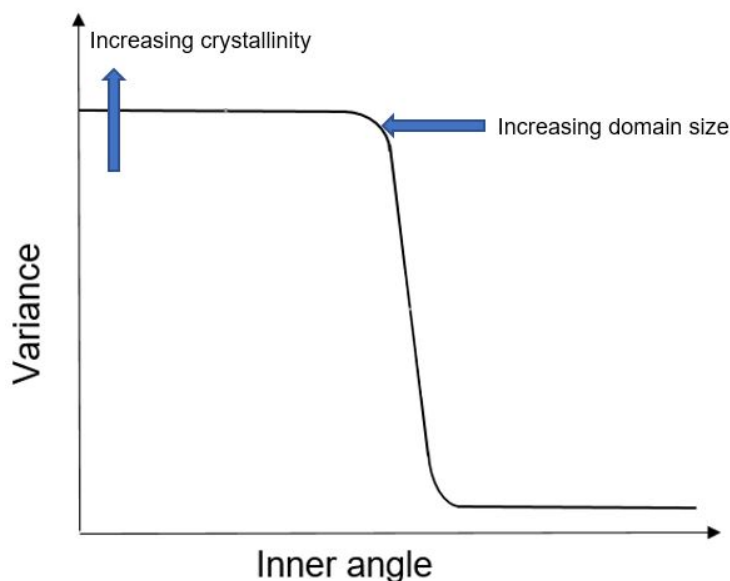


Figure 2.20: Plot of variance dependence on inner angle for an "amorphous" material as at large inner angle the curve drops to zero and shows no crystallinity. See text for further details.

### 2.5.3 Energy electron loss spectroscopy (EELS) analysis

In the previous section, we introduced TEM and STEM techniques and described how they yield valuable information about the internal structure of a specimen. Still, we did not discuss, for example, the chemical composition of the specimen or the orientation of the molecules. An analysis technique called electron energy loss spectroscopy (EELS) measures the energy lost by the primary electrons as they travel through a thin TEM specimen and has the ability to acquire structural and chemical information from a specimen, with a nanometer spatial resolution or the atomic level in favourable cases (Egerton, 2008). In this section it will be shown how the EELS signal can be used to determine the orientation of  $\pi$ -stacking in certain organic materials, such as P3HT (see Figure 1.11, section 1.3). In the case of P3HT this is useful for establishing if the lamellae lie face down or end-on to the substrate on which the thin-film is deposited. EELS instrumentation is based on a magnetic prism that uses a magnetic field to disperse the electrons transmitted through the sample according to their final energy (Egerton, 2008; Egerton and

Malac, 2005). The idea of a magnetic prism is similar to the action of a glass prism on a beam of white light, i.e. separation of the white light according to their energy or wavelength. The magnetic prism is bringing together and focusing the electrons of the same energy at the exit of the spectrometer (Egerton, 2008). In other words the magnetic prism separates the electrons into an EELS energy loss spectrum at the dispersion plane (Figure 2.21). In addition to spectra it is also possible to form energy filtered images or diffraction patterns of the various EELS signals by inserting an energy selecting slit at the dispersion plane. The information is recorded electronically by a charge-coupled device (CCD) camera as shown in Figure 2.21. The magnetic prism/energy filter is a highly sensitive device with an energy resolution  $< 1$  eV even with high acceleration voltage of the primary electrons. The energy-loss spectrum is arbitrarily split up into the low loss

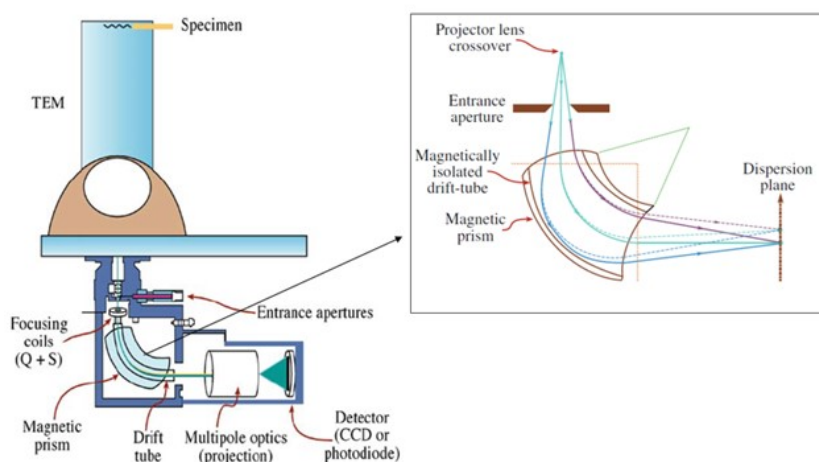


Figure 2.21: Schematic diagram that shows on the left hand side the electron energy-loss spectrometer mounted below the viewing screen of a TEM and at the right hand side shows the focussing lens action in the dispersion plane outside the spectrometer(Williams and Carter, 1978).

(maximum 50 eV) and high loss regions (Figure 2.22). The low energy-loss spectrum contains a zero-loss and plasmon peak. The zero-loss peak represent electrons that were scattered elastically or remained unscattered, as well as inelastic scattering events with energy loss below the energy resolution of the EELS spectrometer. This typically includes phonon scattering caused by the thermal vibration of atoms

within the sample, where the energy loss is of the order of meV. Plasmon scattering takes the form of a collective oscillation of the valence or outer-shell electrons in the specimen (Egerton, 2008). The plasmon energy is fixed by the natural oscillation frequency of the valence electrons (McEuen and Kittel, 2005). Figure 2.22 shows that with increasing energy loss above the plasmon peak, the overall signal intensity decreases rapidly. But, because of energy transfer to inner-shell or core electrons in the atom, there is an increase in EELS intensity (such as K-edge) at an energy loss equal to the inner shell ionisation energy, i.e. the core atomic electron gains sufficient energy to be promoted to a continuum energy level. Due to quantisation of electronic energy levels the ionisation energy is characteristic of a particular chemical element. Thus, the energy of ionisation edge, also known as core loss edges, indicates which elements are present within the specimen (Egerton et al., 2005).

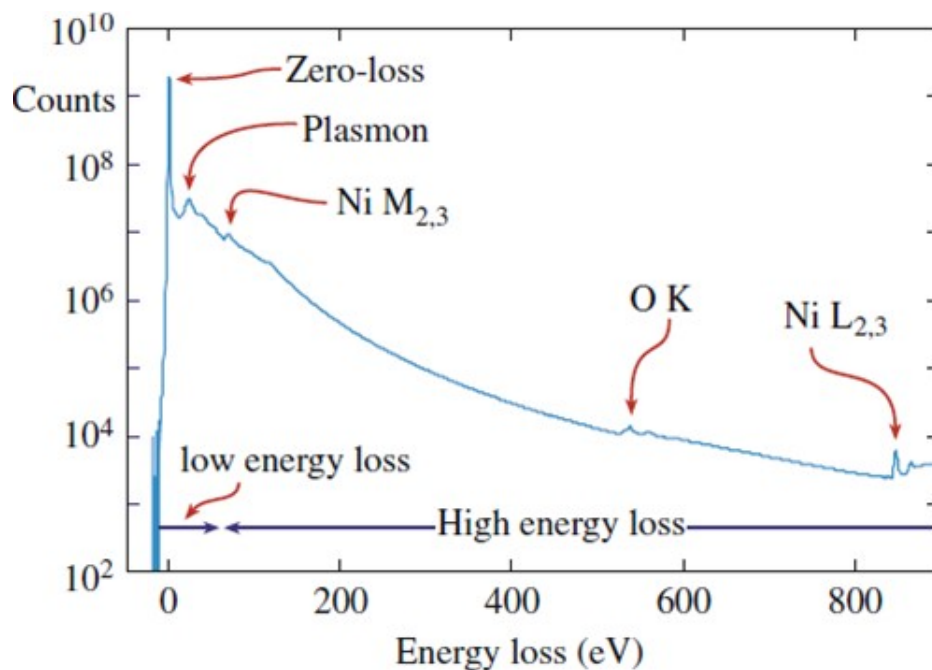


Figure 2.22: EELS spectrum plotted on a logarithmic intensity scale. The overall signal intensity drops rapidly with increasing energy loss above the plasmon peak. In most cases the zero-loss peak is several orders of magnitude more intense than the low energy-loss portion. At the high energy loss, the small ionisation edge peaks are shown (Williams and Carter, 1978).

Core loss edges typically have complex shapes due to so-called ‘fine structure’.

Figure 2.23 explains the origin of the fine structure. It shows intensity variations in the core-loss spectra called energy-loss near-edge structure (ELNES) and extended energy-loss fine structure (EXELFS). ELNES is the fine structure close to the edge onset, while EXELFS is present at higher energy losses. The reason for having a fine structure in an EELS edge shape is the unoccupied density of states (DOS) (Liao, 2006) shown at the top in figure 2.23. We can obtain data on the DOS because of the high-energy resolution inherent in EELS which makes the fine structure visible. There are two types of electronic states in a solid; filled and empty and they represent the occupied, and unoccupied states, respectively. Thus, we are taking an electron from one of the occupied states and exciting it into the unoccupied state. In the filled state, the DOS has a parabolic shape (for free-electron solid which is highly idealised). Above the Fermi energy empty (unoccupied) state DOS has oscillations in its shape due to bonding effects in the solid. ELNES and EXELFS arise because of the ionisation process that can impart more than the critical ionisation energy ( $\Delta E$ ). The fine structure in the core loss edge mirrors the oscillations in the unoccupied DOS. For example, a fine structure peak in the EELS edge is due to a local peak in the unoccupied DOS, and represents the fact that there are more empty states for the core electron to be promoted into. For ELNES, the oscillation is strong with energy about 30-50 eV above the critical energy while in EXELFS the oscillation becomes weaker as it extends out for several 100 eV (Williams and Carter, 1978). Thus, the EELS edge shape represents the (partial) unoccupied DOS and can be used as a probe of the bonding structure around the ionised atom. In our work we are interested in using the near-edge structure for the carbon K-edge in order to determine the orientation of the  $\pi$ -stacking in organic thin-films. Figure 2.24 shows the EELS carbon K-edge shapes for graphite ( $sp^2$  bonding) and diamond ( $sp^3$ ) respectively. The sharp peak ( $\pi^*$ ) at the absorption edge in graphite corresponds to the excitation of carbon K-shell electron (1s electron) to the  $\pi^*$  anti-bonding orbital involving  $p_z$  orbitals (see section 1.2.1). Similarly, the higher energy  $\sigma^*$  peak corresponds to excitation of the

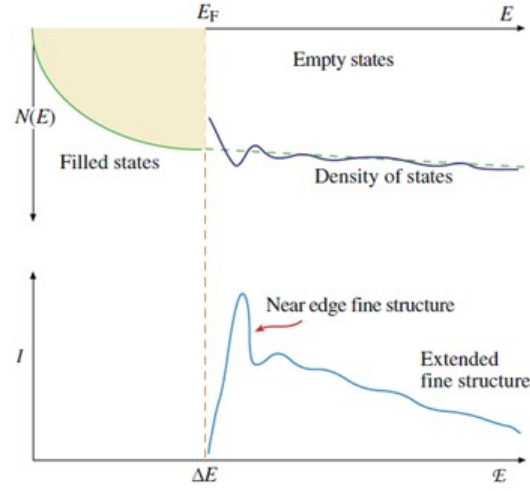


Figure 2.23: The diagram shows the relationship between the empty and filled electronic state DOS and the fine structure in EELS. A smooth curve is drawn for the DOS below the Fermi energy ( $E_F$ ) for filled states while an oscillating shape is present for the empty states. The corresponding EELS edge shape is shown at the bottom of the figure (Williams and Carter, 1978).

1s electron to  $\sigma^*$  anti-bonding orbitals. In diamond, there is only a broad  $\sigma^*$  peak and no  $\pi^*$  peak due to  $sp^3$  bonding. Amorphous carbon contains a mixture of  $sp^2$  and  $sp^3$  bonding and the structural variations can be estimated by comparing the relative proportions of  $\pi^*$  and  $\sigma^*$  peak intensity, following calibration with known standards. The carbon K-edge shows anisotropy effects, meaning that the relative intensity of  $\pi^*$  and  $\sigma^*$  features (figure 2.24) is sensitive to the orientation of the incident beam with respect to the sample. According to Fermi's golden rule the EELS (core loss) edge shape can be expressed as:

$$\frac{d^2\sigma_{if}(\theta)}{d\Omega dE} = \frac{4}{a_0^2 q^4} |\langle f | \exp(i\vec{q} \cdot \vec{r}) | i \rangle|^2 \quad (2.15)$$

where  $\sigma_{if}$  is the scattering cross-section,  $\vec{q}$  is the momentum transfer (related to scattering angle  $\theta$ ),  $a_0$  is the Bohr radius and  $\vec{r}$  is the position vector of the atomic electron undergoing transition from an initial state  $|i\rangle$  to final state  $|f\rangle$ . Equation 2.15 represents the double differential scattering cross-section per unit energy loss ( $E$ ) and per unit solid angle ( $\Omega$ ). The expression  $|\langle f | \exp(i\vec{q} \cdot \vec{r}) | i \rangle|^2$  determines the EELS edge shape and is called the transition matrix element. Moreover, fine structure in EELS can arise when an inner-shell electron in a state  $|i\rangle$  is promoted

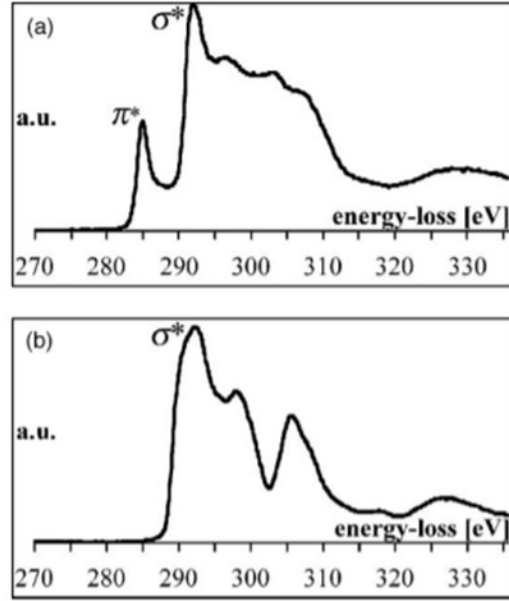


Figure 2.24: EELS spectrum of carbon K-edge for (a) graphite and (b) diamond (Hamon et al., 2004).

to an unoccupied state  $|f\rangle$  which has a non-monotonic density of states (Leapman et al., 1983); see Figure 2.23. In quantum mechanics, the transition matrix element can be represented by the integral:

$$\int \phi_f^* \exp(i\vec{q} \cdot \vec{r}) \phi_i d\vec{r} \quad (2.16)$$

where  $\phi_i$  and  $\phi_f$  are the initial and final state wavefunctions and the asterisk denotes the complex conjugate. The exponential in Equation 2.16 can be expanded as:

$$\exp(i\vec{q} \cdot \vec{r}) = 1 + i\vec{q} \cdot \vec{r} - \frac{1}{2}(i\vec{q} \cdot \vec{r})^2 + \dots \quad (2.17)$$

The first term in the expansion will give zero because the wave functions are orthogonal. For small  $\vec{q}$  (dipole limit), this means that to collect electrons within the dipole limit, the detector needs to be positioned in a way that restricts the collection angle to within the dipole limit, so we only retain the second term which gives:

$$i \int \phi_f^* (\vec{q} \cdot \vec{r}) \phi_i d\vec{r} \quad (2.18)$$

The above integral is zero when  $\vec{q}$  is perpendicular to the atomic electron position vector  $\vec{r}$ . Consider applying Equation 2.18 to the carbon K-edge in graphite [001].

The initial wavefunction  $\phi_i$  corresponds to the 1s state which is isotropic. However, this is not the case for the final wavefunction  $\phi_f$ , i.e. the  $\pi^*$  anti-bonding orbitals are perpendicular to the graphite planes, while the  $\sigma^*$  anti-bonding orbitals lie in-plane. Therefore, if  $\vec{q}$  is perpendicular to the anti-bonding orbital then the corresponding fine structure will not appear in the EELS spectrum. As an example, consider the case where the incident electrons are normal to the graphite planes. If the EELS collection angle  $\theta$  is small then  $\vec{q}$  will be in the same direction of the electron beam, and only the  $\pi^*$  peak will appear in the fine structure since  $\vec{q} \cdot \vec{r} = 0$  for the  $\sigma^*$  peak. For higher collection angles however the intensity of the  $\sigma^*$  peak will increase relative to  $\pi^*$ . This is demonstrated experimentally in Figure 2.25. In our experiment, the incident beam is fixed with respect to the organic thin-film

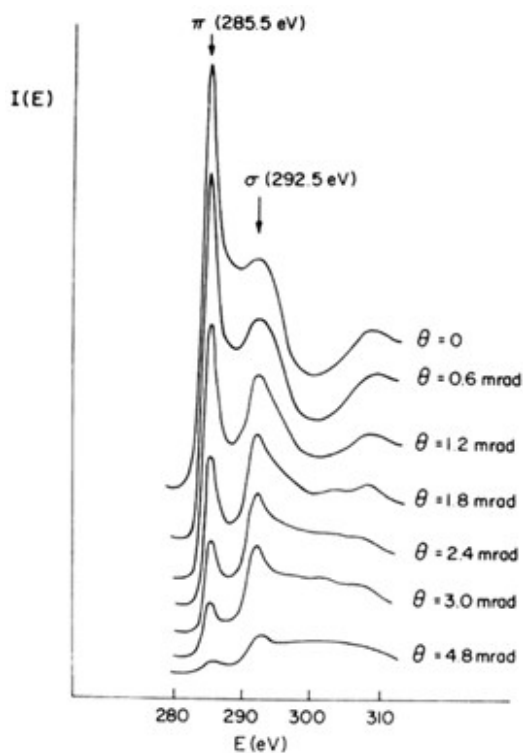


Figure 2.25: EELS spectra for graphite as a function of the scattering angle ( $\theta$ ). The electron beam is incident normal to the graphite planes [001].

specimen, although the  $\pi$ -stacking orientation of the molecules can vary within the thin-film. Therefore, anisotropy effects should still be evident for a given EELS collection angle, i.e. the relative intensity of the  $\pi^*$  and  $\sigma^*$  fine structure should

vary depending on the orientation of the molecules. Therefore, using the carbon K-edge fine structure it is possible to determine if the  $\pi$ -stacking is parallel or perpendicular to the thin-film. Furthermore, by scanning a STEM probe over the specimen and acquiring an EELS spectrum at each raster point (so-called ‘spectrum imaging’ technique (Jarausch et al., 2009)) it should also be possible to map the distribution of  $\pi$ -stacking domains. Note that for a certain EELS ‘Magic’ collection angle Daniels et al. (2003), the EELS spectrum does not show the expected changes due to anisotropy. Therefore, for accurate orientation mapping the EELS collection angle should be different from the magic angle.

## **2.6 Multislice Simulation**

We use TEM/STEM image simulation because of strong dynamic scattering of the electron beam within the specimen and the loss of phase information in practical experiments, so that it is difficult to directly correlate the image or diffraction pattern to the material structure. Moreover, we will be able to see how closely the simulated image or diffraction pattern resembles experiment, modify the model structure and repeat the process until a satisfactory convergence has been achieved. Simulations can also be used to estimate the sensitivity of a given measurement. For example, in this work simulations are used to establish the sensitivity of the STEM FEM method (section 2.5.2) to measure variance in a (computer generated) amorphous supercell which contains a small crystal. Several parameters, such as supercell thickness, size of the crystal, its depth within the supercell, and ADF detector angles can be independently varied to examine its effect on the variance. Such a high level of control is impossible to achieve in experiments, and serves as a useful guide for establishing the limits of the technique and correct interpretation of experimental results. Numerical simulation of TEM and STEM images has mainly been performed using the multislice method (Cowley and Moodie, 1959). The principle of the multislice method is illustrated in Figure 2.26, where the electron

beam is alternately transmitted through thin slices within the specimen until it reaches the exit surface. For accuracy the slice thickness must be made small, i.e.  $\sim 1 \text{ \AA}$  or an inter-atomic layer thickness (for a periodic crystal). The goal is to calculate the electron exit wavefunction  $\Psi_{exit}(\mathbf{r})$  starting from the incident wavefunction  $\Psi_o(\mathbf{r})$ .

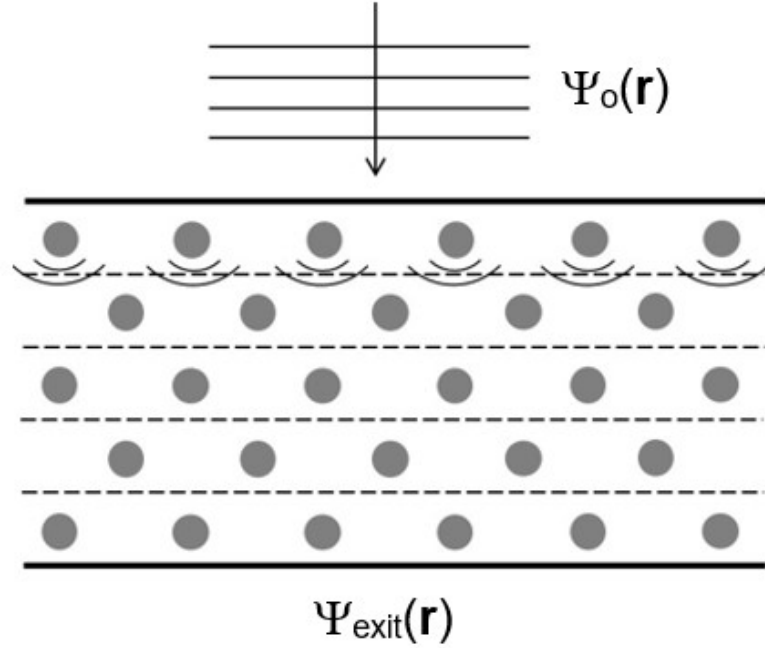


Figure 2.26: Schematic of the multislice method showing the electron beam transferred through the specimen that is divided into many thin slices.  $\Psi_o(\mathbf{r})$  and  $\Psi_{exit}(\mathbf{r})$  are the electron incident and exit wave functions.

To calculate the electron wavefunction in any given slice two types of processes must be taken into account, namely transmission and propagation. In transmission, the shortening of the electron wavelength due to the positive potential field of the nuclei in the specimen leads to a phase change in the electron wavefront. This is described by the transmission function  $Q(\mathbf{r}) = \exp[i\sigma V_z(\mathbf{r})]$  (Kirkland, 2010), where  $\sigma$  is the interaction constant and  $V_z(\mathbf{r})$  is the slice potential projected along the z-axis (i.e. electron optic axis direction). The modified electron wavefunction  $\Psi'$  is then:

$$\Psi'(\mathbf{r}) = Q(\mathbf{r})\Psi(\mathbf{r}) \quad (2.19)$$

where  $\Psi$  is the wavefunction prior to the phase shift to the positive potential.

Following transmission the modified wavefunction must be propagated through free space to the next slice. This process can be described by a convolution of  $\Psi'$  with a propagator function  $P(\mathbf{r})$ . Combining transmission and propagation the electron wavefunction for the  $n^{\text{th}}$ -slice ( $\Psi_n$ ) is related to the wavefunction in the preceding slice ( $\Psi_{n-1}$ ) via:

$$\Psi_n(\mathbf{r}) = P_{n-1}(\mathbf{r}) \otimes [Q_{n-1}(\mathbf{r})\Psi_{n-1}(\mathbf{r})] \quad (2.20)$$

where  $\otimes$  denotes convolution and  $Q_{n-1}$ ,  $P_{n-1}$  are the transmission and propagator functions for the  $(n-1)^{\text{th}}$ -slice. It is easier to evaluate Equation 2.20 in Fourier space by taking advantage of the convolution theorem, where convolution operations in real space become multiplication in reciprocal space  $\mathbf{k}$ .

$$\Psi_n(\mathbf{k}) = P_{n-1}(\mathbf{k}) \cdot FT[Q_{n-1}(\mathbf{r})\Psi_{n-1}(\mathbf{r})] \quad (2.21)$$

where ‘ $FT$ ’ denotes the Fourier transform. The reciprocal space propagator function  $P(\mathbf{k})$  is given by (Kirkland, 2010):

$$P(\mathbf{k}) = \exp(-i\pi\lambda k^2 \Delta z) \quad (2.22)$$

where  $\lambda$  is the electron wavelength and  $\Delta z$  is the slice thickness. Equation 2.21 is used iteratively to calculate the electron wavefunction at successive slices starting from the incident wavefunction  $\Psi_o$  until we reach the exit wavefunction  $\Psi_{exit}$ . In parallel beam TEM the incident wavefunction  $\Psi_o$  is a plane wave, while for STEM  $\Psi_o$  is the Airy disc of a focused probe. The TEM image can be calculated by convolving  $\Psi_{exit}$  by the lens point spread function and taking the square modulus. The lens aberration function takes into account imaging artefacts, such as defocus and spherical aberration (Williams and Carter, 1978). For STEM bright-field and dark-field images are simulated by first Fourier transforming  $\Psi_{exit}(\mathbf{x})$  to give a diffraction pattern and integrating the signal over the angular range of the detector. This gives the STEM bright-field/dark-field image intensity for a single point in the specimen. The process is repeated for each specimen point over the STEM probe raster area to build the image pixel by pixel.

---

# Multislice Simulations

## 3.1 Motivation for simulations

-There are many factors that affect the experimental detection of order in a fluctuation electron microscopy (FEM) measurement, such as particle crystalline size, depth in the sample, atomic number, and paracrystallinity. In a real sample, with a high degree of disorder, it is extremely difficult to isolate the role of a single parameter on a FEM measurement. Simulations, where the microstructure of the sample can be artificially constructed, is a suitable alternative. Any one of the parameters of interest can be systematically varied, while keeping other parameters constant. Numerical simulation of TEM and STEM images has mainly been performed using the multislice method (Ishizuka, 2002). In this chapter multislice simulations (section 2.6) are used to investigate the effect of microstructural parameters on scanning transmission electron microscopy FEM (STEM FEM). In particular, we focus on the detection limits of the ‘integrated’ STEM FEM method used in this thesis, where the scattering is integrated over the annular dark field detector (section 2.5.2). This is important since conventional STEM FEM measurements in the literature are based on scattering along a fixed wavevector, and there are no results on the ‘integrated’ STEM FEM approach. In the literature, multislice STEM FEM simulations have been carried out on amorphous Ge by Julian et al. (Julian et al., 2018). They did a simulation for ten different paracrystalline mod-

els chosen from the work of Bogle et al (Bogle et al., 2007), surrounded by a wholly amorphous layer modelled using the continuous random network (CRN) model (Barkema and Mousseau, 2000). In this way, the STEM FEM variance (Equation 2.13, section 2.5.1) can be calculated for each scattering vector  $\mathbf{k}$ , and compared to experiment. This is however, a very complex problem because of the need to model the microstructure accurately, and the high computational costs involved in simulating a large multislice supercell (11x11x33 nm<sup>3</sup>) in STEM mode, where the diffraction pattern at each beam raster point must be simulated. To simplify our work, we built a simple model that deals with only one crystalline particle surrounded by an amorphous matrix, the latter generated by random displacement of atoms starting from a crystalline lattice. The amorphous region does not therefore reproduce the same level of detail as a CRN model, but this is expected to play only a minor role in electron beam scattering for sufficiently thick specimens (few tens of nm). Furthermore, since only one crystalline particle is simulated, a value for variance cannot be generated. Instead, we focus on the minimum detection limit of parameters such as crystalline particle size, depth within the specimen, atomic number and paracrystallinity at 20 nm thickness.

### 3.1.1 Simulation procedure

A program is used to produce a supercell that generates a crystalline region of [100] diamond cubic carbon surrounded by an amorphous carbon matrix, as shown in Figure 3.1a. At the start of the program the entire supercell is crystalline with [100] diamond cubic orientation and lattice parameter 3.57 Å. The user can define the crystalline region within the supercell, while all atoms outside this region will be made amorphous through random displacement. We circle out a radius (R) for the crystalline particle that has a maximum value 3 nm, because the supercell half-width is 4 nm. We have chosen three different radii 1, 2, and 3 nm for simulation. We are also able to specify the depth (d) of the particles within the supercell. Because the thickness for the supercell is 20 nm, the depth is specified to be 3, 10,

and 17 nm, i.e. close to the electron beam entrance surface, middle of the specimen and close to the beam exit surface respectively.

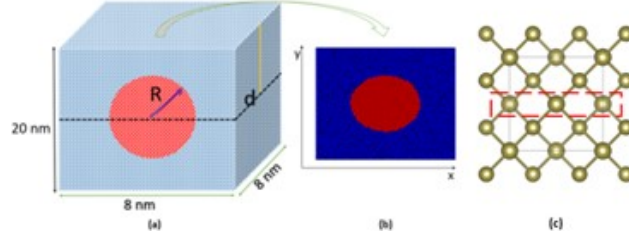


Figure 3.1: Schematic of a supercell 8 nm dimension and 20 nm thickness including crystalline (red) and amorphous (blue) regions., a) crystalline particle at a selected radius  $R$  and depth  $d$ . The particle has a diamond cubic crystal structure and  $[100]$  orientation to the incoming electron beam. All atoms are carbon. b) shows the atomic structure of the crystalline particle surrounded by amorphous regions as viewed from the top surface of the supercell. c) is the projected crystal structure of the diamond unit cell viewed along the  $[100]$  orientation. the dashed box indicates the slices used for multislice simulations.

After setting the radius and depth, we apply random displacements to the atoms outside the particle radius  $R$  to generate amorphous regions. The magnitude of the random displacement can be set by the user. The orientation of the displacement vector is also chosen using a random number generator in the computer. The simulations have been performed using a  $1.0 \text{ \AA}$  displacement magnitude for the amorphous region. This value was obtained by multislice simulating the convergent beam diffraction pattern for the ‘amorphous’ region generated using several different trial displacement magnitudes. Results for  $0.1$ ,  $0.5$  and  $1.0 \text{ \AA}$  displacement magnitudes are shown in Figure 3.2. With increasing displacement magnitude the Bragg discs from the starting  $[100]$  diamond cubic crystalline structure disappear and the diffraction pattern becomes more amorphous. At  $1.0 \text{ \AA}$ , we get only the characteristic halo pattern of amorphous specimens.

Having generated the supercell the sampling used for multislice must be determined. When an image does not have equal dimensions, as seen in Figure 3.3, it is calculated as  $(N_x) \times (N_y)$  pixels. The images are sampled at  $N_x$  discrete points along  $x$  and  $N_y$  discrete points along  $y$ , resulting in a supercell with real-space dimensions of  $a \times b$ . Each pixel in real space has the dimensions  $(a/N_x) \times (b/N_y)$

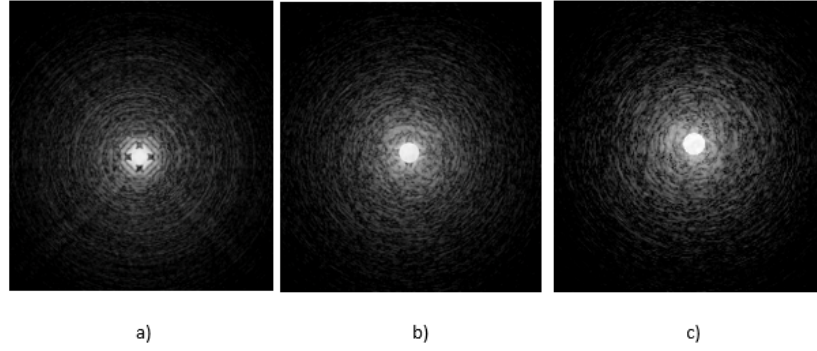


Figure 3.2: Multislice simulated convergent beam electron diffraction patterns for different amorphous displacements, a) 0.1 Å, b) 0.5 Å and c) 1.0 Å. The supercell thickness is 20 nm. The probe parameters are 200 kV, 5.3 mrad semi-convergence angle and 643 Å underfocus (Scherzer condition). The results are the average of 10 frozen phonon configurations.

and a single intensity value associated with it that is the average over the pixel's area.

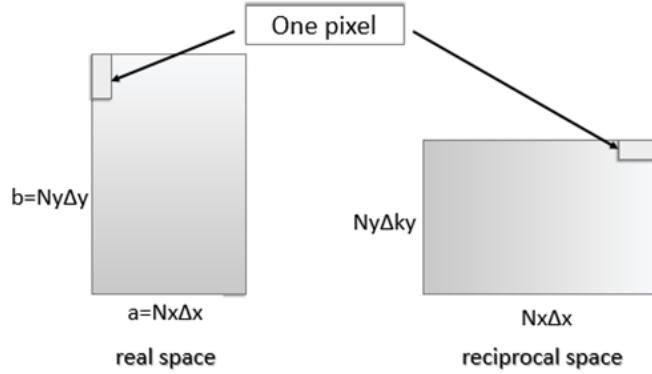


Figure 3.3: An image of size  $a \times b$  is sampled in a plane perpendicular to the microscope's optic axis. In real space, there are  $(N_x) \times (N_y)$  pixels of size  $(a/N_x) \times (b/N_y)$ , whereas in reciprocal space, the pixel size is  $(1/a) \times (1/b)$ . The figure is for a non-square supercell (Kirkland, 2010).

Since in our case the supercell lateral dimensions is a square,  $N_x$  and  $N_y$  will be equal and denoted by  $N$ . We choose a real space dimension of 8nm by 8nm because it has to be larger than the maximum particle size (radius 3 nm) and it should be a sufficient size to allow for electron beam scattering within the specimen. To verify 8 nm is a suitable value, two conditions have to be satisfied. First, we want to sample the atomic potential accurately in real space in order to calculate the

multislice transmission function  $Q$  (see Equation 2.19, section 2.6). If we consider the x-direction, only discrete values are taken into account:

$$x = ix\Delta \quad (3.1)$$

, where  $i = 0, 1, 2, 3, \dots, (N - 1)$ .

The size of the pixel is therefore:

$$\Delta x = a/N \quad (3.2)$$

where  $a$  is the supercell size in the plane perpendicular to the optic axis.

Equation 3.2 enables us to estimate if the atomic potential is sampled at sufficient resolution. For a 8 nm supercell and  $N = 1024$  pixels, we got 0.1 Å for the pixel size. This is smaller than the L shell Bohr radius for the carbon atom (0.35 Å), indicating that this value is appropriate for the real space part of the multislice.

The second condition is to make sure that the scattering angle in reciprocal space is large enough. For a supercell of  $a \times b$  dimensions in real space the Fourier transform dimensions of each pixel is  $1/a \times 1/b$ . This shows that the larger the dimension of the supercell in real space the smaller the pixel size in reciprocal space. The maximum dimension ( $\Delta k_{max}$ ) in reciprocal space coordinates is therefore:

$$\Delta k_{max} = \frac{2N}{3(2a)} \quad (3.3)$$

The extra factor of 2/3 is due to bandwidth limiting for reducing aliasing artefacts in the multislice simulation (Kirkland, 2010). The scattering angle is giving by  $\lambda \Delta k_{max}$ , where  $\lambda$  is the electron wavelength. The maximum scattering angle using equation 3 becomes:

$$\alpha_{max} = (2/3)\lambda \times (N/2a) \quad (3.4)$$

Maximum angle using Equation 3.4 was found to be 107 mrad. The Bragg angle for diamond cubic carbon is less than 10 mrad, which means that we are simulating out to many orders of Bragg scattering, and sampling both the coherent and incoherent scattering regimes. Such a large scattering angle can also allow us to consider that the detector outer angle is effectively infinite and therefore we are including all the scattering from the sample. Finally, we selected 0.9 Å for the slice thickness periodicity along [100] using the equation below:

$$\Delta Z = \frac{a_0}{\sqrt{h^2 + k^2 + l^2}} \quad (3.5)$$

where the lattice parameter for carbon ( $a_0$ ) is 3.57 Å and Miller indices  $\sqrt{h^2 + k^2 + l^2}$  for (400) planes is 4. This slice thickness was chosen based on the periodic repeat distance of a diamond cubic crystal structure along the [100] direction (see Figure 3.1c).

As an electron propagates through a specimen, it interacts intensely with it and can scatter multiple times. Dynamical scattering occurs when an incident electron has scattered many times as it passes through a specimen, so that the scattered beams have acquired appreciable intensity. The diffraction pattern contains much useful information about the structure of the specimen (section 2.4). Here diffraction patterns were simulated by summing the results from 20 different frozen phonon configurations. Frozen phonons are required to reproduce thermal diffuse scattering, as well as Kikuchi bands and Bragg diffracted beam intensities in crystalline specimens (Kirkland, 2010). A frozen phonon configuration is generated by assuming the Einstein model, where the vibration of each atom is calculated independently using the Debye-Waller factor for diamond. The frozen phonon is a ‘snapshot’ of the specimen vibration as seen by the swift, incident electron, which passes through the solid in a time shorter than the phonon vibration period. The reason for choosing 20 frozen phonons is that there was very little difference compared to a larger simulation involving 50 frozen phonon configurations. The lower

value of 20 is therefore chosen, since the results have sufficiently converged and the run time of the programme is faster (30 mins per calculation for a standard 3 GHz desktop computer). Example diffraction patterns for a STEM probe incident on the crystalline and amorphous regions of the supercell are shown in Figure 3.4. The high intensity central beam has been blocked out to display the Bragg spots better.

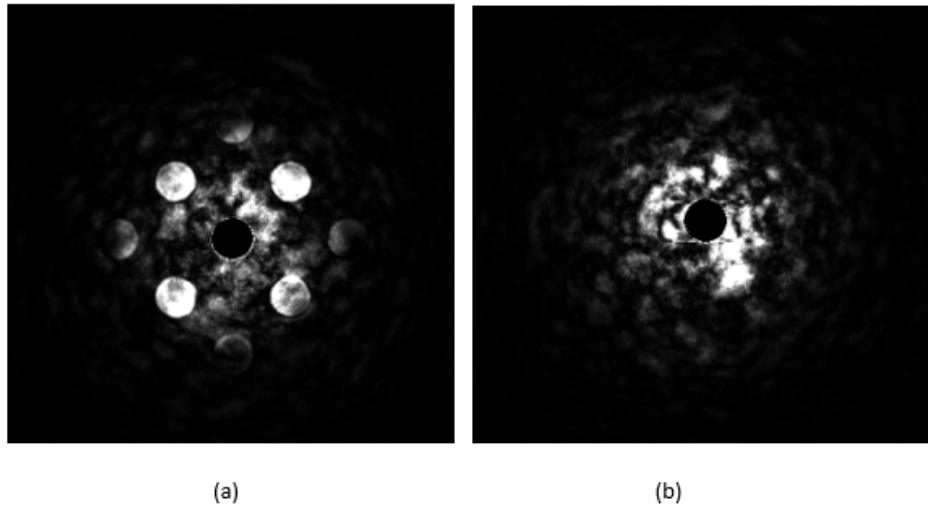


Figure 3.4: Simulated diffraction patterns obtained from an amorphous carbon supercell of dimension  $8 \times 8 \times 20$  nm, with a crystalline particle of radius 2nm at 10 nm depth (diamond cubic crystal structure). The electron beam parameters are 200 keV energy,  $C_s = 1.1\text{mm}$  and  $643 \text{ \AA}$  underfocus (Scherzer condition). (a) and (b) show diffraction patterns with the probe incident along the crystalline and amorphous regions respectively. The central beam has been blocked to display the weaker scattering better.

The simulated diffraction patterns can be used to calculate the ‘virtual dark-field (DF)’ intensity as a function of the scattering inner angle ( $\alpha_{inner}$ ). This is schematically illustrated in Figure 3.5, which shows the diffraction space between  $\alpha_{inner}$  and the maximum simulated scattering angle  $\alpha_{max}$  (Equation 3.4). The virtual DF intensity is obtained by summing the pixel intensities within this region. Because  $\alpha_{max}$  is very large (107 mrad), and scattering from the sample has decreased to nearly zero at this value, the calculated value for the virtual DF intensity effectively represents scattering to angles beyond  $\alpha_{inner}$ . A Digital Micrograph script is used to extract the virtual DF intensity as a function of  $\alpha_{inner}$ , and the results

for the crystalline and amorphous diffraction patterns in Figure 3.4 are shown in Figure 3.6 respectively.

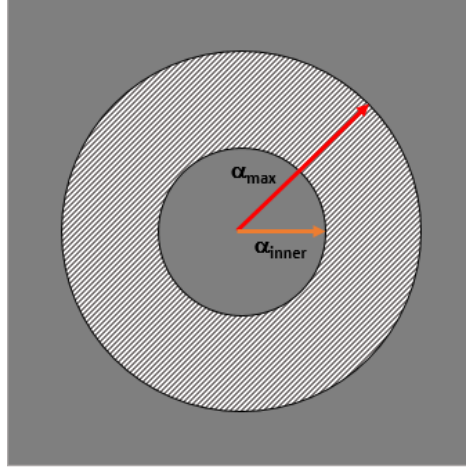


Figure 3.5: Schematic showing the scattering inner angle  $\alpha_{inner}$  and maximum simulated scattering angle  $\alpha_{max}$  used for calculating the virtual dark-field intensity.

As expected the virtual DF intensity decreases monotonically with inner scattering angle, although the intensity for the crystalline region is higher at smaller scattering angles ( $<30$  mrad), due to the presence of Bragg diffraction spots. The contrast ( $C$ ) for a given inner angle can be defined as follows:

$$C(\alpha_{inner}) = \left( \frac{I^c(\alpha_{inner}) - I^a(\alpha_{inner})}{I^a(\alpha_{inner})} \right) \times 100\% \quad (3.6)$$

where  $I^c$  and  $I^a$  are the virtual DF intensities in the crystalline and amorphous diffraction patterns respectively. The contrast ‘ $C$ ’ is a measure of the visibility of the crystalline region with respect to the amorphous matrix for an annular DF-imaged formed with inner angle  $\alpha_{inner}$ . Note that in order to observe contrast due to crystallinity the detector inner angle must be sufficiently small to include Bragg reflections from the crystalline particle. Crystalline particles with large contrast are expected to contribute strongly to the variance measured in an ‘integrated’ STEM FEM measurement (see Figure 2.20, section 2.20). Therefore, contrast can be used as an indirect measure of the various factors (particle size, depth etc) governing

detectability limits in the experiment. The contrast curve for Figure 3.6 is shown in Figure 3.7, where, as expected, the contrast is largest at the small scattering angles.

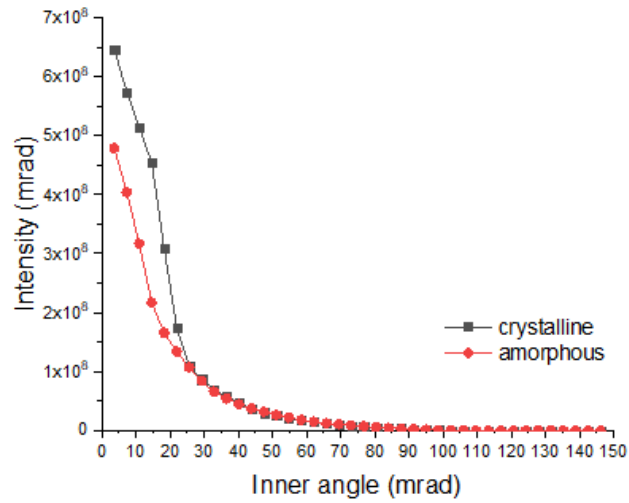


Figure 3.6: Virtual dark-field intensity as a function of scattering inner angle (mrad) for the crystalline and amorphous diffraction patterns in Figure 3.4.

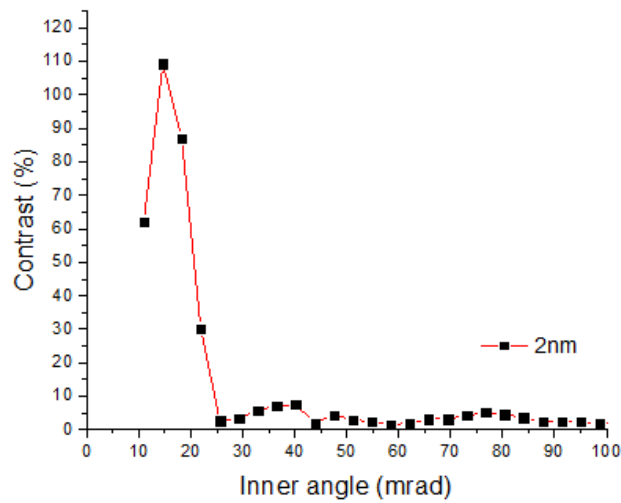


Figure 3.7: Contrast as a function of scattering inner angle for the results shown in Figure 3.6.

## 3.2 Results and discussion

### 3.2.1 Radius and atomic number

Figure 3.8 depicts the simulated diffraction patterns for two distinct crystalline particle radii (1 nm and 3 nm) embedded in an amorphous carbon matrix. The particles were positioned in the middle of a specimen 20 nm thick. Unlike 1 nm, which shows only weak Bragg reflections, the 3 nm radius particle shows strong Bragg spots in the diffraction pattern. Equation 2.1 from Chapter 2 was used to confirm the Bragg spots to be 220 type reflections, consistent with a  $2\theta$  Bragg angle of 20 mrad. Because the supercell contains a small crystal in a vast amorphous matrix, the first order of the 220 Bragg beams can only be detected at 3 nm, and the scattering is not strong enough to show subsequent systematic row reflections, such as 440 etc, although the vector sum 400 of two of the 220 reflections is weakly present.

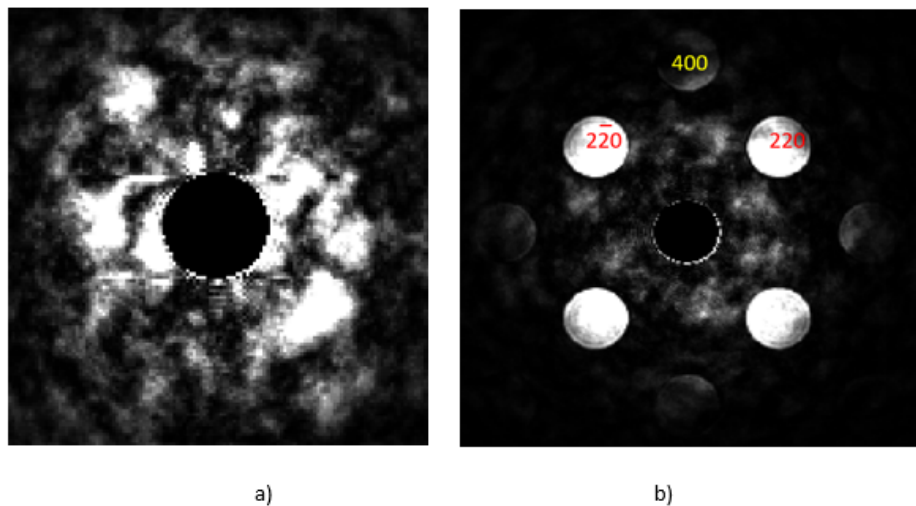


Figure 3.8: Simulated diffraction patterns obtained from a 20 nm thick amorphous carbon specimen with a crystalline particle at 10 nm depth. A) 1 nm and b) 3 nm particle radius

A contrast plot is shown in Figure 3.9a for three different radii: 3 nm, 2 nm, and 1 nm in carbon. The 3 nm particle has the highest contrast, which gradually

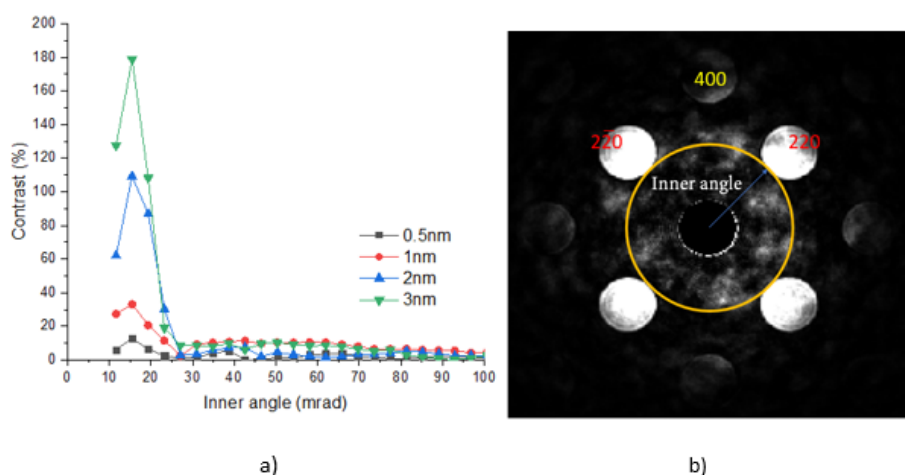


Figure 3.9: Contrast as a function of scattering inner angle for carbon with particle radii 3 nm, 2 nm, 1 nm and 0.5 nm. The crystalline particles are at 10 nm depth in an otherwise 20 nm thick amorphous carbon specimen. B) Diffraction pattern for 3 nm radius particle showing the inner angle at maximum contrast.

decreases with radius as expected. The graph shows very large contrast values at small inner angles between 10 and 20 mrad and then drops close to zero, with relatively minor increases at larger inner angles that can be seen in the graph. The high contrast is likely due to the 220 reflections, although the maximum contrast is at 15 mrad, which is smaller than the  $2\theta$  Bragg angle of 20 mrad. Due to the convergence angle of the electron probe the Bragg disc is broadened between 15-25 mrad. When calculating contrast the intensity of the diffraction pattern is integrated between a variable inner angle and fixed outer angle. This means that the contrast will be greatest when the inner angle is just touching the 220 Bragg discs, as shown in Figure 3.9b, since then the entire Bragg disc will contribute to the contrast. This explains the discrepancy between the contrast maximum and  $2\theta$  Bragg angle. Increasing the inner angle further will lower the contrast, since only a smaller fraction of the Bragg disc can contribute, until at 25 mrad the inner angle is larger than the Bragg disc and the contrast is close to zero, due to the absence of higher angle Bragg scattering. As a rule of thumb, we can detect particles that are 0.5 nm radius size in 20 nm carbon matrix, since the maximum contrast for this case is approximately 10% higher than the amorphous background.

We can explore the effect of atomic number on contrast by replacing carbon with a higher atomic number element, such as germanium (Ge). Due to the stronger scattering of Ge, the amorphous supercell structure was created by increasing the random displacement of atoms from 1.0 Å to 1.5 Å (section 3.1.1). Similar to carbon, crystalline particles of variable size were placed at 10 nm depth in an otherwise amorphous matrix, with the specimen thickness being 20 nm. The 3 nm radius particle shows strong Bragg spots in the diffraction pattern, while 1 nm shows only weak Bragg reflections (Figure 3.10). Due to the stronger scattering of Ge, both the 220 and second order 440 reflections are weakly observed for the 3 nm particle. Compared to carbon the diffracted beams are closer to the unscattered beam, due to the larger lattice parameter of Ge (5.7 vs 3.6 Å). Consequently, the  $2\theta$  Bragg angle is only 12.5 mrad.

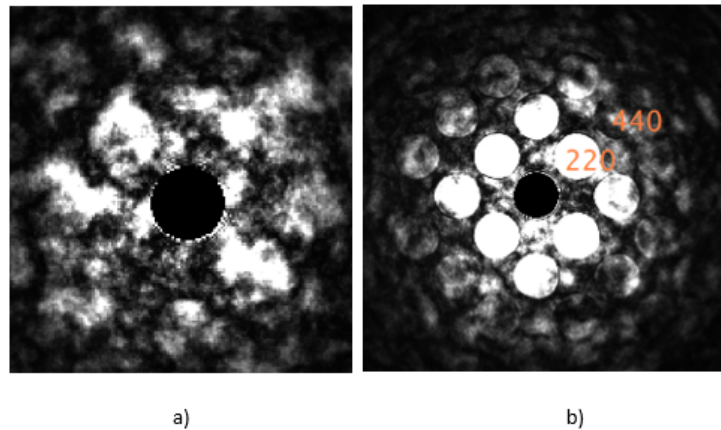


Figure 3.10: . Simulated diffraction patterns obtained from a 20 nm thick amorphous germanium specimen with a crystalline particle of radius a) 1 nm and b) 3 nm positioned at 10 nm depth.

Figure 3.11 shows the contrast for Ge at three distinct radii: 3 nm, 2 nm, and 1 nm. The largest contrast is seen at 3 nm particle radius, which gradually decreases with radius as expected. The graph demonstrates that contrast values are very large for small inner angles around 10 mrad, before decreasing at larger inner angles. A second broad peak can also be seen at much larger inner angles of 85 mrad in the curves for 2 and 3 nm particle sizes. The contrast in Ge extends to a broader range of inner angles than carbon due to stronger scattering from the

higher atomic number. Furthermore, plotting the diffraction patterns for the 2 nm and 3 nm particles in a logarithmic intensity scale reveals the presence of higher order Laue Zone (HOLZ) rings, as shown in Figure 3.12. The HOLZ ring is due to the curvature of the Ewald sphere, cutting through upper Laue zone layers at high scattering angles. The presence of the HOLZ ring for the 2 nm and 3 nm particles gives rise to the second contrast peak observed in Figure 3.11.

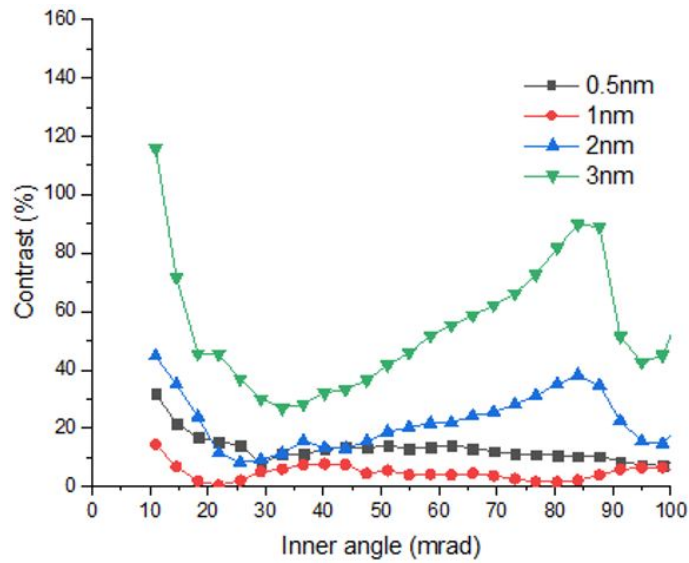


Figure 3.11: Contrast as a function of scattering inner angle for germanium with particle radii 3 nm, 2 nm, 1 nm and 0.5 nm. The particles are at 10 nm depth in an otherwise amorphous specimen 20 nm thick.

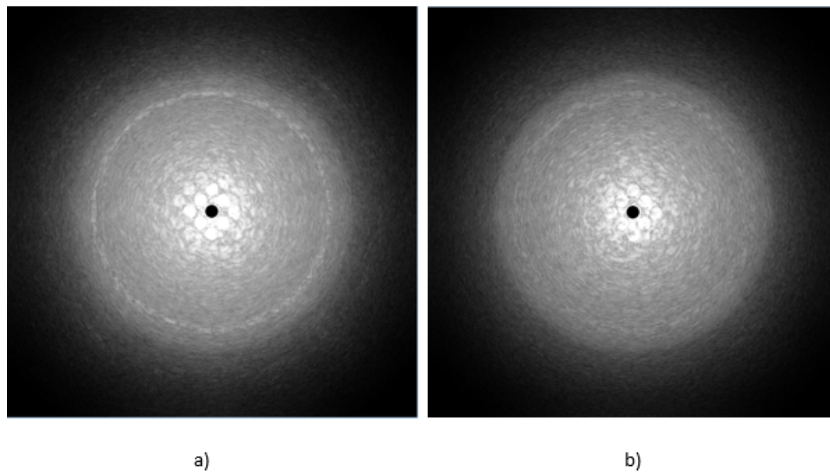


Figure 3.12: Simulated diffraction patterns (log intensity scale) obtained from a 20 nm thick amorphous germanium specimen with a) 3 nm and b) 2 nm radius crystalline particle at 10 nm depth.

Figure 3.11 further indicates that at small inner angles, the contrast at 0.5 nm is higher than 1 nm particle size, which is unexpected. The 0.5 nm and 1 nm particle diffraction patterns look quite similar when plotted on a log scale (Figure 3.13) and do not show strong Bragg discs. The Ge lattice parameter is only 5.7 Å, which means that these particles only contain a handful of unit cells within its volume. Scattering will therefore be very small in this situation, and it will be difficult to build up any significant intensity in the Bragg diffracted beams for such small crystals. Boundary effects are also likely to affect the diffracted beam intensity for these small crystals, which is probably the reason for the anomalous contrast. However, the 2nm and 3nm particles are large enough to follow the expected trends.

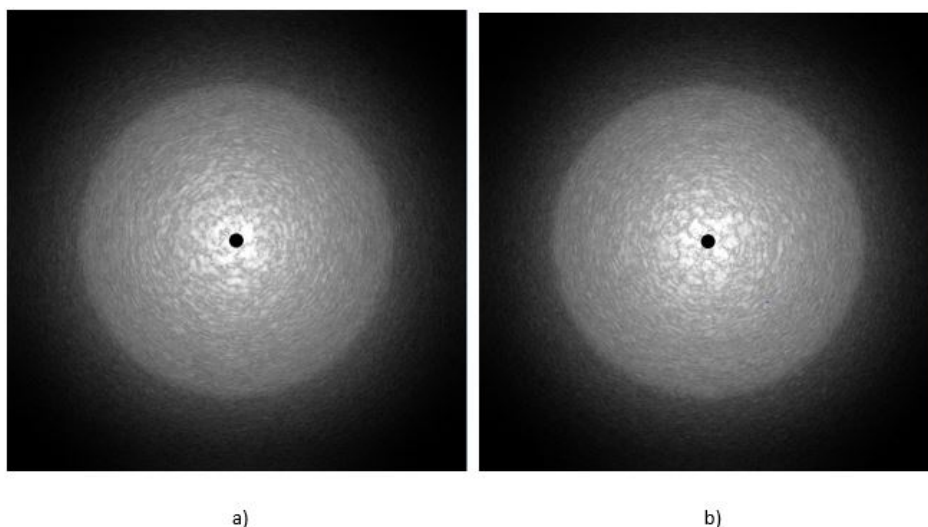


Figure 3.13: Simulated diffraction patterns (log scale) obtained from a 20 nm thick amorphous germanium specimen with a crystalline particle of radius a) 0.5 nm and b) 1 nm positioned at 10 nm depth.

To conclude this section we compare the minimum detectable particle size in our simulations with experimental data in the literature. Treacy and Gibson (Treacy and Gibson, 1996) have published variable coherence FEM images for amorphous Ge, a typical example of which is shown in Figure 3.14. The image shows an experimental hollow-cone TEM dark field image from a 14.4 nm thickness sample, acquired at 100 kV energy. Although these results are for TEM, they are related to the STEM simulations in this work through the principle of reciprocity (section

2.1.2). Nevertheless key differences remain, such as specimen thickness (14 nm vs 20 nm) electron beam energy (100 keV vs 200 keV) and illumination/detector angles. We chose 10 different particles that appeared distinct in the image at random and measured their size using Gatan Digital Micrograph (DM) proprietary software. The mean average radius of the Ge particles is 2.9 nm and the smallest measured particle radius was 2.2 nm. This is consistent with the simulation results which indicate that the contrast of 2-3 nm Ge particle size is sufficiently strong to be easily detected (Figure 3.11). Smaller particle sizes may also contribute to Figure 3.11, but their lower contrast make them harder to separate from the background intensity.

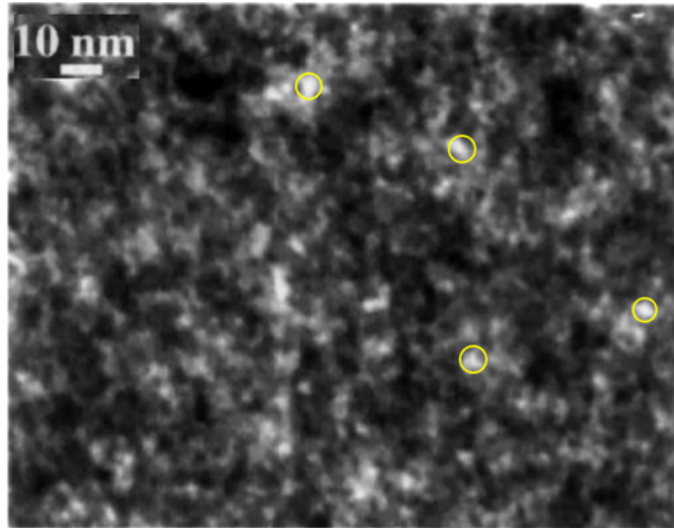


Figure 3.14: Hollow-cone TEM dark-field image of amorphous Ge with 14.4 nm specimen thickness. The scale bar is 10nm (Treacy and Gibson, 1996). The circled particles were randomly chosen for particle size analysis.

### 3.2.2 Particle depth in the specimen.

In a real specimen the crystalline particles will be distributed at random depths within the amorphous matrix. In this section we will explore the role of specimen depth through simulation. For example, a STEM probe diameter is smallest at the specimen entrance surface, but as it propagates through an amorphous specimen it will undergo geometric broadening and scattering. The illumination of a particle

close to the entrance surface is therefore very different to the same particle at larger depth. In the simulations the specimen thickness and particle radius are fixed at 20 nm and 2 or 3 nm respectively, but the depth is varied as 3 nm (near electron beam entrance surface), 10 nm (middle of specimen) and 17 nm (close to beam exit surface). Figure 3.15 shows the contrast for carbon particles of radius 2 nm and 3 nm at the three different depths 3 nm, 10 nm, and 17 nm. The graphs show very large contrast values at small inner angles of 15 mrad and then drops close to zero; the interpretation of the contrast is described in section 3.31. The particle with the highest contrast is at a depth of 10 nm, followed by 17 nm and 3 nm (note that we are referring to the maximum contrast value, rather than contrast at any given inner angle). The effect of geometric spreading of the electron beam as it propagates through the specimen thickness is illustrated in Figure 3.16 and can be calculated using the following equation:

$$X = \tan(\theta) \times \text{depth} \quad (3.7)$$

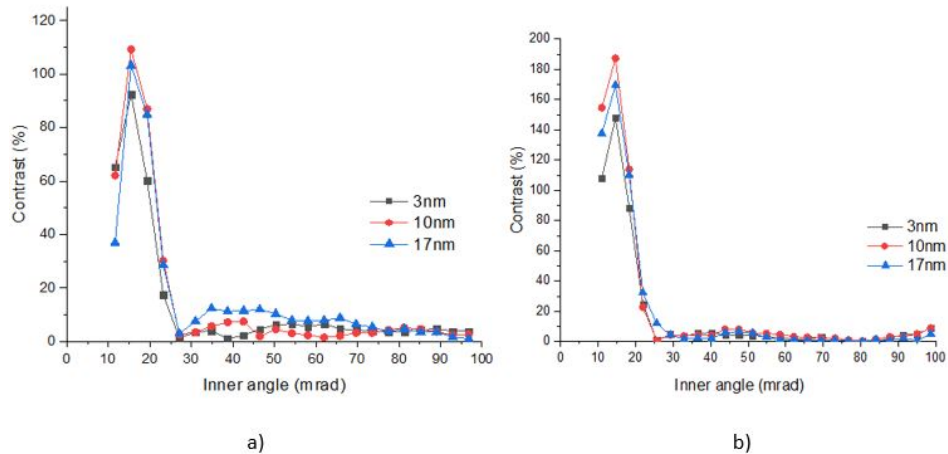


Figure 3.15: Contrast as a function of scattering inner angle for carbon at depths 3 nm, 10 nm and 17 nm in a 20 nm thick amorphous specimen. The particles size is a) 2 nm and b) 3 nm.

, where  $X$  is the beam radius at a given depth and  $\theta$  is the probe semi-convergence angle. A calculation for our STEM probe ( $\theta = 5.3$  mrad) gives a value of 0.053nm for the beam radius at 10 nm specimen depth. This is much smaller than the

particle radius of 2-3 nm and so the electron beam will fall entirely within the particle, as illustrated in Figure 3.16. In practice, scattering will increase the beam radius slightly further, but is not expected to change the main conclusion of a beam radius smaller than the crystalline particle due to the low atomic number of carbon. The reason for the higher contrast in the middle of the specimen is unknown. Note that the contrast is very large for all specimen depths, so that although 10 nm depth gives the highest contrast, 2-3 nm radius particles close to the beam entrance and exit surfaces would still be clearly visible, since the probe spreading remains smaller than the particle size.

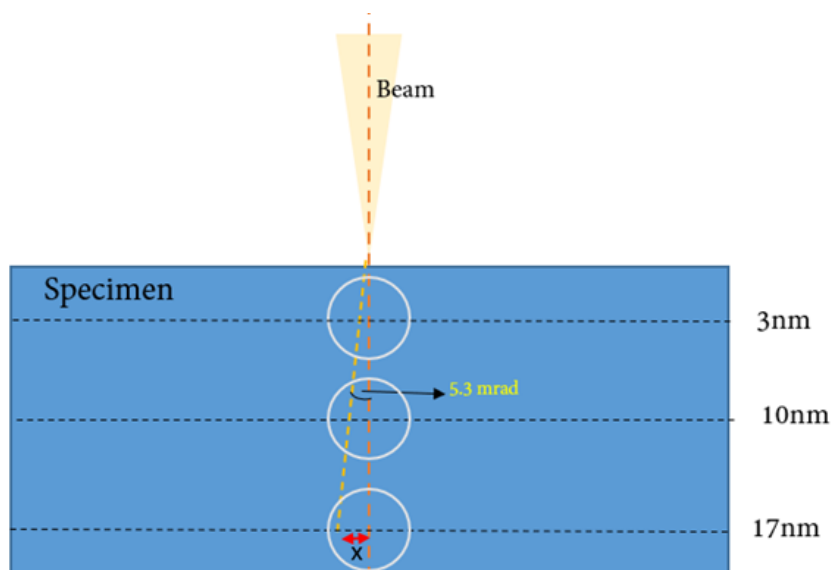


Figure 3.16: Schematic illustrating the effect of geometric spreading of a STEM probe with 5.3 mrad semi-convergence angle for particles located at different specimen depths. The diagram is not drawn to scale.

Simulations have also been carried out where carbon is replaced with germanium. For Ge particles, the results for 2 nm shows a different trend with respect to specimen depth compared to the 3 nm particle (Figure 3.17). For the former the maximum contrast is slightly larger close to the exit surface (17 nm) compared to the entrance surface (3 nm), while the opposite trend is observed for the latter. Similar to carbon the highest contrast is observed for a particle in the middle of

the specimen (10 nm), although the contrast is still high at all specimen depths investigated. This suggests that the ‘integrated’ STEM FEM method is suitable for detecting particles with a minimum radius of at least 2 nm in specimens that are approximately 20 nm thick using a 200 kV electron beam with 5.3 mrad semi-convergence angle. Note that much larger STEM probe semi-convergence angles (e.g. 20-30 mrad) reduces the depth of field, so that the particle depth within the specimen is likely to be more important (van Benthem et al. (2005)). However, such large probe angles require correcting the spherical aberration in the objective lens, which is not available in the microscopes used in this study.

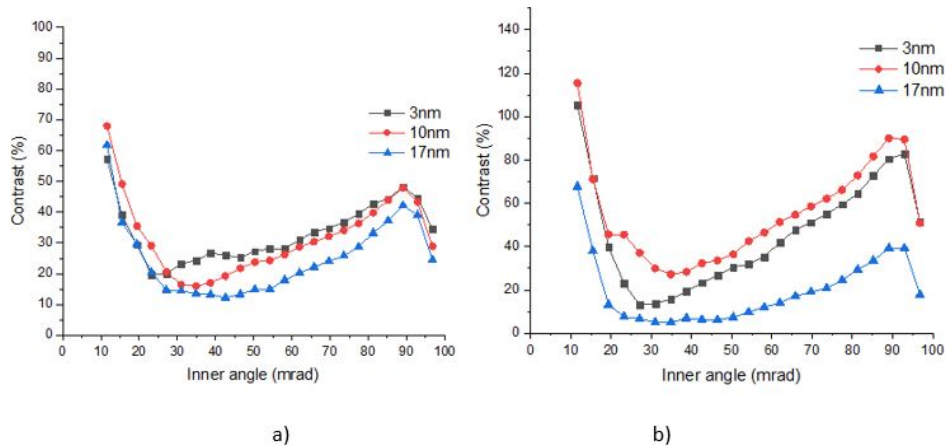


Figure 3.17: Contrast as a function of scattering inner angle for Ge at depths 3 nm, 10 nm and 17 nm in a 20 nm amorphous specimen. The particles radius is a) 2 nm and b) 3nm.

### 3.2.3 Para-crystallinity in the specimen.

Crystalline grains embedded in a disordered matrix can be deformed by strain to form para-crystalline particles. Short- and medium-range ordering (SRO-MRO) is present in their lattice, but they lack crystal-like long-range ordering in at least one direction (Voyles et al., 2001b). Paracrystallinity in nanoscale materials can be characterised in real and reciprocal space using scanning transmission electron microscopy (Savitzky et al., 2016), where their existence has been proved by diffraction analyses. However, because experimental techniques applied to real systems

can sometimes be challenging to interpret, simulation has been used to systematically investigate the role of para-crystallinity on the contrast. Two distinct crystalline particles radii (i.e. 2 nm and 3 nm) have been simulated. Para-crystallinity was introduced by a random displacement in the otherwise perfect crystal lattice. For both carbon and Ge, the displacement amplitude was 0 Å (perfect crystal), 0.10 Å, and 0.20 Å. The particle was positioned in the middle of a 20 nm thick amorphous specimen. The results for carbon and Ge are shown in Figures 3.18 and 3.19 respectively. As expected for carbon the highest contrast is found at 0 Å displacement, when the particle is perfectly ordered and Bragg diffraction is at its strongest. With increased displacement, and therefore higher para-crystallinity, the contrast decreases.

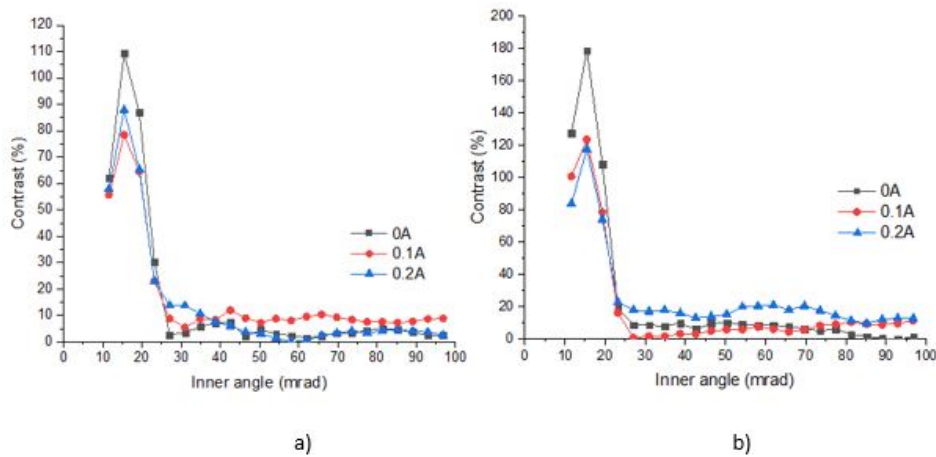


Figure 3.18: Contrast as a function of scattering inner angle for carbon at para-crystallinity displacements of 0 Å, 0.10 Å and 0.20 Å in a 20 nm thick amorphous specimen. The particles size is a) 2 nm and b) 3 nm.

The para-crystalline contrast for Ge (Figure 3.19) is however more complicated. For example, the change in contrast is more significant at large inner angles (i.e. HOLZ region, 80-100 mrad) compared to small inner angles (<20 mrad). These trends can be qualitatively explained using Bragg's law. The d-spacing for the 220 reflection is 2.01 Å for Ge and 1.27 Å for carbon. The d-spacing for the HOLZ ring in Ge is 0.13 Å at 93 mrad scattering angle (Figure 3.12). A 0.20 Å para-crystalline

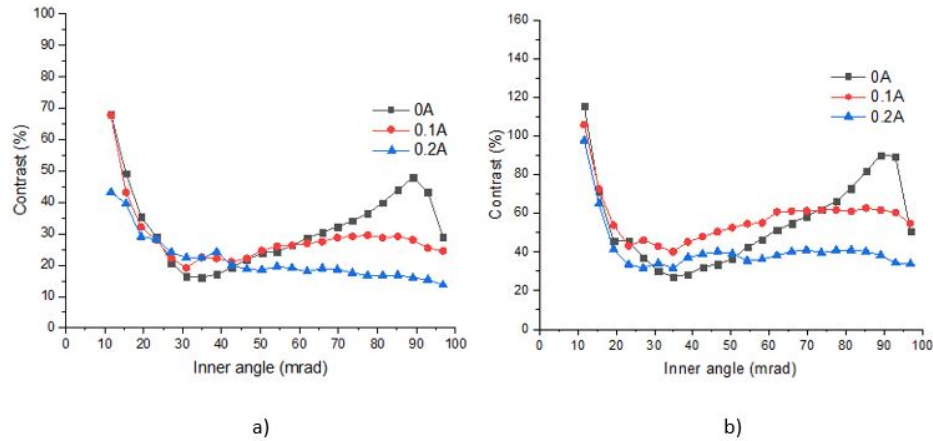


Figure 3.19: Contrast as a function of scattering inner angle for Ge at para-crystallinity displacements of 0 Å, 0.10 Å and 0.20 Å in a 20 nm amorphous specimen. The particles radius is a) 2 nm and b) 3nm.

displacement will therefore have a larger effect on 220 Bragg scattering in carbon compared to Ge. For example, the change in 220 d-spacing is at most 15% for carbon and 10% for Ge (note that the important parameter is the displacement component along the crystal plane normal, since the component parallel to the crystal plane do not alter the d-spacing). Therefore, we expect larger changes in contrast at small inner angles in carbon compared to Ge. A 0.20 Å para-crystalline displacement is nevertheless of a similar magnitude to the Ge HOLZ ring d-spacing, and therefore there are significant changes in the contrast at high inner angles.

### 3.3 Summary and conclusions

The effect of microstructural parameters on STEM FEM was examined using multislice simulations. Results were obtained for carbon and Ge as a function of the crystalline size of the particles, particle depth in the specimen, and their para-crystallinity. Using a crystalline region of [100] diamond cubic carbon and Ge with radius between 0.5 nm and 3.0 nm surrounded by an amorphous matrix, a supercell with 8 nm square dimension and 20 nm thickness was constructed. The ‘virtual’ dark-field (DF) intensity was calculated using simulated diffraction patterns for the STEM probe positioned at the particle position as well as neigh-

bouring amorphous regions. The maximum contrast was at inner angle 15 mrad due to 220 Bragg diffraction. Simulations where the particle was positioned at the centre of the supercell and its radius varied indicated that the minimum detectable particle size could be as small as 0.5 nm. An analysis of a FEM TEM micrograph for amorphous Ge published in the literature gave a larger value of 2-3 nm for the minimum detectable particle size. There could be several reasons for the discrepancy between experimental and simulation values for the minimum particle radius, such as differences in imaging parameters (e.g. TEM vs STEM, electron beam energy, specimen thickness etc), and inaccuracies in the simulation, such as a highly simplified microstructure consisting of only a single crystalline particle. Simulations also revealed a subtle dependence of contrast on the particle depth within the specimen, although the contrast is sufficiently high to detect all 2-3 nm particles within the specimen. This implies that there is no selection bias in the measurement. Para-crystallinity was found to influence the contrast in carbon at small inner angles, while for Ge the effect is stronger at large inner angles. These trends can be qualitatively explained by comparing the para-crystalline displacement with the relevant d-spacing giving rise to Bragg diffraction.

---

# STEM and 4D STEM

## 4.1 Motivation

In this chapter experimental results for the ‘integrated’ STEM FEM method will be presented. As described in chapter 2 this is a new method being explored to quantify disorder in organic-based materials. Multislice simulation results for highly simplified supercells were presented in chapter 3. Real organic materials have much more complex microstructures and are also susceptible to electron beam damage. The ‘integrated’ STEM FEM method was therefore first tested on nanocrystalline nickel oxide (NiO). NiO is a well characterised sample that is stable under the high energy electron beam typically used in a TEM. NiO is not a conjugated polymer but is used as a control polycrystalline material to test the STEM FEM imaging method outlined in section 2.1.2. In a polycrystalline material, some grains will be in the correct orientation for strong Bragg diffraction, while other grains will only be weakly scattering. This is similar to scattering expected from a semi-crystalline polymer, with the weakly diffracting NiO grains corresponding to amorphous regions and strongly diffracting NiO grains corresponding to favourably oriented crystalline regions.

There are two methods for acquiring the STEM FEM data. The first is to acquire

a series of annular dark-field images at a given camera length. The variance is calculated from the dark-field images. By systematically changing the camera length the variance can then be plotted as a function of detector inner angle (section 2.1.2). This approach was tested on NiO using the microscope at Durham University, but did not yield successful results due to detector limitations (section 4.3.3). The second method is to use 4D STEM, where the diffraction pattern is acquired at each STEM beam position in the scanned region. In the literature, 4D-STEM has been widely used, for example by Yang et al. (Yang et al., 2015), Fatermans et al. (Fatermans et al., 2018), Hachtel et al. (Hachtel et al., 2018) and Ophus (Ophus, 2019). There are other examples of 4D STEM applied to organic materials such as P3HT, PC61 BM (Mu et al., 2019), poly [2.5-bis(3-tetradecylthiophen-2-yl)thieno[3,2-b]thiophene] (PBTTT) (Panova et al., 2019) and other polymer blends (Donohue et al., 2022). Furthermore, the orientation  $\pi$ - $\pi$  stacking from two different molecular film systems was mapped using 4D-STEM, which provided an orientation map showing overlapping grains (Bustillo et al., 2021). The advantage of 4D STEM is that the entire diffraction pattern is acquired at each specimen position. This means that the variance can be calculated post-acquisition at any inner angle using a virtual annular detector. The method is therefore highly dose efficient, a key requirement for beam sensitive samples, such as organic thin-films. 4D STEM data were acquired on NiO (control sample) and organic TIPS pentacene thin-films at the University of Manchester, in collaboration with Dr Alex Eggeman. The results are presented in section (4.4). TIPS pentacene is widely used in organic electronics applications, since it has a regular  $\pi$ - $\pi$  stacking arrangement in the unit cell and good solubility in typical organic solvents (Chen et al., 2007). This is because the pentacene unit has two bulky TIPS side groups on either side of it. In principle, optimized  $\pi$ - $\pi$  stacking could improve charge carrier transport between individual acene units, thereby enhancing the overall electrical performance of organic molecular crystals (Anthony et al., 2002).

## 4.2 Experimental Method

### 4.2.1 Sample preparation

All the samples in this study are in thin-film form and are supported on a copper TEM grid for electron microscopy work. The NiO sample was commercially provided by Gatan UK as a test specimen for calibrating the EELS spectrometer. This sample was also used for calibrating the STEM probe convergence semi-angle and camera length of the TEM. The TIPS pentacene samples were prepared by Dr Kleitos Stavrou, Durham University. The TIPS pentacene thin-film was first deposited on a layer of poly(3,4-ethylenedioxythiophene) polystyrene sulfonate, also known as PEDOT:PSS. The extra layer of PEDOT:PSS is used because it is soluble in water, which enables us to release the TIPS pentacene layer and transfer it to a TEM grid as a free-standing film. PEDOT:PSS from Ossila was filtered in 0.45  $\mu\text{m}$  filter and was then diluted in isopropanol at a ratio of 1:1. The solution was then spin coated at 3000 rpm for 60 seconds onto a glass substrate and thermally annealed at 150°C for 15 minutes. The TIPS pentacene was purchased from Ossila and had a purity better than 99.9% as claimed by the manufacturer. TIPS pentacene was dissolved in chlorobenzene at two concentrations 5 and 20 mg/ml respectively. The solution was spin coated onto PEDOT:PSS/glass substrate using the 5 mg/ml solution at 2000 rpm for 60s, followed by thermally annealing at 100°C for 5 min at a pressure of 2000 mbar. The reason for the thermal annealing step is to improve the crystallinity of the TIPS pentacene. Drop cast TIP pentacene films were prepared using both 5 and 20 mg/ml concentrations. All spin coated and drop cast solutions were fabricated in a glove box under nitrogen atmosphere. Following deposition of the TIPS pentacene the glass substrates were immersed in de-ionised water. After a few minutes the PEDOT:PSS layer dissolved and the TIPS pentacene film floated to the surface. The film was then picked up with 250 mesh copper grids for examination in the TEM. Some folding of the TIPS penta-

cene layers occurred while transferring to the TEM grid, but only the thinner, unfolded regions were selected for analysis.

#### 4.2.2 Electron Microscopy

The NiO thin-film was examined in a JEOL JEM-2100F TEM operating at 200kV (Figure 4.1). The first step in this experiment is to find a clean area, where there are no deformities or folding of the film. The microscope was set up in STEM mode with a 5.3 mrad probe semi-convergence angle. The probe angle is smaller than the optimum angle  $\alpha_{opt}$  and is therefore diffraction limited (section 2.1.2). The annular dark field (ADF) detector inner angle was set by varying the camera length. The relation between the camera length and inner angle is inverse, with large camera length giving smaller inner angles for a fixed detector size.

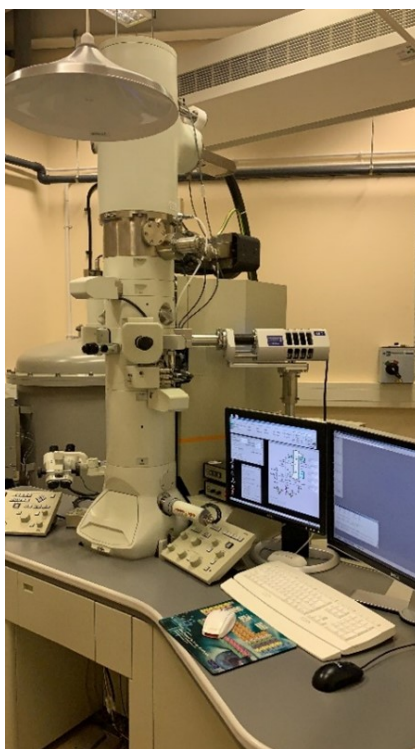


Figure 4.1: JEOL JEM-2100F TEM used for investigating NiO and TIPS pentacene thin-films.

In order to calibrate the STEM probe convergence angle and ADF detector inner angle the diffraction pattern from a NiO grain oriented along a zone-axis must first

be obtained. An example is shown in Figure 4.2, where the NiO grain is oriented along  $\langle 110 \rangle$  (Morishita et al., 2008), as determined by the angles between Bragg diffracted discs. NiO has a face centered cubic crystal structure with a lattice parameter of  $3.6 \text{ \AA}$  (section 4.3.1). The angle between the unscattered beam and a Bragg diffracted disc is  $2\theta_B$ , where  $\theta_B$  is the Bragg angle. Since  $\theta_B$  can be calculated using Bragg's law, the diffraction pattern can be calibrated and from that probe convergence angle and ADF detector inner angle readily measured. The ADF detector has an outer radius of 8 mm and an inner radius of 3 mm. The ADF outer angle can therefore be calculated using the following equation:

$$\alpha_{outer} = \text{outer radius of detector in (mm)} \times \frac{\text{inner angle (mrad)}}{\text{inner radius of detector in(mm)}} \quad (4.1)$$

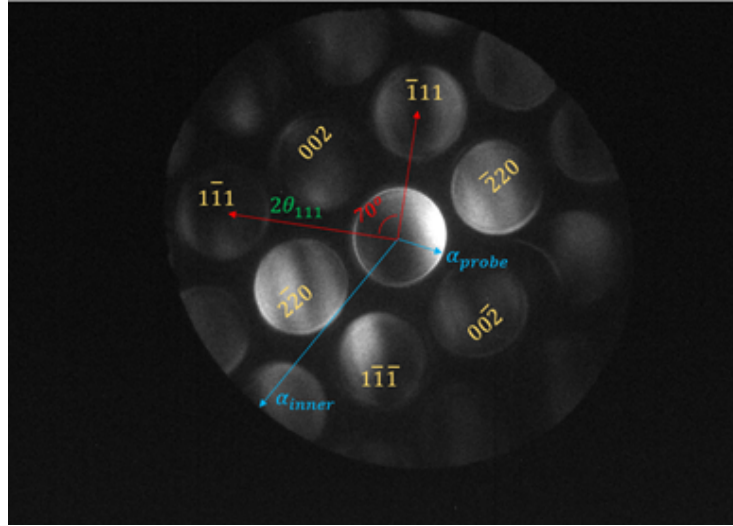


Figure 4.2: Electron diffraction pattern for a  $[110]$  NiO grain. The STEM probe semi-convergence angle  $\theta_{probe}$  is proportional to the unscattered beam radius, which can be calibrated using a known Bragg angle, such as  $\theta_{111}$ . Also shown in the figure is the inner angle  $\theta_{inner}$  for the ADF detector.

At each inner angle we acquired five bright field (BF) and dark field (DF) images from different regions of the specimen. BF images were used to check for suitability of the area for analysis (i.e. no film deformities etc). The DF images were used to calculate the intensity variance at a given ADF inner angle. To measure grain size ten centred dark field images were acquired with a tilted electron beam in TEM

mode. Digital Micrograph software was used to analyse image variance in STEM DF images as well as grain size analysis. 4D STEM data on the NiO thin-film were acquired by Dr Alex Eggeman at the University of Manchester using a Tecnai F30 field emission gun (FEG) TEM operating at 300 kV. An ASTAR (an automatic crystallographic indexing and orientation/ phase mapping tool developed for TEM) NanoMegas system was used for recording the diffraction pattern on the phosphor screen at each beam scan position using a CCD camera mounted outside the TEM viewing chamber. This detection geometry resulted in elongated diffraction patterns (Figure 4.3). The distortion was corrected and the intensity variance for the 4D STEM dataset calculated using a Python script provided by Dr Eggeman. NiO 4D STEM data was collected using different condenser aperture (50 and 100  $\mu\text{m}$ ) and beam spot sizes (spots size 1, 5 and 9). At spot size 1 and 5, the intensity of the unscattered beam was saturating and therefore this data was not analysed further.

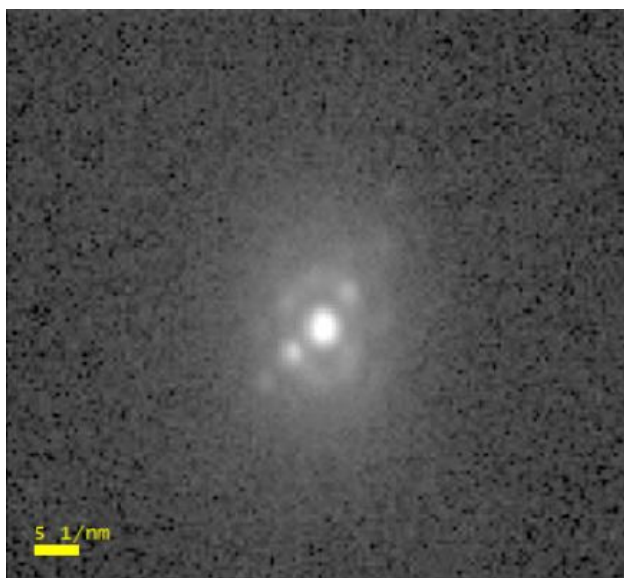


Figure 4.3: Example as-recorded diffraction pattern for NiO in 4D STEM. The figure is displayed on a square root intensity scale to highlight any weak scattering.

TIPS pentacene measurements were performed using a Talos Arctica cryo-TEM operated at 200 kV FEG in STEM mode, equipped with a NanoMegas. The data acquisition was at spot size 1, 5 and 9, 10 nm step size, 250 ms pixel dwell time,

camera length 7.1 cm and a 10  $\mu\text{m}$  C2 aperture, with a convergence semi-angle of 5 mrad. The diffraction patterns were recorded by Digital FluCam with a frame size of  $512 \times 512$  pixels. Virtual annular dark field (ADF) images were created via HyperSpy software on the 4D-STEM data by choosing a virtual detector that includes strong scattering reflections in the diffraction patterns; Figure (4.4).

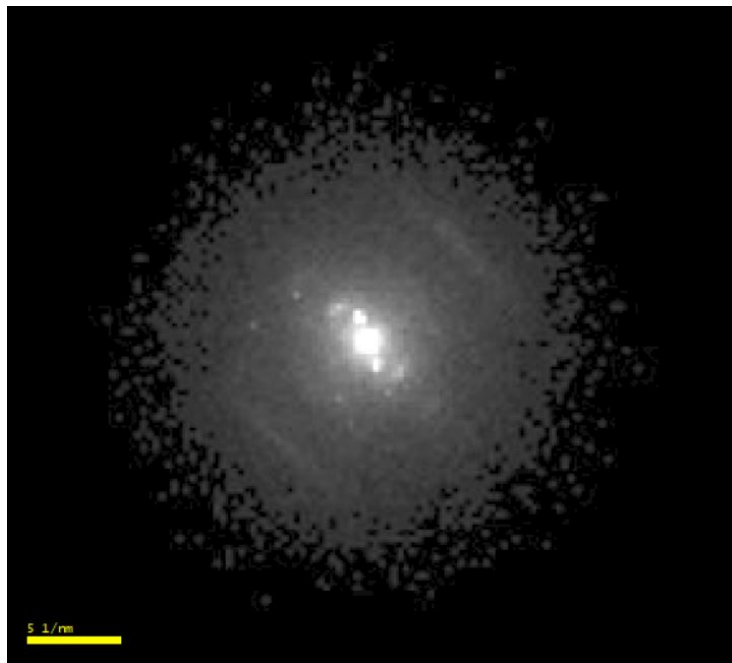


Figure 4.4: An example diffraction pattern of TIPS pentacene recorded by 4D-STEM, which shows faint streaks at high scattering angles. The figure is displayed on a square root intensity scale to highlight any weak scattering.

## 4.3 NiO experimental results

### 4.3.1 NiO thin-film characterisation

Figure 4.5 shows TEM bright field and dark field images of the NiO thin-film. The polycrystalline nature of the material is clearly visible; for example, the dark regions in the bright field image correspond to individual grains that are strongly Bragg diffracting, and similarly for bright regions in the dark field image.

Figure 4.6a shows the diffraction pattern acquired from the NiO thin-film. Since

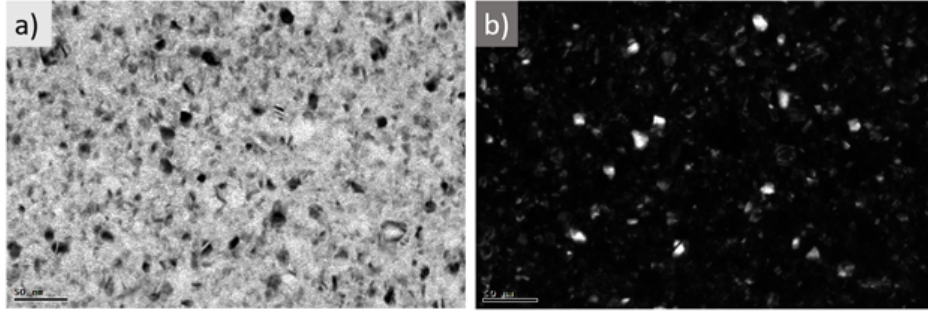


Figure 4.5: (a) Bright field and (b) dark field TEM images of NiO. The scale bar in each figure is 50 nm.

the film is polycrystalline each of the rings correspond to Bragg diffraction from a particular type of crystallographic plane. The crystal structure of NiO is face centred cubic (Sasaki et al., 1979) and therefore only reflections from crystal planes where the Miller indices are either all even or all odd (e.g. 111, 200 etc) are allowed. The Miller indices for each ring in the diffraction pattern are indicated in Figure 4.6a. From the diffraction pattern the lattice parameter ( $a_0$ ) can be extracted using the following formula valid for cubic crystals:

$$d_{hkl} = \frac{a_0}{\sqrt{h^2 + k^2 + l^2}} \quad (4.2)$$

From the above equation a graph of  $(1/d_{hkl})$  vs.  $\sqrt{h^2 + k^2 + l^2}$  is a straight line with gradient  $(1/a_0)$ . This graph is plotted in Figure 4.6b. From Figure 4.6b the lattice parameter for the NiO thin-film is 3.6 Å. This value is significantly smaller than the literature value of 4.2 Å (Sasaki et al., 1979). This may be due to the fact that the literature value was obtained from bulk samples, while our sample was a thin-film. The 3.6 Å lattice parameter for our material was used to calibrate the STEM probe and ADF detector angles as outlined in section 4.2.2.

### 4.3.2 Grain Size Analysis

DF images are very effective in showing the crystalline grain distributions on nanometer scale. These grains are selected randomly; 10 different grains from 10 different DF images are measured to get statistics from a total of 100 grains. We used

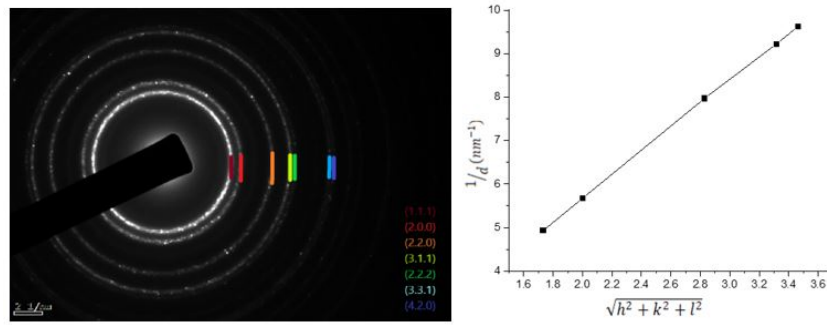


Figure 4.6: (a) Electron diffraction pattern of NiO. Miller indices for each of the rings is as indicated. (b) Plot of  $(1/d_{hkl})$  vs  $\sqrt{h^2 + k^2 + l^2}$ , where  $d_{hkl}$  is the interplanar spacing of the  $(hkl)$  crystallographic plane.

Digital micrograph (DM) proprietary software for grain size analysis. DM allows us to calculate the equivalent diameter (i.e. diameter of the circle that has the same area as the particle shape). Figure 4.7 shows a plot of grain size (diameter) vs frequency that was acquired from 100 grains, where the mean grain size is 10.8 nm and the standard deviation is 3.2 nm. The histogram shows a single peak (unimodal distribution), which is similar to the classical Gaussian type distribution, and is roughly symmetric.

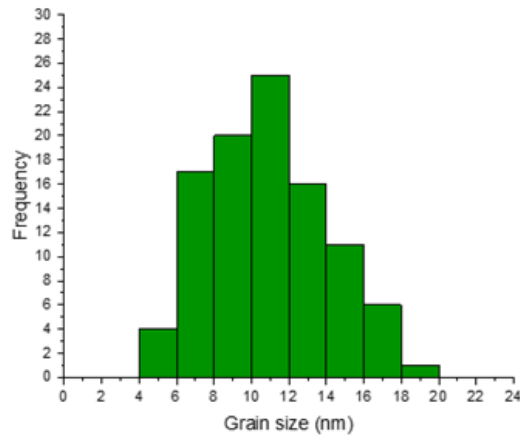


Figure 4.7: Histogram plot showing grain size data (diameter) for 100 grains.

### 4.3.3 STEM Fluctuation Electron Microscopy

As described in section 4.2.2 fluctuation electron microscopy in the STEM was performed by acquiring a series of dark field images at varying ADF detector inner angles. Figure 4.8 shows example STEM DF images acquired at inner angles of 6 and 45 mrad respectively. It is clear that the image intensity variance is much larger for the smaller inner angle of 6 mrad. This is due to the fact that smaller inner angles have larger coherence volumes leading to stronger Bragg diffraction (section 2.1.2).

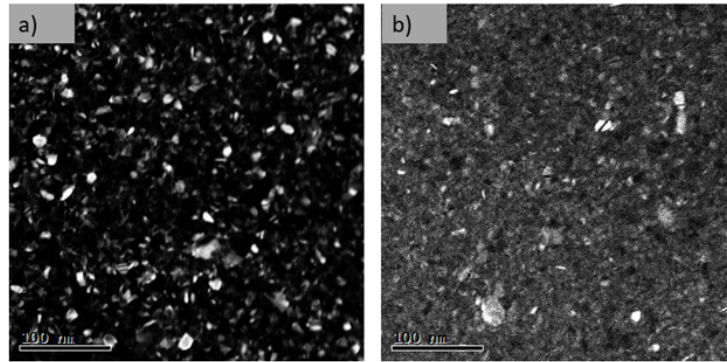


Figure 4.8: STEM DF images for NiO at a) the smallest inner angle of 6 mrad and b) the largest inner angle of 45 mrad. The scale bar is 100 nm.

Figure 4.9 shows the image intensity variance plotted as a function of ADF detector inner angle for NiO. For each image the intensity variance was calculated using Equation 2.13 in Section 2.5.1, and the values for 5 different images, all acquired at the same inner angle, was averaged and plotted in Figure 4.9.

In Figure 4.9, when we move from large inner angle to low inner angle, the variance starts to increase at inner angle 25 mrad before suddenly decreasing instead of reaching a plateau, as expected from the ideal plot in Figure 2.20, section 2.5.2. The average grain size is 10.8 nm (section 4.3.2) while the Airy disc diameter of the STEM probe is 0.6 nm, as calculated using the equation for a diffraction limited probe (section 2.1.2, 4.3.1). Since the Airy disc is much smaller than the grain size, the plateau in the ideal variance plot should have been observed. A potential artefact in the measurements is however the fact that we are using an

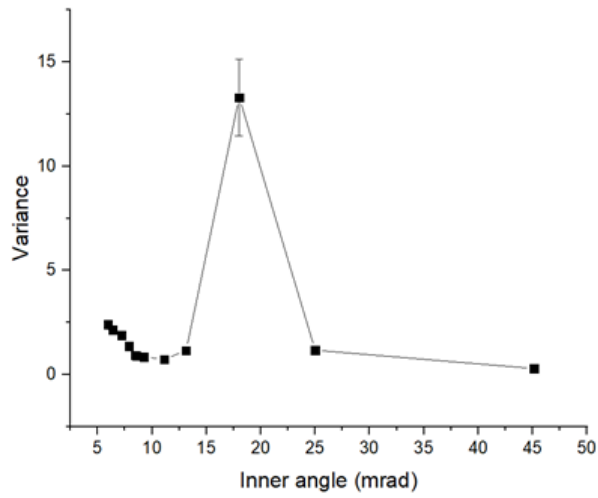


Figure 4.9: Intensity variance as function of inner angle for the NiO thin-film sample. For all data points other than 18 mrad the error bar is smaller than the data point marker.

ADF detector of fixed physical dimensions, which means that the detector outer angle will depend on the inner angle. Figure 4.10 shows a plot of ADF detector outer angle vs inner angle, indicating that the outer angle decreases monotonically with decreasing inner angle. Therefore, at small inner angles many of the higher order Bragg diffracted beams will lie outside the ADF detector range. It is assumed that this may be the cause of the variance decrease at small inner angle, since the ideal curve in Figure 2.20, section 2.5.2 effectively assumes an ADF detector of infinite outer angle.

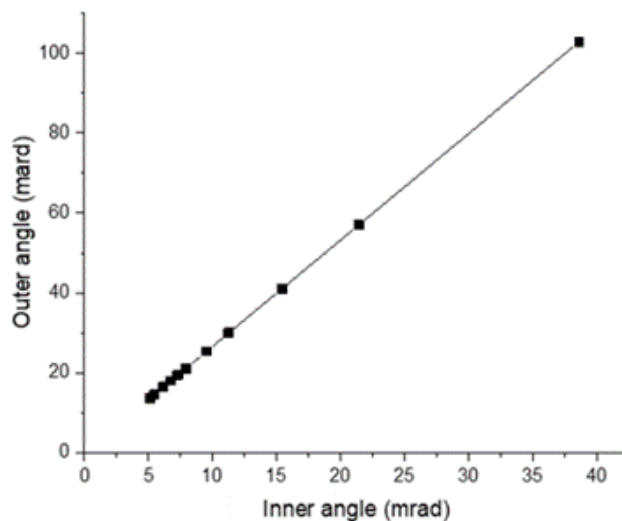


Figure 4.10: Variation of ADF detector outer angle as a function of inner angle for a JEOL JEM-2100F TEM.

#### 4.3.4 4D STEM

As mentioned in section 4.1, 4D STEM has been used to obtain the diffraction pattern and intensity variance of virtual dark-field images for different spot size numbers (i.e. first condenser lens excitation) and second condenser aperture sizes. Hyperspy was used to analyse the diffraction patterns and obtain dark-field images using a virtual aperture. The two smallest spot size numbers (spot size 1 and 5) produced strong saturation around the unscattered beam, making the data unusable. Therefore, results are only presented for the low intensity spot size 9 at two different condenser aperture sizes (C2-1 and C2-3). The diffraction pattern for spot size 9, C2-1 was saturating in the middle (Figure 4.11), although the Bragg peaks are clearly visible and not saturating the detector. Therefore, only the region outside the unscattered beam disk was used for calculating the variance. For spot size 9 and smaller C2-3 aperture there was no saturation of the unscattered beam (see Figure 4.3 for an example diffraction pattern).

Bright and dark-field images from suitable areas of the diffraction pattern were generated using virtual apertures (Figure 4.11). Bright-field and example dark-field images for spot size 9, C2-1 and C2-3 apertures are shown in Figures 4.12 and 4.13

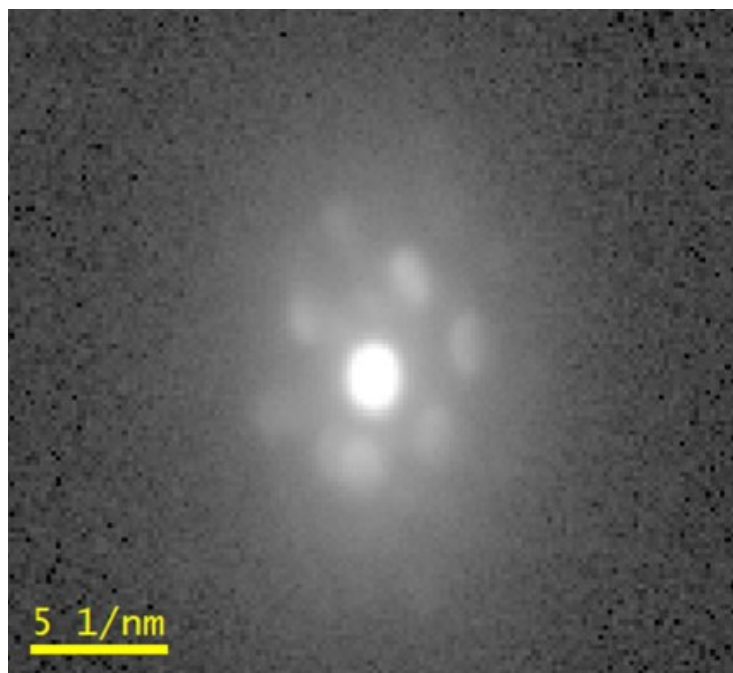


Figure 4.11: 4D STEM electron diffraction pattern for NiO acquired at spot size 9 and aperture C2-1. The red and yellow circles represent virtual apertures for generating bright-field and dark-field images. The figure is displayed on a square root intensity scale to highlight any weak scattering.

respectively. A square area of dimension 483 nm was scanned in a grid of  $200 \times 200$  pixels. This gives a total of 40,000 data points for calculating the intensity variance, which is a much larger sampling than previous variance calculations Voyles and Muller (2002), so that random errors are minimised. It is clear that for both C2 aperture sizes individual NiO grains have been resolved. In particular, the 4D STEM virtual bright-field and dark-field images appear similar to TEM images (Figure 4.5), due to reciprocity of the two imaging modes. Furthermore, in the bright-field image of Figure 4.13 there is evidence of a thickness variation in the NiO film either side of the annotated dash line. The region below the dash line is appearing darker and must therefore be a folded area with larger thickness (the NiO film was unfortunately damaged during handling). The larger thickness of the folded area is expected to decrease the intensity variance compared to the thinner regions of the sample (Yi and Voyles, 2011; Hwang and Voyles, 2011),

Using a Python script from Dr. Alex Eggeman, the intensity variance was com-

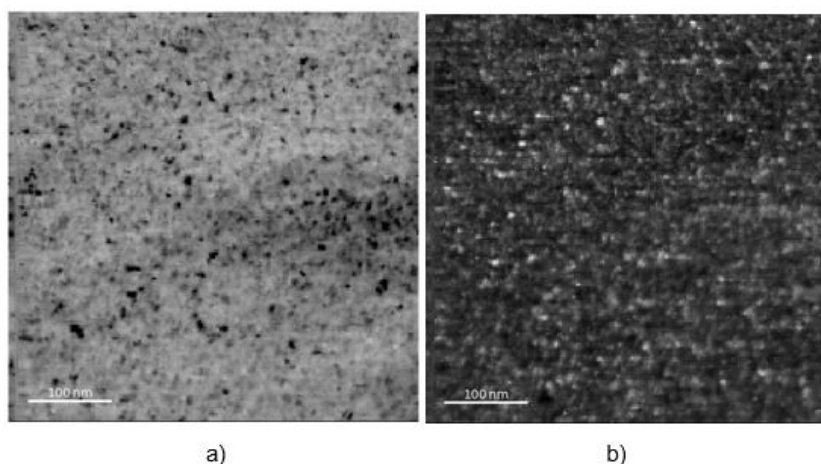


Figure 4.12: NiO 4D STEM virtual a) bright-field and b) dark-field images for C2-1 aperture. The scale bar is 100 nm and the sampling is 200 x 200 pixels.

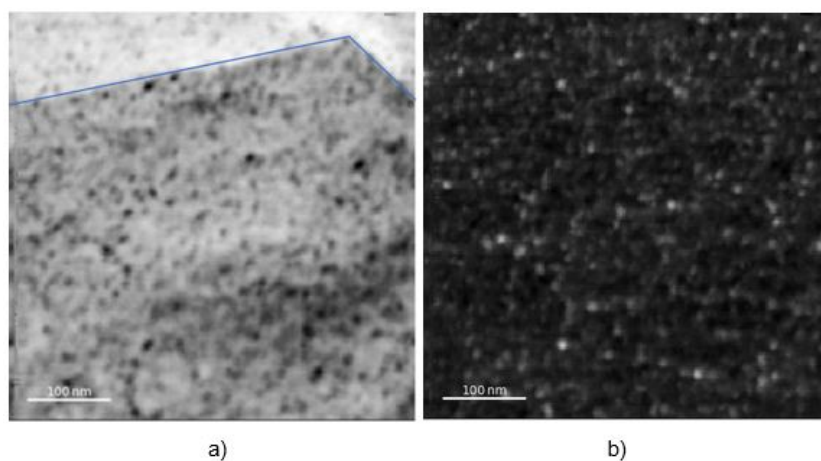


Figure 4.13: NiO 4D STEM virtual a) bright-field and b) dark-field images for C2-3 aperture. The scale bar is 100 nm and the sampling is 200 x 200 pixels.

puted for a range of virtual detector inner angles for a given condenser aperture setting. The inner angle was calibrated using the NiO diffraction pattern in Figure 4.11, following the procedure described in sub-section 4.2.2. The results are shown in Figure 4.14. The variance increased for the smaller condenser aperture size. In both cases the variance decreased monotonically with inner angle.

In a typical TEM there are (at least) two condenser lenses. The first condenser lens (C1) is used to control the spot size, with increasing spot size numbers resulting in a stronger C1 lens current and higher electron source demagnification. This means selecting electrons from a smaller area of the gun filament source with improved

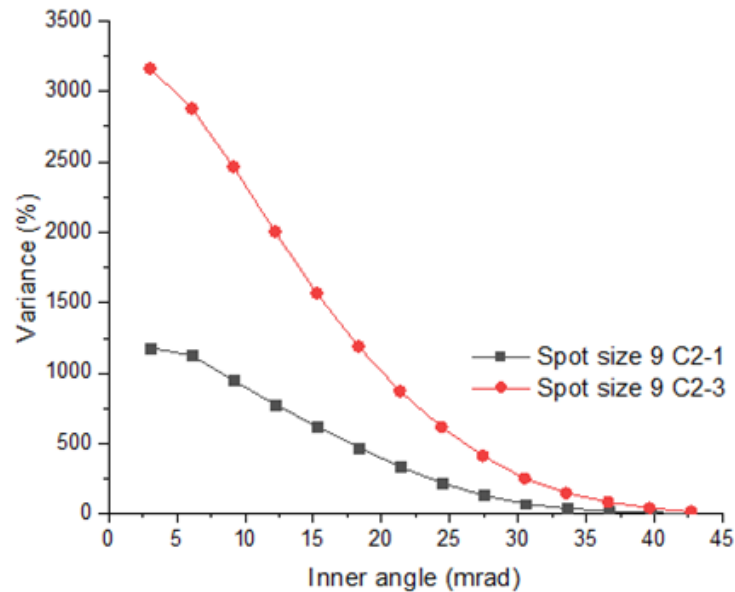


Figure 4.14: 4D STEM dark-field intensity variance as function of virtual detector inner angle for the NiO thin-film sample.

coherence. Because the electron spot size determines the beam coherence we expect the variance to increase. The second condenser lens (C2) is used to expand and collapse the beam on the specimen plane and has an aperture underneath. The aperture controls the solid angle of the probe. The C2 condenser aperture should therefore also affect the variance, with a larger condenser aperture leading to a higher solid angle and therefore more incoherence. Li et al. (Li et al., 2014) and Yi et al. (Yi et al., 2010) have previously shown that the variance depends on beam coherence. The results in Figure 4.14 are also consistent with coherence affecting the variance. Because a part of the NiO film in the C2-3 measurement has been folded (see Figure 4.13), we would expect the variance to decrease due to multiple scattering of the electron beam through the thicker sample. However, this decrease in variance is counteracted by the higher coherence of the smaller C2 aperture. If there is no folding the variance increase would be even larger. Unlike Figure 2.20 section (2.5.2), Figure 4.14 does not show a significant plateau region, because the probe size is smaller than the 10.8 nm average grain size of the NiO thin film (section 4.3.2). This is confirmed by forming a virtual bright-field image from the

4D STEM data set (Figures 4.12 and 4.13), where it is clear that the NiO grains are clearly resolved. As discussed in sections 2.5.1 and 2.5.2 the coherence volume increases with smaller inner angle, with the plateau onset region being when the coherence volume is equal in size to the paracrystalline domain size. Since the NiO crystalline grains are larger than the beam size, the plateau region is not observed.

## 4.4 TIPS pentacene experimental results

### 4.4.1 TIPS pentacene characterisation

A combination of drop-cast and spin-coating methods were used to produce uniform TIPS pentacene films. TIPS pentacene has a triclinic crystal structure with unit cell parameters  $a=7.565 \text{ \AA}$ ,  $b=7.750 \text{ \AA}$ ,  $c=16.835 \text{ \AA}$ ,  $\alpha=89.15^\circ$ ,  $\beta=78.42^\circ$  and  $\gamma=83.63^\circ$  (Anthony et al., 2001). The TIPS pentacene molecule is contained in a linear channel that is formed by the enmeshed isopropylsilyl side chains and cofacial stacking (Figure 4.15).

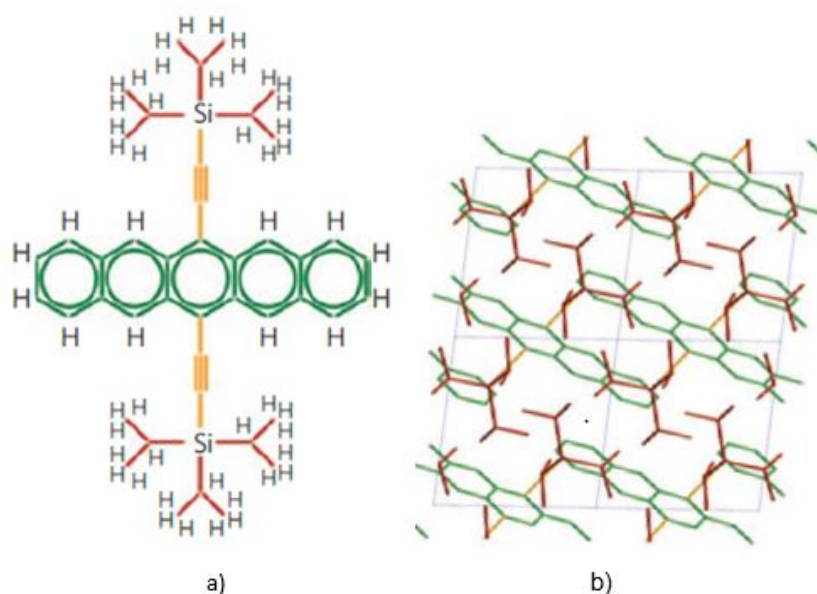


Figure 4.15: (a) Schematic structure of the TIPS-pentacene molecule showing the conjugated  $\pi$ -electron density on the TIPS pentacene. (b) Assembly of TIPS pentacene molecules in a triclinic crystal structure; (Eggeman et al., 2013).

Figure 4.16 shows a typical bright-field TEM image of a drop cast TIPS pentacene thin film. The dynamical scattering bend contours are clearly visible. These bend contours are observed in a crystal sample which is locally deformed or bent. The orientation of a crystal plane with respect to incident beam will then depend on spatial location. Thus, some bent regions will be in the Bragg orientation, giving rise to strong scattering and lower intensity in a bright-field image (Williams and Carter, 2009). As we move away from this region, we are no longer in Bragg and therefore lose the strong diffraction conditions. The presence of continuous bend contours over large regions of the sample, indicates the drop cast TIPS pentacene is well crystallised with micrometer sized grains.

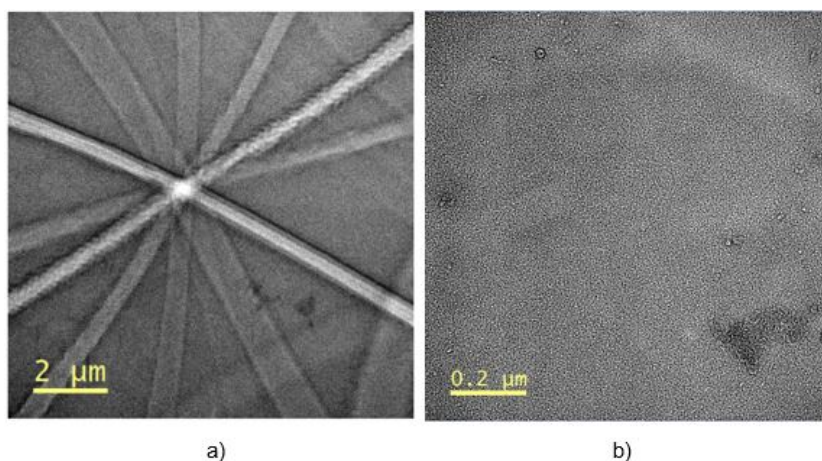


Figure 4.16: TEM image of a) drop cast and b) spin coating TIPS pentacene. The scale bar is 2  $\mu\text{m}$  for drop casting and 0.2  $\mu\text{m}$  for the spin coating image.

A bright-field TEM image of a spin coating TIPS pentacene thin film is shown in Figure 4.16b with no visibility of bend contours. During acquiring data from spin coating TIPS pentacene, the TIPS pentacene is damaging very fast, which affects the crystallinity. Thus, most papers are reporting high crystallinity TIPS pentacene fabricated with drop-casting (Raghuwanshi et al., 2016, 2018; Shih and Akinwande, 2018). The drop casting method is more suitable for small-area deposition, plus it is a simple process and gives a high crystallinity. On the other hand, when using spin casting, there are two reasons that can influence the crystallinity and mobility, which are the deposition location on the substrate (on or off center) (Bharti and

Tiwari, 2015) and the spin rotational speed (Yunus et al., 2022).

#### 4.4.2 4D STEM

4D STEM measurements on the TIPS pentacene films were performed by Dr Alex Eggeman at the University of Manchester. The 200 kV Talos cryo-TEM is ideal for investigating beam sensitive materials, such as the TIPS pentacene films in this study (see Section 4.2.2 for experimental details). In particular, a direct electron detector with higher detector quantum efficiency enables the use of low electron beam currents, which reduces the beam damage. We first present 4D STEM results for the drop cast sample, followed by the spin coated film. An example diffraction pattern acquired from a 4D STEM data set for the drop cast TIPS pentacene film is shown in Figure 4.17a. Apart from sharp Bragg reflections due to the sample being crystalline, there are also streaks of diffuse intensity approximately parallel to the 120 Bragg reflection (Figure 4.17a). The diffraction pattern is similar to that reported in Eggeman et al. (2013) for drop cast TIPS pentacene in the [001] orientation Figure 4.17b.

The presence of diffuse scattering is due to molecular disorder within the pentacene crystal (Eggeman et al., 2013). The diffuse streaks observed are consistent with a linear displacement along the pentacene long axis, because the pentacene fragment long axis is approximately parallel to [210], and the diffuse streaks are normal to this direction. Any reflection whose structure factor is affected by the displacement vector will show the streaks, while reflections that only depend on the undistorted atomic coordinates of the structure will show no streaking (the latter includes the sharp Bragg reflections in Figure 4.17a and 4.17b). The relationship between the molecular disorder and streaking is further illustrated in Figure 4.17c and 4.17d.

The 4D STEM data set can be calibrated using the diffraction pattern. The  $d$ -spacing for triclinic TIPS pentacene is given by the following formula:

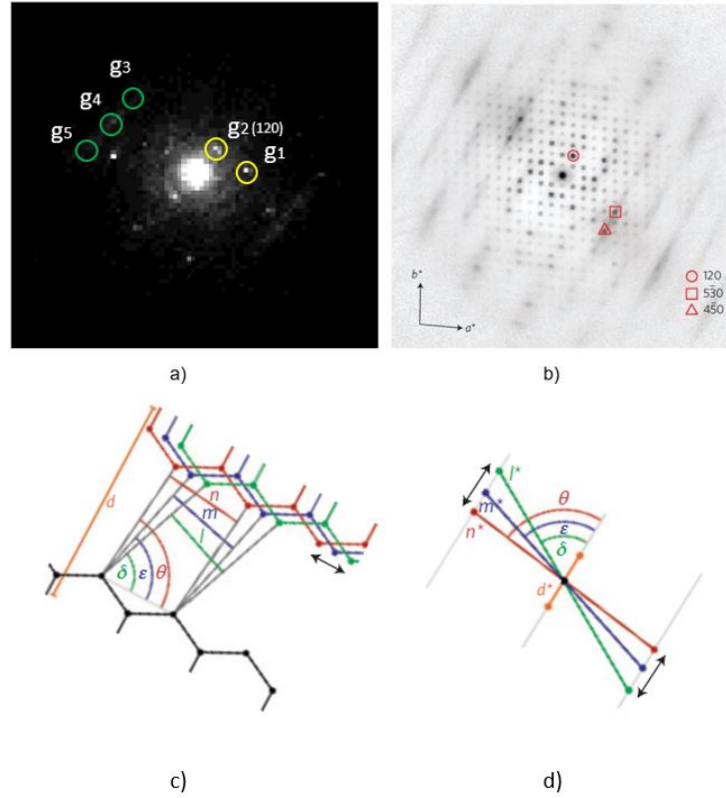


Figure 4.17: a) Example 4D STEM electron diffraction pattern for drop cast TIPS pentacene. The yellow circles represent virtual apertures for generating Bragg reflection dark-field images. The green circles represent virtual apertures for the diffuse intensity streaks. b) The diffraction pattern for drop cast TIPS pentacene in the [001] orientation reported in (Eggeman et al., 2013). Origin of streaking in TIPS pentacene shows c) displacements along the long axis of the pentacene molecule creates a range of interplanar angles ( $\delta$ ,  $\epsilon$ ,  $\theta$ ) and interplanar distances ( $l$ ,  $m$ ,  $n$ ) and d) in reciprocal space this gives rise to a diffuse scattered streak. c) The diffraction pattern for drop cast TIPS pentacene in the [001] orientation reported in (Eggeman et al., 2013).

$$\frac{1}{d^2} = \frac{1}{V^2}(S_{11}h^2 + S_{22}k^2 + S_{33}l^2 + 2S_{12}hk + 2S_{23}kl + 2S_{13}hl) \quad (4.3)$$

where  $V$  is volume of the unit cell.  $S_{11}=b^2c^2\sin^2\alpha$ ,  $S_{22}=a^2c^2\sin^2\beta$ ,  $S_{33}=a^2b^2\sin^2\gamma$ ,  $S_{12}=abc^2(\cos\alpha\cos\beta-\cos\gamma)$ ,  $S_{23}=a^2bc(\cos\beta\cos\gamma-\cos\alpha)$  and  $S_{13}=ab^2c(\cos\gamma\cos\alpha-\cos\beta)$ . The lattice parameters were obtained from (Eggeman et al., 2013) and the 120 Bragg reflection was used for the calibration. Using Equation 4.3 the pixel dimensions in 4D STEM can be expressed in reciprocal space or alternatively in mrad scattering angle by multiplying by the electron wavelength at 200 kV. The micro-

structure of the drop cast TIPS pentacene film can be investigated using 4DSTEM dark-field imaging. Virtual apertures around a Bragg peak ( $g_1$ ) and 120 reflection ( $g_2$ ) taken from Figure 4.17a were used to generate dark-field images from the 4D STEM data set, as shown in Figure 4.18. The  $g_1$  reflection (Figure 4.18a) shows a bend contour in the form of a bright band in the image, while  $g_2$  (Figure 4.18b) does not show a strong bend contour, indicating that the sample is more uniformly diffracting. This means that the sample bending is predominantly in a direction parallel to the 120 planes (note that the  $g_1$  reflection has a component orthogonal to  $g_2$ ; Figure 4.17a). The 120 reflections are along the pentacene molecule stacking direction, which makes bending along this direction very small.

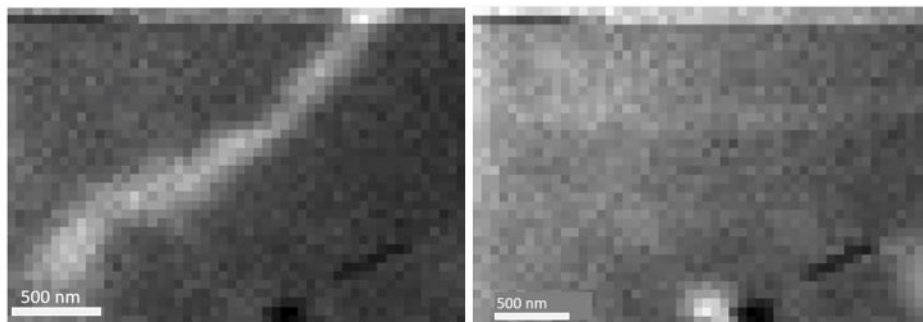


Figure 4.18: TIPS pentacene dark field images generated via 4D STEM virtual apertures positioned on a)  $g_1$  and b)  $g_2$  reflections in Figure 4.17a.

The diffuse scattering was investigated by placing the virtual aperture along different parts of the streak; for example, apertures  $g_3$ ,  $g_4$  and  $g_5$  in Figure 4.17a. The corresponding dark-field images are shown in Figure 4.19. Some parts of the streak ( $g_4$  and  $g_5$ ) give rise to strong localised diffraction, while other parts ( $g_3$ ) are more uniform. Furthermore, there is no obvious correlation between the streak dark-field images, and dark-field images for the 120 reflection, which is parallel to the streak direction. The different dark-field image intensities along the same streak suggests that in different parts of the thin film there are different degrees of TIPS pentacene molecule shifting (Figure 4.17d). The molecular disorder is therefore non-uniform through the structure, and shows a lot of variation.

Figure 4.20a is an example diffraction pattern from the spin coated TIPS penta-

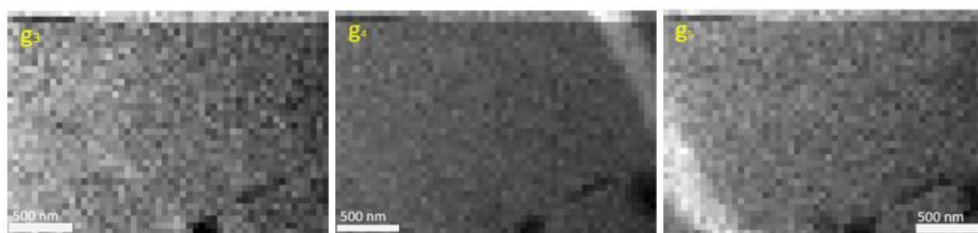


Figure 4.19: TIPS pentacene dark field images of the diffuse streak, generated using the virtual  $g_3$ ,  $g_4$  and  $g_5$  in Figure 4.15.

cene film acquired from a 4D STEM data set. There were sharp Bragg reflections around the unscattered beam, which indicates that there is some crystallinity in this sample. However, the diffraction pattern did not show strong streaks at high scattering angles similar to drop cast TIPS pentacene. A dark field image is acquired via a virtual aperture placed around the circled reflection in Figure 4.20a, where small grains are clearly seen in Figure 4.20b.

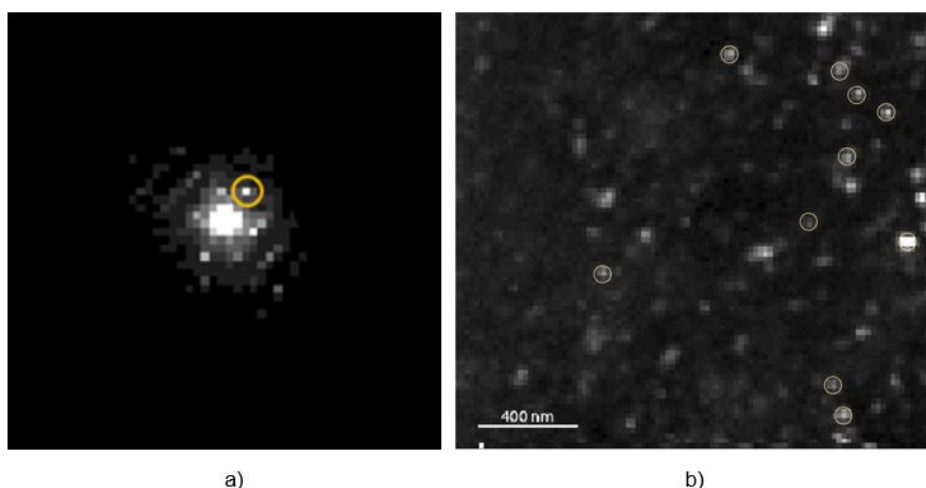


Figure 4.20: a) Diffraction pattern of spin coated TIPS pentacene, where the sample is crystalline and shows sharp Bragg reflections. The circled reflection is used to generate the virtual dark field image in b). The circled grains in b) are used to calculate the grain size

Using Digital micrograph (DM) software, the grains size has been analysed. The equivalent diameter (i.e. diameter of the circle that has the same area as the particle shape) of 10 grains has been measured. The average grain diameter for spin coating TIPS pentacene is  $58.7 \pm 10$  nm. Yoo et al (Yoo et al., 2015) calculated a coherence length for spin coated TIPS pentacene crystalline domains between 39.8 nm and

63.7 nm, using grazing incidence wide angle X-ray scattering (GIWAXS). Grieco et al (Grieco et al., 2016) obtained a domain size of  $23\pm 3$  nm for spin coated and  $40\pm 10$  nm for spin coated and solvent annealed TIPS pentacene, using Scherrer analysis of X-ray diffraction peaks. These domain sizes are similar to our results. Note that the small grain sizes, as well as rapid electron beam damage to the sample, meant that the crystallinity was not evident in the TEM bright-field image shown in Figure 4.16b. Only by using low electron doses and a direct electron detector could the crystallinity be observed.

### 4.4.3 Variance plots

The 4D STEM data set can also be used to generate variance plots. There were 1872 and 8,811 data points (i.e.  $52 \times 36$  and  $99 \times 89$  pixel scans) for the drop cast and spin coated sample data sets used for calculating the intensity variance, which minimises any random errors. Figure 4.21 shows the variance as function of inner angle for the drop cast sample, acquired with a spot size number 5 electron beam. The inner angle was calibrated using the 120 reflection in the TIPS pentacene diffraction pattern (Figure 4.17a), following the procedure described previously for NiO (sub-section 4.2.2). The variance drops monotonically to zero by 20 mrad, which is a faster decrease than NiO (Figure 4.14), where the variance extended to at least 30 mrad. This difference is due to the higher atomic number of NiO, whereas pentacene is mainly carbon based, and therefore only scatters to low angle. Furthermore, no plateauing of the variance is observed for small inner angles. This is because the drop cast TIPS pentacene sample is so well crystalline, with even the molecular disorder represented by the diffraction pattern streaking giving rise to uniform scattering over large areas of the sample (Figure 4.19). The paracrystalline domain size is therefore likely to be much larger than the electron beam size, and hence no plateauing of the variance is observed.

Figure 4.22 shows the variance as a function of inner angle for spin coated TIPS pentacene, acquired with a spot size number 9 electron beam. The variance drops

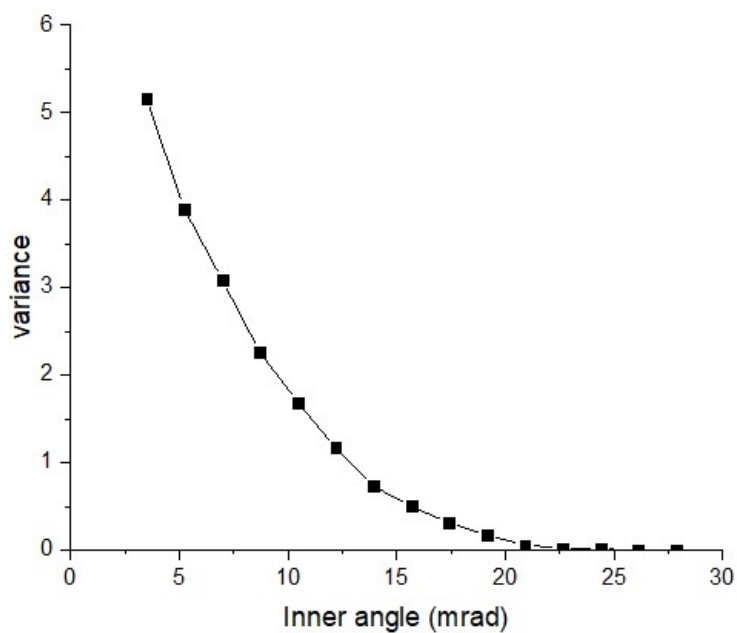


Figure 4.21: 4D STEM dark-field intensity variance as function of virtual detector inner angle for drop cast TIPS pentacene thin-film sample.

to zero at 16 mrad, far more rapidly than the drop cast sample. The spin coated variance is also orders of magnitude smaller than drop casting, despite the fact that the former used an electron beam with larger spot size number and therefore higher beam coherence. This suggests that with the spin coating, even with domains that are diffracting, there is a possibility of large amounts of para-crystallinity. The exact nature of the para-crystallinity is not clear, but since no diffuse streak intensity is observed in the diffraction pattern (Figure 4.20a), the para-crystallinity is expected to be different to the pentacene molecule shifting reported for large grain, highly crystalline TIPS pentacene (Figure 4.15).

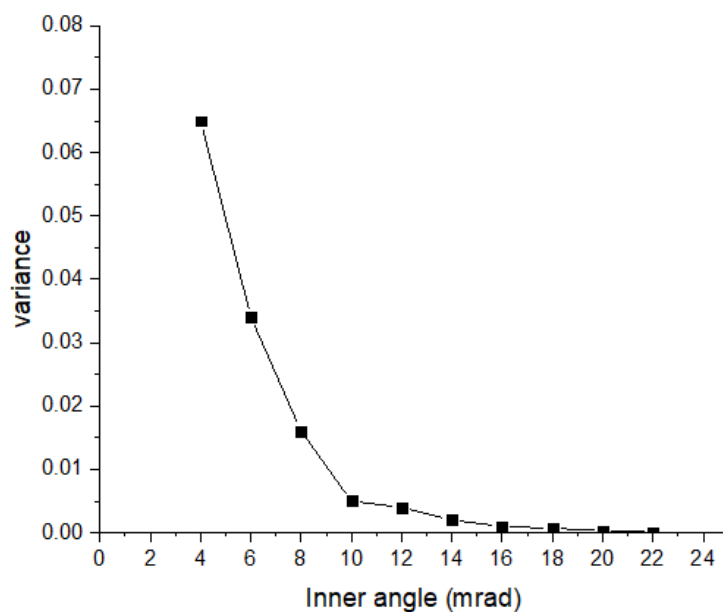


Figure 4.22: 4D STEM dark-field intensity variance as function of virtual detector inner angle for spin coated TIPS pentacene thin-film sample. Spot size number 9.

## 4.5 Conclusions

NiO was used as a test sample for the development of a conventional STEM and 4D STEM based fluctuation electron microscopy technique, that can potentially be used to investigate the nanoscale morphology of conjugated polymer and small molecules. We characterised the NiO sample, which has a FCC crystal structure with lattice parameter 3.6 Å and average grain size of 10.7 nm. Variance plots were constructed by analysing STEM DF images acquired at different ADF detector inner angles. The variance plots were found to be limited by the finite outer collection angle of the ADF detector at smaller inner angles. This can however be overcome by acquiring a 4D STEM data set and using virtual detectors to construct the variance plot. A small molecule TIPS pentacene sample prepared by both drop casting and spin coating has also been investigated. Using a conventional TEM at 200 kV we found that electron beam damage placed significant limitations on the information (e.g. diffraction patterns) that could be extracted. However, we found that beam damage can be minimised on a 200 kV Talos cryogenic transmission

electron microscope (cryo-TEM) with direct electron detector. Reliable 4D STEM data was obtained from the TIPS pentacene samples using this microscope. The diffraction pattern for the drop cast sample is similar to previous reports in the literature. In particular, large grain size of the order of several micrometers and diffuse streaking due to shifting of the pentacene molecule is observed. Virtual dark-field images acquired from different parts of the streak showed that the molecular disorder was non-uniform throughout the sample. The spin coated sample also showed Bragg reflections, and virtual dark-field images revealed grains with an average size of 58.7 nm. However, there is no indication of diffuse streaking in the spin coated sample. Variance plots acquired from the same 4D STEM datasets suggest that the spin coated sample has a larger amount of para-crystallinity within the grains than the drop cast sample. The disorder in the two systems are therefore very different in nature. For drop casting large grain sizes of the order of several micrometers is observed, with diffuse streaking due to pentacene molecular stacking disorder. For spin coating the grain size is considerably smaller (60 nm), with para-crystallinity within the grains, but no molecular stacking disorder. It is not immediately clear which morphology would produce better organic electronic devices, although in each case there is scope to improve the crystallinity further.

---

# EELS spectroscopy

## 5.1 Motivation

In the previous chapter, TEM and STEM analysis techniques, applied to NiO and TIPS pentacene samples have been shown. These techniques give information about the internal structure of a specimen using dark field images and diffraction patterns, including variance curves. In this chapter, we will apply the technique of electron energy loss spectroscopy (EELS) to determine the orientation of  $\pi$ -stacking in certain organic materials. As shown in Figure 5.1 there are three types of benzene dimer molecular  $\pi$ -stacking between two aromatic rings (Wheeler, 2011); face-to-face (i.e.co-facial), parallel-displaced, and edge-to-face. The edge-to-face for benzene dimer was found to be more stable than face-to-face and parallel-displaced (Janiak, 2000). Therefore, referring to different packing geometries,  $\pi$ -stacking of conjugated small molecules in crystals is divided into four types, which are shown in Figure 5.2 (Yao et al., 2018).

The face-to-face arrangements within columns and the edge-to-face arrangements between columns are the most recognisable characteristics of the herringbone stacking mode, which pentacene molecular structure is an example (Yao et al., 2018). (Sherman et al., 2015) state that single crystals of benzene feature herringbone packing, while the edge-to-face generally is desired for high -performance polymer

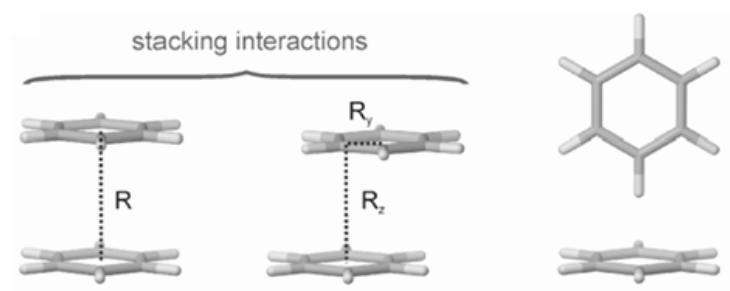


Figure 5.1: Three structures of the benzene/benzene intermolecular stacking; a) face-to-face, b) parallel-displaced and c) edge-to-face (Wheeler, 2011).

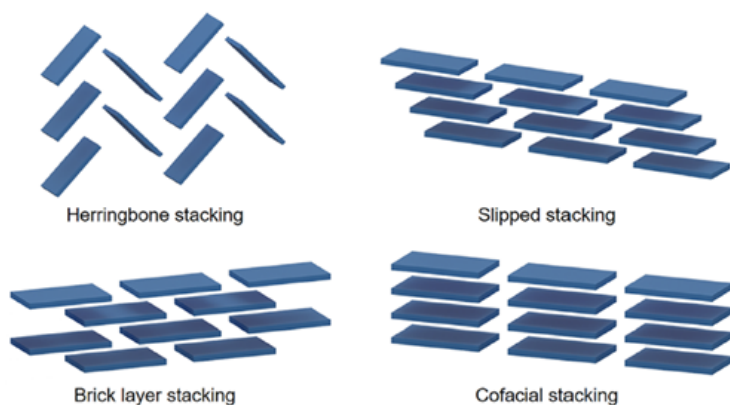


Figure 5.2: The four categories of  $\pi$ -stacking in conjugated small molecules: herringbone, slipped, brick layer and cofacial stacking (Yao et al., 2018).

transistor (Li et al., 2016). Unlike herringbone stacking, the cofacial stacking type is one by one stacking, with small displacement in their conjugated molecules, a typical example being TIPS pentacene. Because of the bulky side group present in a TIPS pentacene molecule (Figure 4.15), the edge-to-face herringbone conformation is changed into a face-to-face configuration (Pitsalidis et al., 2014). In the literature grazing incident wide-angle X-ray (GIWAXS) has been used to characterise the molecular packing in organic thin films. The GIWAXS crystallographic method can be used to learn more about the structural details of the deposited thin films, such as the interlayer stacking distances, the long-range crystalline order, and the orientation of the polymer as well small molecules. (Zhang et al., 2016) found using GIWAXS measurement that 2DQTT-o-B material exhibits face-to-face packing similar to TIPS pentacene, while a herringbone structure with layers of molecules that are oriented edge-to-face similar to pentacene was observed for

2DQTT-o-L. (Sherman et al., 2015) used GIWAXS to show that thin films of TIPS pentacene exhibit preferred orientation in the out-of-plane direction, with the (001) planes parallel to the substrate. Another technique, X-ray absorption near edge spectroscopy (XANES), can also provide information about molecular orientation. (Rivnay et al., 2012) probed P3HT films by XANES at different incident angles and showed more preferred edge-on orientation. XANES is often used on carbon-based materials (Salleo et al., 2010), due to the rich fine structure of the carbon K-absorption edge. Because GIWAXS and XANES measures a large area of the sample, techniques with higher spatial resolution are required. For example, the orientation of the molecules may change due to disorder within the thin film, at grain boundaries or close to interfaces. The molecular orientation with respect to the film has an important effect on the charge transport, in devices such as organic field effect transistors, light emitting diodes or photovoltaics. The carbon K-edge fine structure in EELS shows anisotropy effects in materials with  $sp^2$  bonding (Section 2.5.3). EELS fine structure analysis has previously been applied to polymers (Pal et al., 2017; Varlot et al., 1999; Pal et al., 2021) and carbon nanotubes (Wepasnick et al., 2010; Yase et al., 1996). In this chapter the suitability of EELS to probe molecular stacking orientation in organic thin films at high spatial resolution is evaluated.

## 5.2 Anisotropy in carbon K-edge

In this section changes to the EELS carbon K-edge fine structure as a result of orientation will be quantified. In particular, an analysis of the  $\pi^*$  to  $\sigma^*$  ratio in the carbon K-edge can be used to distinguish between face-to-face and edge-to-face molecular orientations. For this purpose, we use a natural graphite sample as a calibration test specimen. The reason for choosing natural graphite is because it is highly ordered and relatively beam stable. EELS carbon K-edges are acquired at different specimen tilts, using a high tilt tomography holder, that can achieve

much larger tilts (up to 60° tilt) compared to conventional TEM holders. The  $\pi^*$  to  $\sigma^*$  ratio is calculated at each specimen tilt. Results are acquired in both parallel beam TEM and focussed beam STEM illumination conditions. The former is easier to interpret, since there is only one orientation of the beam with respect to the graphite sample. On the other hand for STEM there are different beam directions within the STEM probe which complicate interpretation of the data. Nevertheless, the STEM technique is essential for spatial mapping of molecular disorder within a thin film. By comparing the local  $\pi^*$  to  $\sigma^*$  ratio obtained from spatial STEM EELS mapping to the calibration data obtained from the graphite test specimen, we can deduce information about the molecular orientation in a thin film, such as TIPS pentacene.

A commercial natural graphite sample (Alfa Aesar, 99.9% purity) was provided by Dr Michael Hunt, Durham university. The graphite flakes were crushed and deposited on a holey carbon TEM grid. A TEM image of the graphite flake used for EELS analysis is shown in Figure 5.3. EELS acquisition was performed on a thin area of the flake suspended over vacuum (circled regions in Figure 5.3), to avoid any contribution from the holey carbon support. For accurate analysis, it is important that the flake thickness does not change significantly upon tilting, since multiple inelastic scattering can change the shape of the carbon K-edge. Figure 5.3a shows the graphite flake at 0° specimen tilt, while Figure 5.3b shows the same area at the maximum specimen tilt angle of 60°. The specimen appears slightly darker upon tilting, although the thickness is still reasonable for EELS.

After selecting a suitable area in graphite, EELS was used to acquire the zero-loss peak and carbon K-edge peak at specimen tilts from 0° to 60° in step sizes of 5°. We first present results for parallel beam TEM. EELS data were acquired in image mode with a 5.3 mrad radius objective aperture. The zero-loss peak was used to calculate the thickness of the sample, in units of the inelastic mean free path  $\lambda$ , i.e. the average distance that the electron beams travels before undergoing an energy loss scattering event. The thickness at 0° and 60° specimen tilt was  $0.4\lambda$  and  $0.7\lambda$

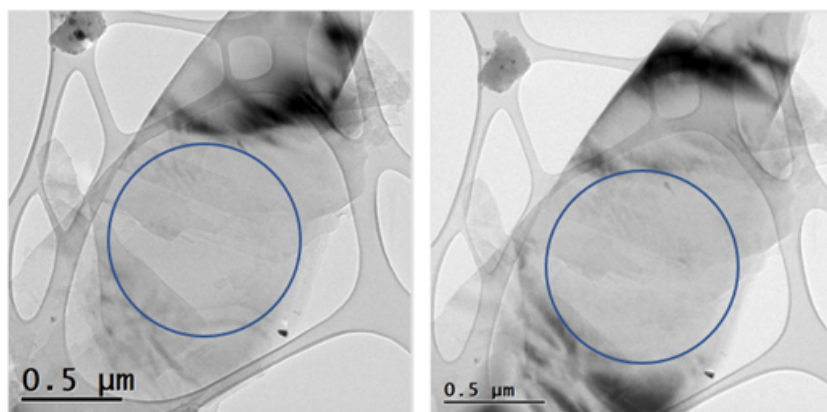


Figure 5.3: TEM image of graphite at a)  $0^\circ$  and b)  $60^\circ$  specimen holder tilt. EELS data was acquired from the circled area in each figure. At  $0^\circ$  tilt the c-axis of the graphite flake is parallel to the electron optic axis.

respectively. These values are smaller than  $\lambda$ , which confirms that multiple inelastic scattering is small in the measured EELS spectra. The carbon K-edge near edge fine structure can be attributed to promotion of a 1s core electron to unoccupied (anti-bonding) states of  $\pi^*$  and  $\sigma^*$  orbitals (see section 2.5.3). It is well known that graphite has  $sp^2$  and  $p_z$  bonding orbitals, and therefore exhibit both  $\pi^*$  and  $\sigma^*$  features in its carbon K-edge spectrum. (Leapman et al., 1983) report that the crystal orientation and scattering angle are found to strongly influence the K-edge fine structure for graphite due to anisotropy (section 2.5.3). This is clearly seen by comparing the EELS spectra acquired at  $0^\circ$  and  $60^\circ$  specimen tilts (Figure 5.4).

In Figure 5.4, the  $\pi^*$  and  $\sigma^*$  peaks are approximately at 285 eV and 292 eV respectively. In Figure 5.4a ( $0^\circ$  specimen tilt) the relative intensity of the  $\pi^*$  peak compared to the  $\sigma^*$  peak is much smaller than the spectrum at  $60^\circ$  specimen tilt (Figure 5.4b). To quantify the changes further we extracted the  $\pi^*$  peak intensity by least squares fitting a gaussian over a 4.3 eV energy window centred around the narrow  $\pi^*$  peak. The  $\sigma^*$  peak does not have a simple shape, and therefore its intensity was determined by integrating the number of counts over a 23 eV energy window between 287 eV and 310 eV energy losses. The  $\pi^*/\sigma^*$  intensity ratio can therefore be calculated. Figure 5.5 shows a plot of  $\pi^*/\sigma^*$  ratio vs specimen tilt, indicating that the  $\pi^*/\sigma^*$  ratio increases with tilt angle. To test that no beam

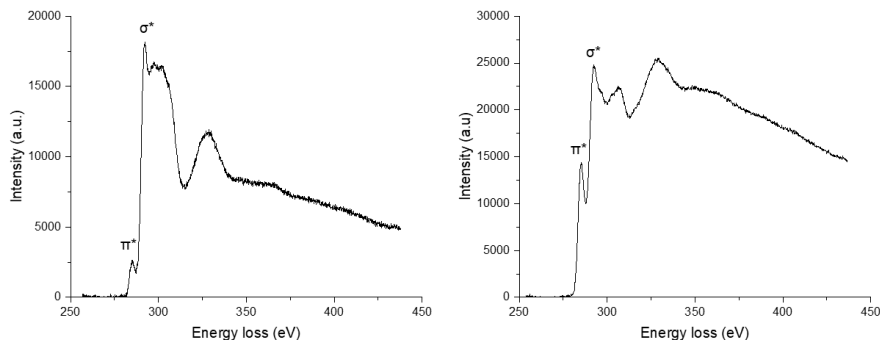


Figure 5.4: TEM EELS carbon K spectra for graphite recorded at specimen tilts of a)  $0^\circ$  and b)  $60^\circ$ . The  $\pi^*$  and  $\sigma^*$  features are indicated in each figure. At  $0^\circ$  tilt the c-axis of the graphite flake is parallel to the electron optic axis.

damage occurred while acquiring multiple EELS spectra from the same region, we rotated the sample holder back to the starting configuration of  $0^\circ$  and compared the result with the same measurement done at the start of the experiment at the same tilt. There was no discernible change in the EELS spectrum, indicating that Figure 5.5 is free from damage artefacts. Because the data in Figure 5.5 did not appear monotonic, the error bar was calculated assuming Poisson statistics for the EELS intensity and found to be smaller than the noise in the graph. Therefore, the random variations are likely to be coming from sources other than counting statistics, such as Bragg diffraction because the sample is crystalline. Bragg beams are tilted with respect to the incident beam, and therefore the EELS signal they contribute will have a different  $\pi^*/\sigma^*$  ratio.

At  $0^\circ$  tilt the graphite flakes are flat (Figure 5.3a), meaning that the crystal c-axis is parallel to the incoming (parallel) electron beam. It is therefore inferred that the  $\pi^*$  intensity increases with specimen tilt, or equivalently angle between the electron beam and graphite c-axis. This is opposite to the expected trend for small scattering angles, where the  $\pi^*/\sigma^*$  ratio is predicted to be highest at  $0^\circ$ . However, the size of the spectrometer collection angle can also impact the fine structure

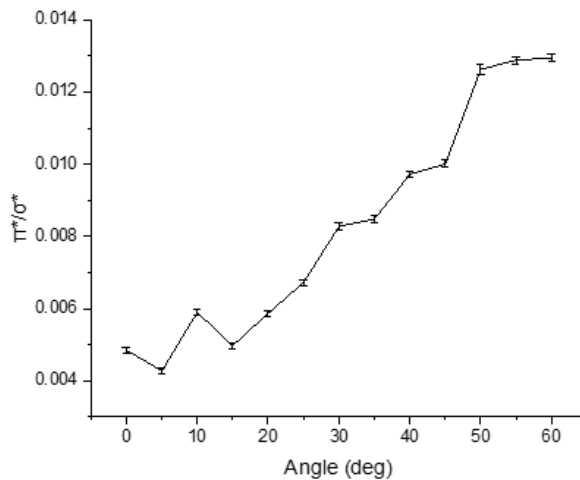


Figure 5.5: The  $\pi^*/\sigma^*$  intensity ratio in TEM EELS spectra of graphite as a function of specimen tilt angle. The line connecting the data points is a guide to the eye.

(Williams and Carter, 2009). The collection angle is one of the most important parameters in EELS because the intensity variation in the spectrum depends on the range of electron scattering angles that been gathered by the EELS spectrometer. Figure 5.6 shows the relationship between scattering vector ( $\vec{q}$ ), incident electron wavevector ( $\vec{k}$ ) and inelastically scattered wave vector ( $\vec{k}'$ ). The scattering vector can be resolved into two components: a transverse component  $q_{\text{transverse}} \sim k\theta$  normal to the incident beam, where  $\theta$  is the scattering angle, and a component  $q_{\text{min}}$  parallel to the incident beam.  $q_{\text{min}} = k\theta_E$ , where  $\theta_E$  is the characteristic scattering angle given approximated by  $\frac{E}{2E_0}$ , where  $E$  is the energy loss and  $E_0$  is the primary beam energy. For a small EELS collection angle  $\theta$  is small and the scattering vector is approximately  $q_{\text{min}}$ . Under these conditions, a sample at  $0^\circ$  orientation, i.e. incident electron beam parallel to the graphite c-axis, will give a strong  $\pi^*$  peak (Leapman et al., 1983). As  $\theta$  and the spectrometer collection angle increases, the scattering vector will have a larger transverse component,  $q_{\text{transverse}}$ . (Leapman et al., 1983) have shown that for larger  $\theta$  the  $\pi^*$  peak relative intensity decreases. For a carbon K-edge,  $E \sim 285$  eV and therefore  $\theta_E = 0.7$  mrad at 200 keV incident beam energy. On the other hand, the TEM EELS collection semi-

angle was determined by the objective aperture, which was 5.3 mrad. Since  $\theta > \theta_E$  for our measurements, the transverse scattering vector component is dominant, and therefore the  $\pi^*/\sigma^*$  ratio should increase with specimen tilt, consistent with the experimental results. There is however, still a small  $q_{min}$  component, which is why the  $\pi^*$  peak intensity does not go to zero at  $0^\circ$  specimen tilt (Figure 5.5).

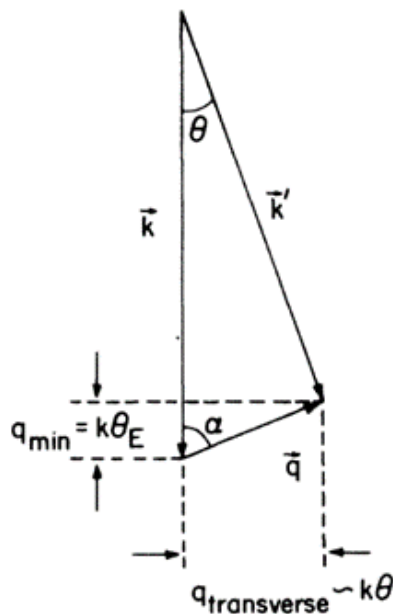


Figure 5.6: Diagram showing the relation between scattering angle ( $\theta$ ), scattering vector ( $\vec{q}$ ) and the incident and inelastically scattered electron wavevectors,  $\vec{k}$  and ( $\vec{k}'$ ) respectively Leapman et al. (1983).

Carbon K-edge fine structure data has also been acquired in STEM mode with 10.8 mrad probe semi-convergence angle. The camera length was adjusted so that the entire STEM transmitted beam disk passed through the EELS spectrometer entrance aperture. These are the same experimental conditions used for spatially mapping the  $\pi^*/\sigma^*$  ratio in a TIPS pentacene organic thin-film (section 5.4). STEM EELS data were acquired from the same area of the graphite flake as the TEM measurements. However, because the beam had been collapsed for STEM, there will be a range of incident angles with respect to the graphite sample. The angular resolution is therefore reduced for a converged STEM beam (Williams and Carter, 2009). The STEM EELS spectra for  $0^\circ$  and  $60^\circ$  specimen tilts are shown in Figure

5.7.

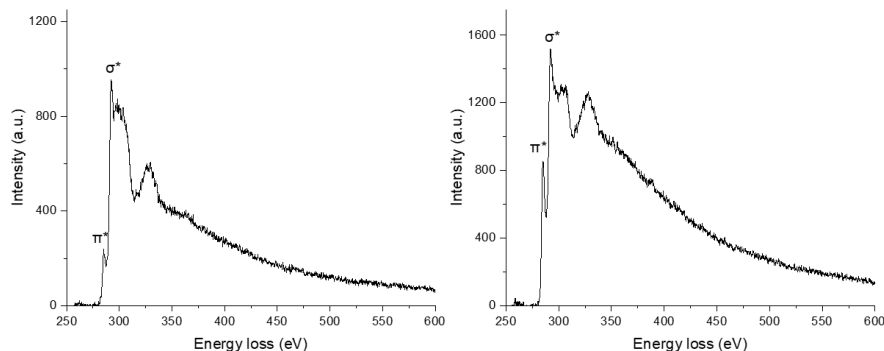


Figure 5.7: Energy loss spectrum of graphite carbon K-edge recorded using STEM EELS for a)  $0^\circ$  and b)  $60^\circ$  specimen tilt. Both graphs show  $\pi^*$  and  $\sigma^*$  features.

The relative intensity of the  $\pi^*$  peak increases with specimen tilt angle, similar to the TEM case (Figure 5.4). After acquiring carbon K-edge at different tilt angles in STEM, we determined the  $\pi^*$  and  $\sigma^*$  peak intensities with the same Gaussian fit and energy window as was used for TEM EELS. Figure 5.8 shows the  $\pi^*/\sigma^*$  ratio for STEM EELS as a function of specimen tilt angle. The increase in  $\pi^*/\sigma^*$  ratio with specimen tilt is due to the EELS collection angle  $\theta = 10.8$  mrad being larger than the characteristic scattering angle  $\theta_E$  (see discussion on TEM EELS data).

The  $\pi^*/\sigma^*$  ratio increased by a factor of 2.6 and 2.3 between  $0^\circ$  and  $60^\circ$  specimen tilt for TEM and STEM respectively. This suggests that the carbon K EELS fine structure is suitable for distinguishing between the two extreme types of  $\pi$  stacking, namely face-on ( $0^\circ$ ) and edge-on ( $90^\circ$ ). Intermediate molecular orientations can also be detected, although the systematic noise in the calibration graphs (Figures 5.5 and 5.8) would make it difficult to assign a precise angle. The main advantage of EELS is the higher spatial resolution attainable with STEM, which enables molecular orientation mapping at the nano-scale.

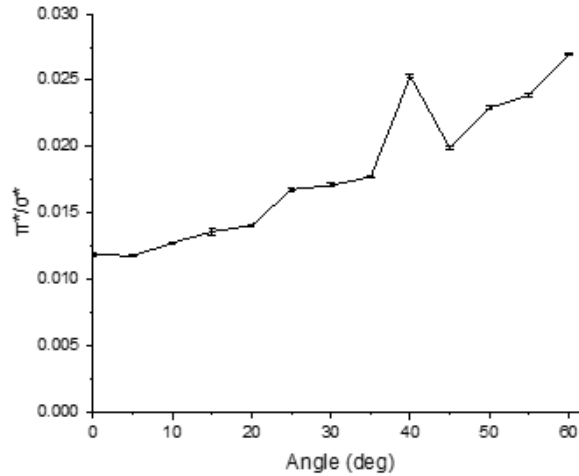


Figure 5.8: The  $\pi^*/\sigma^*$  ratio in STEM EELS as a function of specimen tilt angle. The line connecting the data points is a guide to the eye. The error bar is very small.

### 5.3 Beam Damage

In sub-section 2.5.3, we discussed EELS and how it relates to the inelastic scattering of the electron beam in which the incident electrons lose energy as they traversed the specimen. This inelastic scattering deposits energy which can damage the organic specimen, such as TIPS pentacene, if it is beam sensitive. The damage, which affects the crystalline structure of these specimens, mainly depends on the incident beam energy (although other factors, such as specimen temperature, thermal conductivity etc, may also contribute). For polymers and small molecules such as TIPS pentacene, the inelastic scattering can break the chemical bonds i.e.,  $\pi$  bonding, which is called radiolysis damage (Williams and Carter, 2009). To study the drop cast TIPS pentacene beam damage in our experiments, we acquired bright-field images of the bend contours and diffraction pattern at different stages of exposure to a 200 kV electron beam. Figure 5.9a shows the diffraction pattern and a TEM image of bend contours upon initial exposure to the electron beam. The diffraction pattern shows strong Bragg diffraction spots as well as the diffuse streaking reported in 4D STEM measurements (section 4.4.2). The presence of Bragg spots and

bend contours in the TEM image confirm crystallinity of the sample. To see how the sample looks like after few seconds, another diffraction pattern or TEM image was acquired from the same area (Figure 5.9b). The bend contours and diffraction spots disappear, indicating the sample has lost its long range crystallinity.

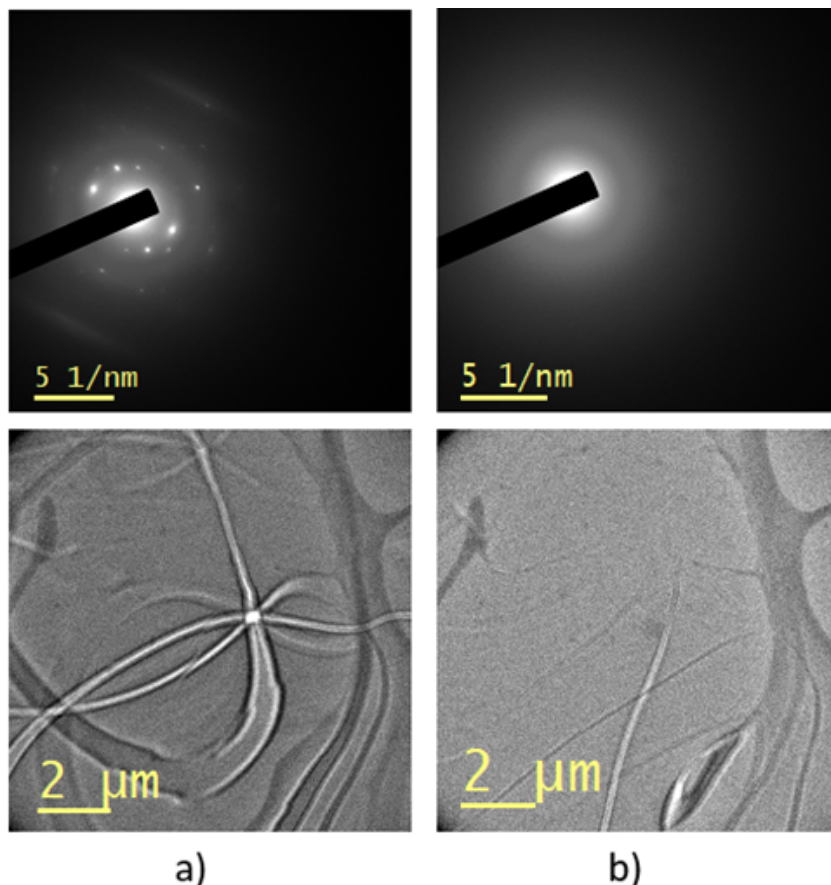


Figure 5.9: Diffraction pattern and TEM image showing bend contours in TIPS pentacene at a) 0 seconds and b) after few seconds respectively.

In order to quantify the critical electron dose for TIPS pentacene beam damage, the current density incident on the sample must be measured. This was done using the small phosphor screen with the electron beam passing through vacuum (note that more accurate methods for measuring the beam current, such as a Faraday cage, are not available on our microscope). The current density reading was  $160 \text{ pA/cm}^2$ , which gives an electron dose of  $25 \text{ e}/\text{\AA}^2$  for an acquisition time of  $0.025\text{s}$  (the shortest exposure time on our camera for the binning setting that was used). (Ilett et al., 2020) report a  $0.2\text{-}120 \text{ e}/\text{\AA}^2$  critical dose for organic crystals, which is

compatible with the value measured in this work.

## 5.4 STEM EELS Mapping

After calibrating the EELS  $\pi^*$  to  $\sigma^*$  ratio in a graphite reference specimen, we apply the technique to map the local molecular order in a TIPS pentacene thin-film using STEM EELS ‘spectrum imaging’. In spectrum imaging the STEM probe is rastered over a region of interest in the sample and an EELS spectrum collected at each scan position. By analysing the  $\pi^*$  to  $\sigma^*$  ratio for each EELS spectrum, a map of the local TIPS pentacene molecular orientation can be constructed. An important consideration is the electron dose used for spectrum imaging. The dose should be large enough to acquire a ‘clean’ EELS spectrum with good signal-to-noise ratio. However, the dose should also be below the critical value for electron beam damage. Furthermore, the acquisition time of a spectrum image data set should not be too long so that the specimen drifts in the electron microscope (due to random variations in the temperature), which can be achieved by using higher electron doses. Finally, there should also not be any specimen contamination during analysis. In particular, hydrocarbons on the thin film free surface can rapidly diffuse to the position of the STEM probe, and polymerise under the electron beam to form carbon contamination deposits, which will affect the measured  $\pi^*$  to  $\sigma^*$  ratio. To optimise the acquisition conditions we acquired spectrum image data sets with spot size number 4 and 5 STEM probes, the latter being the smallest STEM dose achievable on our microscope for a given objective aperture size.

Figures 5.10a and 5.10b show two STEM dark field images of drop cast TIPS pentacene, before and after acquiring a spectrum image data set over the highlighted region using a STEM probe with spot size number 5. The image intensity and features are largely the same between the two images, which suggests that there is little contamination or specimen drift during spectrum imaging. The equivalent images for STEM probe spot size number 4 are shown in Figures 5.10c and 5.10d.

There is a slight increase in dark-field intensity over the spectrum imaging region, which suggests some amount of contamination build up for this measurement.

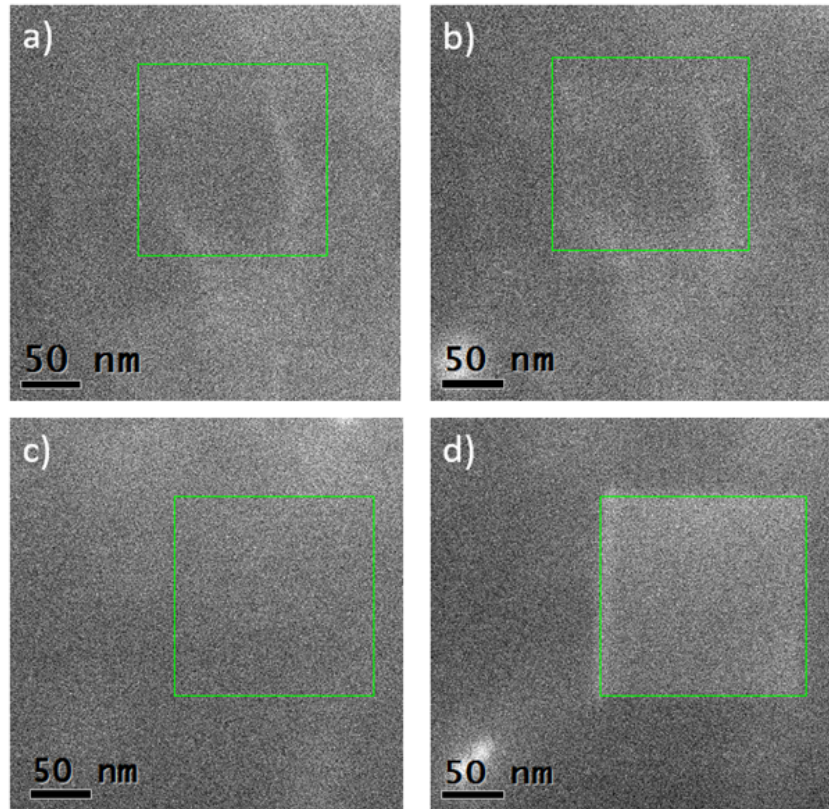


Figure 5.10: Dark field STEM images showing TIPS pentacene a) before and b) after acquiring an EELS spectrum image over the boxed region with STEM probe spot size number 5 as well as c) and d) for spot size number 4. The scale bar is 50 nm.

Several data processing steps had to be carried out before the  $\pi^*$  to  $\sigma^*$  ratio could be acquired from a spectrum image. First, we subtracted the background under the carbon K-edge using the standard power law fit (Egerton et al., 2005). Small deviations in the background subtracted, carbon K-edge position were observed between EELS spectra in the spectrum image. This is likely caused by drift of the EELS spectrometer due to stray electromagnetic fields during spectrum image acquisition, i.e., the zero-loss peak reference point does not stay fixed in the same CCD channel. This energy drift was corrected by taking the EELS spectrum at the start of the acquisition as a reference spectrum, and using cross-correlation to align all spectra in the spectrum image to the reference. In particular, the EELS

spectrum was shifted over an energy window corresponding to  $\pm 20$  pixels, and the square difference between the shifted spectrum and reference spectrum calculated for each shift. The ideal shift was when the square difference was minimised. A Digital Micrograph script was used to automate this process for all EELS spectra in the spectrum image. Figure 5.11 shows representative EELS spectra extracted from a single ‘point’ in spectrum image data sets for STEM probe spot size numbers 5 and 4; the background has been subtracted and the carbon K-edge energy loss corrected for any energy drift. The EELS spectrum for spot size number 5 has a lower signal-to-noise ratio due to the lower electron beam current in the STEM probe.

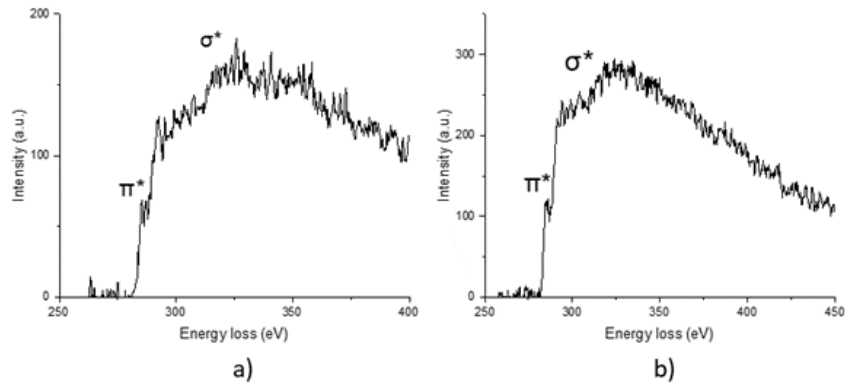


Figure 5.11: Energy loss spectrum of TIPS pentacene carbon K-edge recorded using STEM probe spot size numbers a) 5 and b) 4. The EELS spectra were extracted from a single ‘point’ in a spectrum image data set.

The process to measure  $\pi^*$  and  $\sigma^*$  peak intensities were similar to the TEM and STEM tomography measurements in section 5.2. Specifically, the  $\pi^*$  peak intensity was Gaussian fitted over a 4.3 eV energy window and  $\sigma^*$  peak intensity determined by integrating the number of counts over a 100 eV energy window between 287 eV and 387 eV energy losses. This was done for each ‘point’ in the spectrum image, which enabled a map of the  $\pi^*/\sigma^*$  intensity ratio to be constructed.

Figures 5.12a and 5.12b show the  $\pi^*/\sigma^*$  ratio maps calculated from the EELS spectrum image datasets (Figure 5.10) for STEM spot size numbers 5 and 4 respectively. The intensity scale for the maps vary between 0 and 0.05; this range was

chosen based on the measured  $\pi^*/\sigma^*$  ratios for the graphite test specimen (Figure 5.8), and should cover all specimen orientations. The TIPS pentacene  $\pi^*/\sigma^*$  ratio map had a minimum and maximum value of 0.005 and 0.7 respectively for spot size number 5. Due to this large range many of the pixels appear saturated in the  $\pi^*/\sigma^*$  ratio map (Figure 5.12a). For spot size number 4 however the minimum and maximum  $\pi^*/\sigma^*$  ratio values were 0.005 and 0.01 respectively, a much narrower distribution that is within the expected range. The larger spread in  $\pi^*/\sigma^*$  ratio values in Figure 5.12a is attributed to the lower signal-to-noise ratio for EELS spectra recorded with a spot size number 5 STEM probe. For accurate measurements a STEM probe with spot size number 4 or lower must therefore be used. The  $\pi^*/\sigma^*$  ratio map (Figure 5.12b) is also more spatially uniform. This could be because TIPS pentacene molecules are of uniform orientation within the analysed region. The build-up of carbon contamination during EELS measurement (Figure 5.10b) will also suppress any small changes in the  $\pi^*/\sigma^*$  ratio intrinsic to the TIPS pentacene thin-film.

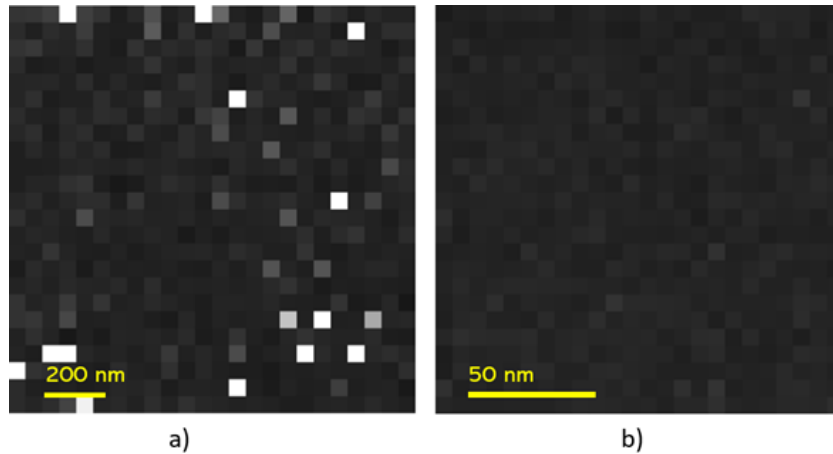


Figure 5.12: TIPS pentacene  $\pi^*/\sigma^*$  ratio maps calculated from EELS spectrum images acquired with STEM probe spot size number a) 5 and b) 4.

The electron beam dose during EELS spectrum imaging and any potential beam damage to the specimen will now be quantified. We used the small phosphor screen in the TEM to measure the current density for STEM probe spot size number 4 to be 18.4 pA/cm<sup>2</sup>. To estimate the STEM probe current we multiply the current

density by the area of the phosphor screen :

$$\frac{\pi d^2}{4} \tag{5.1}$$

where  $d$  is the diameter of the small phosphor screen on the JEOL 2100F (20 mm). The total number of electrons ( $N$ ) used for a single EELS measurement can be calculated using equation 5.2:

$$N = \frac{It}{q} \tag{5.2}$$

where  $I$  is the STEM probe current,  $t$  is the acquisition time per EELS spectrum (0.5s) and  $q$  is the charge of an electron ( $1.6 \times 10^{-19}$  C). Finally dividing number of electrons by the area of a pixel (size 6.8 nm) in the spectrum image gives the electron dose, i.e.  $3.9 \times 10^4$  e/ $\text{\AA}^2$  for spot size number 4 STEM probe. Note that this estimate is a lower limit, since the pixel size is much larger than the STEM probe size (0.05 nm); dividing the number of electrons by the STEM probe area would give a larger electron dose. The electron dose for EELS spectrum imaging is several orders of magnitude larger than the 25 e/ $\text{\AA}^2$  critical dose for beam damage estimated using TEM (section 5.3). The beam damage is expected to take the form of bond breaking (i.e. radiolysis) in TIPS pentacene, particularly the weaker inter-molecular bonds. From Figure 5.10 there is however no evidence for sputter damage, since the constant mass-thickness contrast indicates no loss of material from the thin-film. Therefore, it is concluded that the electron dose required for accurate  $\pi^*/\sigma^*$  ratio mapping is significantly higher than critical dose for electron beam damage. Strategies to minimise the electron beam damage are therefore critical if STEM EELS is to be used for molecular orientation mapping.

## 5.5 Conclusions

This chapter explored the possibility of using the carbon K-edge EELS fine structure for mapping the local orientation of organic thin-films, such as TIPS pentacene. A natural graphite sample was used to calibrate the  $\pi^*/\sigma^*$  ratio as a function of specimen orientation, since it is stable under the electron beam. TEM and STEM EELS measurements were used to determine the orientation of graphite  $\pi$ -stacking at specimen tilts ranging from  $0^\circ$  to  $60^\circ$  in step sizes of  $5^\circ$ . The EELS collection semi-angle for TEM and STEM were determined by the objective aperture size (5.3 mrad) and probe semi-convergence angle (10.8 mrad) respectively, which is larger than the characteristic scattering angle ( $\theta_E$ ) for the carbon K-edge (0.7 mrad). These collection angles are also much larger than the magic angle (i.e.  $2\theta_E = 1.4$  mrad) where EELS spectra are independent of orientation (Daniels et al. (2003)), so that the measurement is sensitive to the orientation of the molecule/crystal. The  $\pi^*$  peak therefore increased when increasing the specimen tilt angle from  $0^\circ$  to  $60^\circ$  (Figures 5.4 and 5.7). The critical electron beam dose for TIPS pentacene was estimated to be  $25 \text{ e}/\text{\AA}^2$ , which is within the range reported for organic crystals (Ilett et al., 2020). EELS spectrum imaging was performed over a region of interest of the TIPS pentacene thin-film, from which a  $\pi^*/\sigma^*$  ratio map can be constructed. STEM probes with spot size numbers 4 and 5 were used for data acquisition, the latter containing a lower electron beam current. The accuracy of the measured  $\pi^*/\sigma^*$  ratio depends on the signal-to-noise ratio of the EELS spectrum. The signal-to-noise ratio can be improved by using STEM probes with higher current, i.e. lower spot size numbers. It was shown that for TIPS pentacene a STEM probe with spot size number 4 or lower is required to give accurate  $\pi^*/\sigma^*$  ratios. The electron dose for a spot size number 4 STEM probe was however estimated to be  $3.9 \times 10^4 \text{ e}/\text{\AA}^2$ , well above the critical dose for electron beam damage. Therefore, strategies to minimise electron beam damage is essential for EELS measurements of molecular orientation in organic thin-films.

---

## Future work

In the previous chapters, we mentioned that polymers and small molecules are easily damaged by the electron beam. For example, it was difficult to see any stable features in the dark field images and diffraction patterns of drop cast and spin coated TIPS pentacene samples. This includes the tiny crystallites in the spin coated TIPS pentacene sample, which were only revealed using a direct electron detector under low dose conditions. For a standard scintillator based CMOS detector the fading of diffraction spots to amorphous rings occurred too rapidly to detect the presence of any crystallinity (section 4.4). For chemical analysis, fine structure of the carbon K-edge in electron energy loss spectroscopy (EELS) was analysed for both graphite and TIPS pentacene. The graphite showed a good result, unlike TIPS where the weak inter-molecular bonding was broken due to its higher beam sensitivity, i.e. radiolysis damage. Furthermore, the minimum electron dose required to get an accurate  $\pi^*$  to  $\sigma^*$  ratio and map the molecular orientation using STEM EELS spectrum imaging is many orders of magnitude higher than the critical dose for TIPS pentacene (section 5.4). These observations indicate that beam damage mitigation is essential for the analysis of organic polymers and small molecules. In this chapter we examine some factors that might help reduce beam damage and improve the quality in any future analysis. The investigation can be broadened by using cryo-microscopy techniques where the specimen is cooled to liquid nitrogen temperatures. This reduces the electron beam damage by limiting

the diffusion of secondary products produced during radiolysis (S'ari et al., 2018). Furthermore, 'dose fractionation' methods, where the signal from many different molecules acquired below the damage threshold is averaged, could also be used, although this reduces the spatial resolution.

According to Ilett et al. (Ilett et al., 2020) the radiolysis damage is less for  $\pi$  conjugated organic molecules, since the delocalised nature of the  $\pi$  electrons enables the energy deposited from the electron beam to be distributed over a relatively large area, i.e. the entire molecule rather than a single chemical bond. The cross-section for radiolysis damage also decreases at higher incident electron beam energies, meaning that microscopes with higher kV are better suited for studying organic materials. However, note that all materials also suffer from knock-on or sputter damage if the accelerating voltage is high enough (Williams and Carter, 2009). Therefore, there is an optimum kV that must be used, which keeps both radiolysis and sputter damage to a minimum. Nevertheless, beam damage studies on theophylline has shown that the critical dose is higher at 300 kV compared to 200 kV (Ilett et al., 2020). The latter was used in the present studies and there is a possibility that better results could have been obtained by using a TEM operating at 300 kV. A further approach is to optimise the detection of the images, diffraction patterns, and electron energy loss spectra generated by TEM and STEM. While this does not change the critical dose the sample can be exposed to, it means that more information is extracted from a given electron dose. The detector quantum efficiency (DQE) of a charge-coupled device (CCD) detector is decreased by the use of a scintillator causing a loss in image quality. The CCD detector is a metal-insulator-silicon device that stores charge generated by electron beams. The CCD cannot however be directly exposed to the high energy electron beam. Hence a scintillator is first used to convert the electron energy into photons that are then transferred to the CCD sensor via a fibre optic plate (Figure 6.1). There are optical losses in the fibre optics which gives rise to a lower DQE. Compared to a scintillator in a CCD camera, a direct electron detector (with no scintillator) is

exposed to the electron beam directly, typically giving higher DQE that is equal to 0.8 or higher, without single electron arrival discrimination (Plotkin-Swing et al., 2020). Particularly for low contrast images, a direct electron detector gives better image quality (reduced noise); an example from our experiments is the diffraction patterns for TIPS pentacene sample acquired via 4D STEM (see Figure 4.17 in subsection 4.4.2). This data shows far more features than that obtained using scintillator based detectors. Direct electron detectors are available in two varieties:

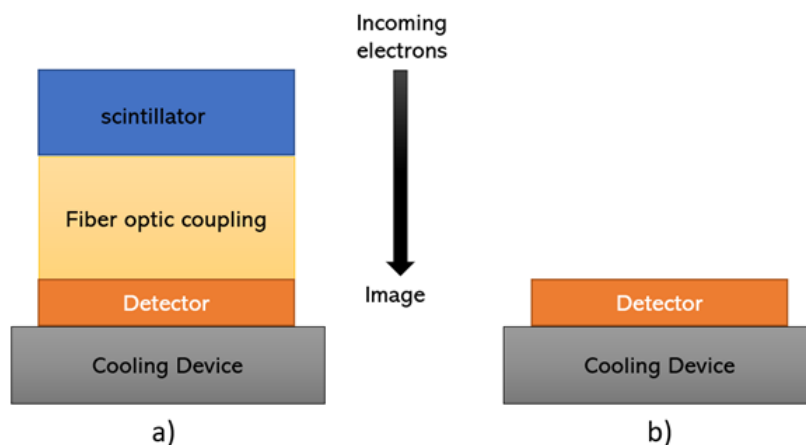


Figure 6.1: A diagram showing the basic features of a) scintillator based and b) direct electron detectors. Each schematic shows electrons passing through the detector.

ies: hybrid pixel detectors (Plotkin-Swing et al., 2020) and active pixel sensors (Milazzo et al., 2005). The hybrid pixel detector, which is also known as a pixel array detector (PAD) is a sensor chip that is connected to a separate electronic chip that simultaneously reads each pixel. The detector is suitable for EELS, since it is resistant to radiation damage, has a wide dynamic range, and a narrow point spread function. It can accommodate up to 0.8 pA per pixel, and thus  $>100$  pA EELS zero-loss peak (ZLP) without saturation because it can detect approximately  $5 \times 10^6$  electrons per pixel per second (Plotkin-Swing et al., 2020). In addition, it is able to accurately detect isolated single electrons in the spectrum high energy loss region (Plotkin-Swing et al., 2020). Active pixel sensors (APS) built on back-thinned complementary metal-oxide semiconductor (CMOS), such as the Gatan K2, have also been used as direct detectors in TEM (McMullan et al., 2014). APS

enable low electron dose rates at energies between 200 and 300 keV. Even if CMOS detectors have small pixel sizes around 5–15  $\mu\text{m}$ , there are other detectors that use larger pixels that can be 55  $\mu\text{m}$ , or even up to 150  $\mu\text{m}$  for a two-layer design (Plotkin-Swing et al., 2020). Applications such as cryo-TEM and STEM-EELS have benefited from the successful use of direct electron detectors. Examples of 4D STEM application detectors are Medipix, a hybrid pixel detector (Mir et al., 2017), which can record an electron dose less than  $0.05 \text{ e}/\text{\AA}^2$  (Georgieva et al., 2011) and the electron microscope pixel array detector (EMPAD) (Tate et al., 2016).

---

## Bibliography

- M. T. Abdullah, A. S. S. Ahmad, A. A. Mohammed, et al. The effect of doped indium on the electrical and optical properties of (se 0.7 te 0.3) 1- x in x thin films. *Advances in Materials Physics and Chemistry*, 5(04):140, 2015.
- T. Adachi, J. Brazard, P. Chokshi, J. C. Bolinger, V. Ganesan, and P. F. Barbara. Highly ordered single conjugated polymer chain rod morphologies. *The Journal of Physical Chemistry C*, 114(48):20896–20902, 2010.
- J. E. Anthony. Functionalized acenes and heteroacenes for organic electronics. *Chemical reviews*, 106(12):5028–5048, 2006.
- J. E. Anthony. The larger acenes: versatile organic semiconductors. *Angewandte Chemie International Edition*, 47(3):452–483, 2008.
- J. E. Anthony, J. S. Brooks, D. L. Eaton, and S. R. Parkin. Functionalized pentacene: Improved electronic properties from control of solid-state order. *Journal of the American Chemical Society*, 123(38):9482–9483, 2001.
- J. E. Anthony, D. L. Eaton, and S. R. Parkin. A road map to stable, soluble, easily crystallized pentacene derivatives. *Organic letters*, 4(1):15–18, 2002.
- O. Bäcke, C. Lindqvist, A. D. de Zerio Mendaza, S. Gustafsson, E. Wang, M. R. Andersson, C. Müller, P. M. Kristiansen, and E. Olsson. Enhanced thermal

- stability of a polymer solar cell blend induced by electron beam irradiation in the transmission electron microscope. *Ultramicroscopy*, 176:23–30, 2017.
- G. T. Barkema and N. Mousseau. High-quality continuous random networks. *Physical Review B*, 62(8):4985, 2000.
- H. F. Bettinger. Electronic structure of higher acenes and polyacene: The perspective developed by theoretical analyses. *Pure and Applied Chemistry*, 82(4):905–915, 2010.
- D. Bharti and S. P. Tiwari. Improved alignment and crystallinity of tips-pentacene thin films by off-center spin coating. In *2015 IEEE 15th International Conference on Nanotechnology (IEEE-NANO)*, pages 432–435. IEEE, 2015.
- S. N. Bogle, P. M. Voyles, S. V. Khare, and J. R. Abelson. Quantifying nano-scale order in amorphous materials: simulating fluctuation electron microscopy of amorphous silicon. *Journal of Physics: Condensed Matter*, 19(45):455204, 2007.
- A. Bogner, P.-H. Jouneau, G. Thollet, D. Basset, and C. Gauthier. A history of scanning electron microscopy developments: Towards “wet-stem” imaging. *Micron*, 38(4):390–401, 2007.
- J.-L. Brédas, Y. Li, H. Sun, and C. Zhong. Why can high charge-carrier mobilities be achieved along  $\pi$ -conjugated polymer chains with alternating donor–acceptor moieties? *Advanced Theory and Simulations*, 1(7):1800016, 2018.
- J. W. Bush. Pilot-wave hydrodynamics. 2015.
- K. C. Bustillo, S. E. Zeltmann, M. Chen, J. Donohue, J. Ciston, C. Ophus, and A. M. Minor. 4d-stem of beam-sensitive materials. *Accounts of chemical research*, 54(11):2543–2551, 2021.
- W. D. Callister, D. G. Rethwisch, et al. *Materials science and engineering: an introduction*, volume 7. John wiley & sons New York, 2007.

- F.-C. Chen, Y.-P. Chen, Y.-J. Huang, and S.-C. Chien. Morphological study on pentacene thin-film transistors: the influence of grain boundary on the electrical properties. *Journal of Physics D: Applied Physics*, 43(40):405103, 2010.
- J. Chen, D. C. Martin, and J. E. Anthony. Morphology and molecular orientation of thin-film bis (triisopropylsilylethynyl) pentacene. *Journal of materials research*, 22(6):1701–1709, 2007.
- C.-J. Chiang. *Nano Structure and Novel Charging Materials of the Small Molecule Based OLED Devices*. PhD thesis, Durham University, 2007.
- M. Chowdhury, M. T. Sajjad, V. Savikhin, N. Hergué, K. B. Sutija, S. D. Oosterhout, M. F. Toney, P. Dubois, A. Ruseckas, and I. D. Samuel. Tuning crystalline ordering by annealing and additives to study its effect on exciton diffusion in a polyalkylthiophene copolymer. *Physical Chemistry Chemical Physics*, 19(19):12441–12451, 2017.
- J. Cowley. Electron nanodiffraction methods for measuring medium-range order. *Ultramicroscopy*, 90(2-3):197–206, 2002.
- J. t. Cowley and A. Moodie. The scattering of electrons by atoms and crystals. iii. single-crystal diffraction patterns. *Acta Crystallographica*, 12(5):360–367, 1959.
- M. Cowley. Stem imaging with a thin annular detector. *Journal of electron microscopy*, 50(3):147–155, 2001.
- H. Daniels, A. Brown, A. Scott, T. Nichells, B. Rand, and R. Brydson. Experimental and theoretical evidence for the magic angle in transmission electron energy loss spectroscopy. *Ultramicroscopy*, 96(3-4):523–534, 2003.
- C. D. Dimitrakopoulos and P. R. Malenfant. Organic thin film transistors for large area electronics. *Advanced materials*, 14(2):99–117, 2002.
- J. Donohue, S. E. Zeltmann, K. C. Bustillo, B. Savitzky, M. A. Jones, G. F. Meyers, C. Ophus, and A. M. Minor. Cryogenic 4d-stem analysis of an amorphous-

- crystalline polymer blend: Combined nanocrystalline and amorphous phase mapping. *Science*, 25(3):103882, 2022.
- R. Egerton and M. Malac. Eels in the tem. *Journal of Electron Spectroscopy and Related Phenomena*, 143(2-3):43–50, 2005.
- R. F. Egerton. Electron energy-loss spectroscopy in the tem. *Reports on Progress in Physics*, 72(1):016502, 2008.
- R. F. Egerton et al. *Physical principles of electron microscopy*, volume 56. Springer, 2005.
- A. S. Eggeman, S. Illig, A. Troisi, H. Siringhaus, and P. A. Midgley. Measurement of molecular motion in organic semiconductors by thermal diffuse electron scattering. *Nature materials*, 12(11):1045–1049, 2013.
- A. Facchetti.  $\pi$ -conjugated polymers for organic electronics and photovoltaic cell applications. *Chemistry of Materials*, 23(3):733–758, 2011.
- L. Fan, I. McNulty, D. Paterson, M. M. Treacy, and J. M. Gibson. Fluctuation x-ray microscopy for measuring medium-range order. *MRS Online Proceedings Library (OPL)*, 840, 2004.
- J. Fatermans, A. Den Dekker, K. Müller-Caspary, I. Lobato, C. O’Leary, P. Nellist, and S. Van Aert. Single atom detection from low contrast-to-noise ratio electron microscopy images. *Physical review letters*, 121(5):056101, 2018.
- S. R. Forrest. The path to ubiquitous and low-cost organic electronic appliances on plastic. *nature*, 428(6986):911–918, 2004.
- M. Geoghegan and G. Hadziioannou. *Polymer electronics*, volume 22. OUP Oxford, 2013.
- D. Georgieva, J. Jansen, I. Sikharulidze, L. Jiang, H. Zandbergen, and J. Abrahams. Evaluation of medipix2 detector for recording electron diffraction data in low dose conditions. *Journal of Instrumentation*, 6(01):C01033, 2011.

- J. Gibson and M. Treacy. Diminished medium-range order observed in annealed amorphous germanium. *Physical Review Letters*, 78(6):1074, 1997.
- C. M. Graney. Objects in telescope are farther than they appear: How diffraction tricked galileo into mismeasuring distances to the stars. *The Physics Teacher*, 47(6):362–365, 2009.
- C. Grieco, G. S. Doucette, R. D. Pensack, M. M. Payne, A. Rimshaw, G. D. Scholes, J. E. Anthony, and J. B. Asbury. Dynamic exchange during triplet transport in nanocrystalline tips-pentacene films. *Journal of the American Chemical Society*, 138(49):16069–16080, 2016.
- J. A. Hachtel, J. C. Idrobo, and M. Chi. Sub-ångstrom electric field measurements on a universal detector in a scanning transmission electron microscope. *Advanced structural and chemical imaging*, 4(1):1–10, 2018.
- A.-L. Hamon, J. Verbeeck, D. Schryvers, J. Benedikt, and R. M. vd Sanden. Elnes study of carbon k-edge spectra of plasma deposited carbon films. *Journal of Materials Chemistry*, 14(13):2030–2035, 2004.
- A. M. Haruk and J. M. Mativetsky. Supramolecular approaches to nanoscale morphological control in organic solar cells. *International Journal of Molecular Sciences*, 16(6):13381–13406, 2015.
- A. J. Heeger. Semiconducting and metallic polymers: the fourth generation of polymeric materials, 2001.
- S. Hilke, H. Rösner, D. Geissler, A. Gebert, M. Peterlechner, and G. Wilde. The influence of deformation on the medium-range order of a zr-based bulk metallic glass characterized by variable resolution fluctuation electron microscopy. *Acta Materialia*, 171:275–281, 2019.
- W. Huang, E. Gann, Y.-B. Cheng, and C. R. McNeill. In-depth understanding of the morphology–performance relationship in polymer solar cells. *ACS applied materials & interfaces*, 7(25):14026–14034, 2015.

- J. Hwang and P. Voyles. Variable resolution fluctuation electron microscopy on cu-zr metallic glass using a wide range of coherent stem probe size. *Microscopy and Microanalysis*, 17(1):67–74, 2011.
- M. Ilett, M. S’ari, H. Freeman, Z. Aslam, N. Koniuch, M. Afzali, J. Cattle, R. Hooley, T. Roncal-Herrero, S. M. Collins, et al. Analysis of complex, beam-sensitive materials by transmission electron microscopy and associated techniques. *Philosophical Transactions of the Royal Society A*, 378(2186):20190601, 2020.
- K. Ishizuka. A practical approach for stem image simulation based on the fft multislice method. *Ultramicroscopy*, 90(2-3):71–83, 2002.
- C. Janiak. A critical account on  $\pi$ - $\pi$  stacking in metal complexes with aromatic nitrogen-containing ligands. *Journal of the Chemical Society, Dalton Transactions*, (21):3885–3896, 2000.
- K. Jarausch, P. Thomas, D. N. Leonard, R. Twesten, and C. R. Booth. Four-dimensional stem-eels: Enabling nano-scale chemical tomography. *Ultramicroscopy*, 109(4):326–337, 2009.
- N. H. Julian, T. T. Li, R. E. Rudd, and J. Marian. Ms-stem-fem: A parallelized multi-slice fluctuation tem simulation tool. *Ultramicroscopy*, 194:117–125, 2018.
- Y.-H. Kim, Y. U. Lee, J.-I. Han, S.-M. Han, and M.-K. Han. Influence of solvent on the film morphology, crystallinity and electrical characteristics of triisopropylsilyl pentacene offts. *Journal of the Electrochemical Society*, 154(12):H995, 2007.
- E. J. Kirkland. Bilinear interpolation. In *Advanced Computing in Electron Microscopy*, pages 261–263. Springer, 2010.
- R. Kline and M. McGehee. Morphology and charge transport in conjugated polymers. *Journal of Macromolecular Science Part C: Polymer Reviews*, 46(1):27–45, 2006.

- D. Knipp, R. Street, and A. Völkel. Morphology and electronic transport of polycrystalline pentacene thin-film transistors. *Applied Physics Letters*, 82(22):3907–3909, 2003.
- N. Koch. Organic electronic devices and their functional interfaces. *ChemPhysChem*, 8(10):1438–1455, 2007.
- A. Koehler and H. Baessler. The electronic structure of organic semiconductors, 2015.
- Y. H. Krieger. Structural instability of one-dimensional systems as a physical principle underlying the functioning of molecular electronic devices. *Journal of Structural Chemistry*, 40(4):594–619, 1999.
- A. Kulovits, G. Facco, and J. Wiezorek. Grain size determination in nano-scale polycrystalline aggregates by precession illumination-hollow cone dark field imaging in the transmission electron microscope. *Materials characterization*, 63:17–26, 2012.
- T.-H. Le, Y. Kim, and H. Yoon. Electrical and electrochemical properties of conducting polymers. *Polymers*, 9(4):150, 2017.
- R. Leapman, P. Fejes, and J. Silcox. Orientation dependence of core edges from anisotropic materials determined by inelastic scattering of fast electrons. *Physical review B*, 28(5):2361, 1983.
- B.-S. Lee, S. G. Bishop, and J. R. Abelson. Fluctuation transmission electron microscopy: Detecting nanoscale order in disordered structures. *Chemphyschem*, 11(11):2311–2317, 2010.
- M. Li, C. An, T. Marszalek, M. Baumgarten, H. Yan, K. Müllen, and W. Pisula. Controlling the surface organization of conjugated donor–acceptor polymers by their aggregation in solution. *Advanced Materials*, 28(42):9430–9438, 2016.

- T. T. Li, S. N. Bogle, and J. R. Abelson. Quantitative fluctuation electron microscopy in the stem: Methods to identify, avoid, and correct for artifacts. *Microscopy and Microanalysis*, 20(5):1605–1618, 2014.
- Y. Liao. Practical electron microscopy and database. *An Online Book*, 2006.
- J. Liu. Scanning transmission electron microscopy and its application to the study of nanoparticles and nanoparticle systems. *Journal of electron microscopy*, 54(3):251–278, 2005.
- X. Lu and Y. Hu. *Molecular Thermodynamics of Complex Systems*, volume 131. Springer, 2008.
- K. E. MacArthur. The use of annular dark-field scanning transmission electron microscopy for quantitative characterisation. *Johnson Matthey Technology Review*, 60(2):117–131, 2016.
- D. C. Martin, J. Chen, J. Yang, L. F. Drummy, and C. Kübel. High resolution electron microscopy of ordered polymers and organic molecular crystals: Recent developments and future possibilities. *Journal of Polymer Science Part B: Polymer Physics*, 43(14):1749–1778, 2005.
- P. McEuen and C. Kittel. Introduction to solid state physics. 2005.
- G. McMullan, A. Faruqi, D. Clare, Henderson, and R. Comparison of optimal performance at 300 keV of three direct electron detectors for use in low dose electron microscopy. *Ultramicroscopy*, 147:156–163, 2014.
- H. Meyers and H. Myers. *Introductory solid state physics*. CRC press, 1997.
- A.-C. Milazzo, P. Leblanc, F. Duttweiler, L. Jin, J. C. Bouwer, S. Peltier, M. Ellisman, F. Bieser, H. S. Matis, H. Wieman, et al. Active pixel sensor array as a detector for electron microscopy. *Ultramicroscopy*, 104(2):152–159, 2005.

- J. Mir, R. Clough, R. MacInnes, C. Gough, R. Plackett, I. Shipsey, H. Sawada, I. MacLaren, R. Ballabriga, D. Maneuski, et al. Characterisation of the medipix3 detector for 60 and 80 keV electrons. *Ultramicroscopy*, 182:44–53, 2017.
- S. Morishita, J. Yamasaki, K. Nakamura, T. Kato, and N. Tanaka. Diffractive imaging of the dumbbell structure in silicon by spherical-aberration-corrected electron diffraction. *Applied Physics Letters*, 93(18):183103, 2008.
- X. Mu, A. Mazilkin, C. Sprau, A. Colsmann, and C. Kübel. Mapping structure and morphology of amorphous organic thin films by 4d-stem pair distribution function analysis. *Microscopy*, 68(4):301–309, 2019.
- A. Musa, A. Gidado, L. Mohammed, K. Yunusa, and A. Suleiman. Molecular and electronic properties of rubrene and its cyanide derivative using density functional theory (dft).
- J. S. Nagra. Modelling microstructure-property relationships in polycrystalline metals using new fast fourier transform-based crystal plasticity frameworks. 2019.
- B. S. Nair and S. Deepa. *Applied Electromagnetic Theory: Analyses, Problems and Applications*. PHI Learning Pvt. Ltd., 2008.
- R. Noriega, J. Rivnay, K. Vandewal, F. P. Koch, N. Stingelin, P. Smith, M. F. Toney, and A. Salleo. A general relationship between disorder, aggregation and charge transport in conjugated polymers. *Nature materials*, 12(11):1038–1044, 2013.
- J. Oelerich, F. Jansson, A. Nenashev, F. Gebhard, and S. Baranovskii. Energy position of the transport path in disordered organic semiconductors. *Journal of Physics: condensed matter*, 26(25):255801, 2014.
- C. Ophus. Four-dimensional scanning transmission electron microscopy (4d-stem): From scanning nanodiffraction to ptychography and beyond. *Microscopy and Microanalysis*, 25(3):563–582, 2019.

- M. P. Oxley, A. R. Lupini, and S. J. Pennycook. Ultra-high resolution electron microscopy. *Reports on Progress in physics*, 80(2):026101, 2016.
- R. Pal, A. K. Sikder, K. Saito, A. M. Funston, and J. R. Bellare. Electron energy loss spectroscopy for polymers: a review. *Polymer Chemistry*, 8(45):6927–6937, 2017.
- R. Pal, L. Bourgeois, M. Weyland, A. K. Sikder, K. Saito, A. M. Funston, and J. R. Bellare. Chemical fingerprinting of polymers using electron energy-loss spectroscopy. *ACS omega*, 6(37):23934–23942, 2021.
- O. Panova, C. Ophus, C. J. Takacs, K. C. Bustillo, L. Balhorn, A. Salleo, N. Balsara, and A. M. Minor. Diffraction imaging of nanocrystalline structures in organic semiconductor molecular thin films. *Nature materials*, 18(8):860–865, 2019.
- A. S. Paraskar, A. R. Reddy, A. Patra, Y. H. Wijsboom, O. Gidron, L. J. Shimon, G. Leitius, and M. Bendikov. Rubrenes: planar and twisted. *Chemistry–A European Journal*, 14(34):10639–10647, 2008.
- C. Pitsalidis, N. Kalfagiannis, N. A. Hastas, P. Karagiannidis, C. Kapnopoulos, A. Ioakeimidis, and S. Logothetidis. High performance transistors based on the controlled growth of triisopropylsilylethynyl-pentacene crystals via non-isotropic solvent evaporation. *Rsc Advances*, 4(40):20804–20813, 2014.
- B. Plotkin-Swing, G. J. Corbin, S. De Carlo, N. Dellby, C. Hoermann, M. V. Hoffman, T. C. Lovejoy, C. E. Meyer, A. Mittelberger, R. Pantelic, et al. Hybrid pixel direct detector for electron energy loss spectroscopy. *Ultramicroscopy*, 217: 113067, 2020.
- C. Poelking, K. Daoulas, A. Troisi, and D. Andrienko. Morphology and charge transport in p3ht: a theorist’s perspective. *P3HT Revisited–From Molecular Scale to Solar Cell Devices*, pages 139–180, 2014.

- V. Raghuwanshi, D. Bharti, and S. P. Tiwari. Flexible organic field-effect transistors with tips-pentacene crystals exhibiting high electrical stability upon bending. *Organic Electronics*, 31:177–182, 2016.
- V. Raghuwanshi, D. Bharti, A. K. Mahato, I. Varun, and S. P. Tiwari. Semiconductor: Polymer blend ratio dependent performance and stability in low voltage flexible organic field-effect transistors. *Synthetic Metals*, 236:54–60, 2018.
- S. C. Rasmussen. The path to conductive polyacetylene. *Bull. Hist. Chem*, 39(1):64–72, 2014.
- R. Ravichandran, S. Sundarrajan, J. R. Venugopal, S. Mukherjee, and S. Ramakrishna. Applications of conducting polymers and their issues in biomedical engineering. *Journal of the Royal Society Interface*, 7(suppl\_5):S559–S579, 2010.
- J. Rivnay, S. C. Mannsfeld, C. E. Miller, A. Salleo, and M. F. Toney. Quantitative determination of organic semiconductor microstructure from the molecular to device scale. *Chemical reviews*, 112(10):5488–5519, 2012.
- H. Rose. Wien-type imaging corrector for an electron microscope, Oct. 9 1990. US Patent 4,962,313.
- E. Saldivar-Guerra and E. Vivaldo-Lima. *Handbook of polymer synthesis, characterization, and processing*. John Wiley & Sons, 2013.
- A. Salleo, R. J. Kline, D. M. DeLongchamp, and M. L. Chabinyc. Microstructural characterization and charge transport in thin films of conjugated polymers. *Advanced Materials*, 22(34):3812–3838, 2010.
- I. Salzmann, S. Duhm, G. Heimel, J. P. Rabe, N. Koch, M. Oehzelt, Y. Sakamoto, and T. Suzuki. Structural order in perfluoropentacene thin films and heterostructures with pentacene. *Langmuir*, 24(14):7294–7298, 2008.
- S. Sasaki, K. Fujino, and Y. Takéuchi. X-ray determination of electron-density distributions in oxides, mgo, mno, coo, and nio, and atomic scattering factors

- of their constituent atoms. *Proceedings of the Japan Academy, Series B*, 55(2): 43–48, 1979.
- B. H. Savitzky, R. Hovden, K. Whitham, J. Yang, F. Wise, T. Hanrath, and L. F. Kourkoutis. Propagation of structural disorder in epitaxially connected quantum dot solids from atomic to micron scale. *Nano letters*, 16(9):5714–5718, 2016.
- L. Sawyer, D. T. Grubb, and G. F. Meyers. *Polymer microscopy*. Springer Science & Business Media, 2008.
- J. B. Sherman, K. Moncino, T. Baruah, G. Wu, S. R. Parkin, B. Purushothaman, R. Zope, J. Anthony, and M. L. Chabinye. Crystalline alloys of organic donors and acceptors based on tips-pentacene. *The Journal of Physical Chemistry C*, 119(36):20823–20832, 2015.
- A. Shih and A. I. Akinwande. Solution-processed and self-assembled monolayer-treated high-voltage organic thin film transistors for flexible mems integration. *MRS Advances*, 3(33):1877–1882, 2018.
- H. Shirakawa, E. J. Louis, A. G. MacDiarmid, C. K. Chiang, and A. J. Heeger. Synthesis of electrically conducting organic polymers: halogen derivatives of polyacetylene,(ch) x. *Journal of the Chemical Society, Chemical Communications*, (16):578–580, 1977.
- B. Stadlober, V. Satzinger, H. Maresch, D. Somitsch, A. Haase, H. Pichler, W. Rom, and G. Jakopic. Structural and electrical properties of polymorphic pentacene thin films. In *Organic Field Effect Transistors II*, volume 5217, pages 112–123. SPIE, 2003.
- M. S’ari, H. Blade, R. Brydson, S. D. Cosgrove, N. Hondow, L. P. Hughes, and A. Brown. Toward developing a predictive approach to assess electron beam instability during transmission electron microscopy of drug molecules. *Molecular Pharmaceutics*, 15(11):5114–5123, 2018.

- N. Tanaka. Present status and future prospects of spherical aberration corrected tem/stem for study of nanomaterials. *Science and Technology of Advanced Materials*, 2008.
- M. W. Tate, P. Purohit, D. Chamberlain, K. X. Nguyen, R. Hovden, C. S. Chang, P. Deb, E. Turgut, J. T. Heron, D. G. Schlom, et al. High dynamic range pixel array detector for scanning transmission electron microscopy. *Microscopy and Microanalysis*, 22(1):237–249, 2016.
- B. C. Thompson and J. M. Fréchet. Polymer–fullerene composite solar cells. *Angewandte chemie international edition*, 47(1):58–77, 2008.
- M. Treacy and J. Gibson. Coherence and multiple scattering in “z-contrast” images. *Ultramicroscopy*, 52(1):31–53, 1993.
- M. Treacy and J. Gibson. Variable coherence microscopy: A rich source of structural information from disordered materials. *Acta Crystallographica Section A: Foundations of Crystallography*, 52(2):212–220, 1996.
- M. Treacy, J. Gibson, and P. Kebabinski. Paracrystallites found in evaporated amorphous tetrahedral semiconductors. *Journal of non-crystalline solids*, 231(1-2):99–110, 1998.
- M. Treacy, J. Gibson, L. Fan, D. Paterson, and I. McNulty. Fluctuation microscopy: a probe of medium range order. *Reports on Progress in Physics*, 68(12):2899, 2005.
- K. van Benthem, A. R. Lupini, M. Kim, H. S. Baik, S. Doh, J.-H. Lee, M. P. Oxley, S. D. Findlay, L. J. Allen, J. T. Luck, et al. Three-dimensional imaging of individual hafnium atoms inside a semiconductor device. *Applied Physics Letters*, 87(3):034104, 2005.
- K. Varlot, J. Martin, D. Gonbeau, and C. Quet. Chemical bonding analysis of electron-sensitive polymers by eels. *Polymer*, 40(20):5691–5697, 1999.

- E. Verploegen, C. E. Miller, K. Schmidt, Z. Bao, and M. F. Toney. Manipulating the morphology of p3ht–pcbm bulk heterojunction blends with solvent vapor annealing. *Chemistry of Materials*, 24(20):3923–3931, 2012.
- P. Voyles and D. Muller. Fluctuation microscopy in the stem. *Ultramicroscopy*, 93(2):147–159, 2002.
- P. Voyles, J. Gibson, and M. Treacy. Fluctuation microscopy: a probe of atomic correlations in disordered materials. *Microscopy*, 49(2):259–266, 2000.
- P. Voyles, J. Gerbi, M. Treacy, J. Gibson, and J. Abelson. Absence of an abrupt phase change from polycrystalline to amorphous in silicon with deposition temperature. *Physical review letters*, 86(24):5514, 2001a.
- P. Voyles, N. Zotov, S. Nakhmanson, D. Drabold, J. Gibson, M. Treacy, and P. Keblinski. Structure and physical properties of paracrystalline atomistic models of amorphous silicon. *Journal of Applied Physics*, 90(9):4437–4451, 2001b.
- P. M. Voyles and J. R. Abelson. Medium-range order in amorphous silicon measured by fluctuation electron microscopy. *Solar energy materials and solar cells*, 78(1-4):85–113, 2003.
- W. Wang, S. Guo, E. M. Herzig, K. Sarkar, M. Schindler, D. Magerl, M. Philipp, J. Perlich, and P. Müller-Buschbaum. Investigation of morphological degradation of p3ht: Pcbm bulk heterojunction films exposed to long-term host solvent vapor. *Journal of Materials Chemistry A*, 4(10):3743–3753, 2016.
- K. A. Wepasnick, B. A. Smith, J. L. Bitter, and D. Howard Fairbrother. Chemical and structural characterization of carbon nanotube surfaces. *Analytical and bioanalytical chemistry*, 396(3):1003–1014, 2010.
- S. E. Wheeler. Local nature of substituent effects in stacking interactions. *Journal of the American Chemical Society*, 133(26):10262–10274, 2011.

- D. B. Williams and C. B. Carter. Transmission electron microscopy. *Systematic Materials Analysis*, 4:407–432, 1978.
- D. B. Williams and C. B. Carter. X-ray spectrometry. In *Transmission Electron Microscopy*, pages 581–603. Springer, 2009.
- H. Yang, L. Jones, H. Ryll, M. Simson, H. Soltau, Y. Kondo, R. Sagawa, H. Banba, I. MacLaren, and P. Nellist. 4d stem: High efficiency phase contrast imaging using a fast pixelated detector. In *Journal of Physics: Conference Series*, volume 644, page 012032. IOP Publishing, 2015.
- Z.-F. Yao, J.-Y. Wang, and J. Pei. Control of  $\pi$ - $\pi$  stacking via crystal engineering in organic conjugated small molecule crystals. *Crystal Growth & Design*, 18(1): 7–15, 2018.
- K. Yase, S. Horiuchi, M. Kyotani, M. Yumura, K. Uchida, S. Ohshima, Y. Kuriki, F. Ikazaki, and N. Yamahira. Angular-resolved eels of a carbon nanotube. *Thin Solid Films*, 273(1-2):222–224, 1996.
- F. Yi and P. Voyles. Effect of sample thickness, energy filtering, and probe coherence on fluctuation electron microscopy experiments. *Ultramicroscopy*, 111(8): 1375–1380, 2011.
- F. Yi, P. Tiemeijer, and P. M. Voyles. Flexible formation of coherent probes on an aberration-corrected stem with three condensers. *Journal of electron microscopy*, 59(S1):S15–S21, 2010.
- H. Yoo, H. H. Choi, T. J. Shin, T. Rim, K. Cho, S. Jung, and J.-J. Kim. Self-assembled, millimeter-sized tips-pentacene spherulites grown on partially cross-linked polymer gate dielectric. *Advanced Functional Materials*, 25(24):3658–3665, 2015.
- Y. Yunus, N. A. Mahadzir, M. N. Mohamed Ansari, T. H. Tg Abd Aziz, A. Mohd Afdzaluddin, H. Anwar, M. Wang, and A. G. Ismail. Review of the

- common deposition methods of thin-film pentacene, its derivatives, and their performance. *Polymers*, 14(6):1112, 2022.
- S. S. Zade and M. Bendikov. Heptacene and beyond: the longest characterized acenes. *Angewandte Chemie International Edition*, 49(24):4012–4015, 2010.
- C. Zhang, Y. Zang, F. Zhang, Y. Diao, C. R. McNeill, C.-a. Di, X. Zhu, and D. Zhu. Pursuing high-mobility n-type organic semiconductors by combination of “molecule-framework” and “side-chain” engineering. *Advanced Materials*, 28(38):8456–8462, 2016.
- P. Zhang, Z. Wang, J. H. Perepezko, and P. M. Voyles. Vitrification, crystallization, and atomic structure of deformed and quenched ni60nb40 metallic glass. *Journal of Non-Crystalline Solids*, 491:133–140, 2018.
- L. Zheng, J. Liu, Y. Ding, and Y. Han. Morphology evolution and structural transformation of solution-processed methanofullerene thin film under thermal annealing. *The Journal of Physical Chemistry B*, 115(25):8071–8077, 2011.
- W. Zhou and Z. L. Wang. *Scanning microscopy for nanotechnology: techniques and applications*. Springer science & business media, 2007.